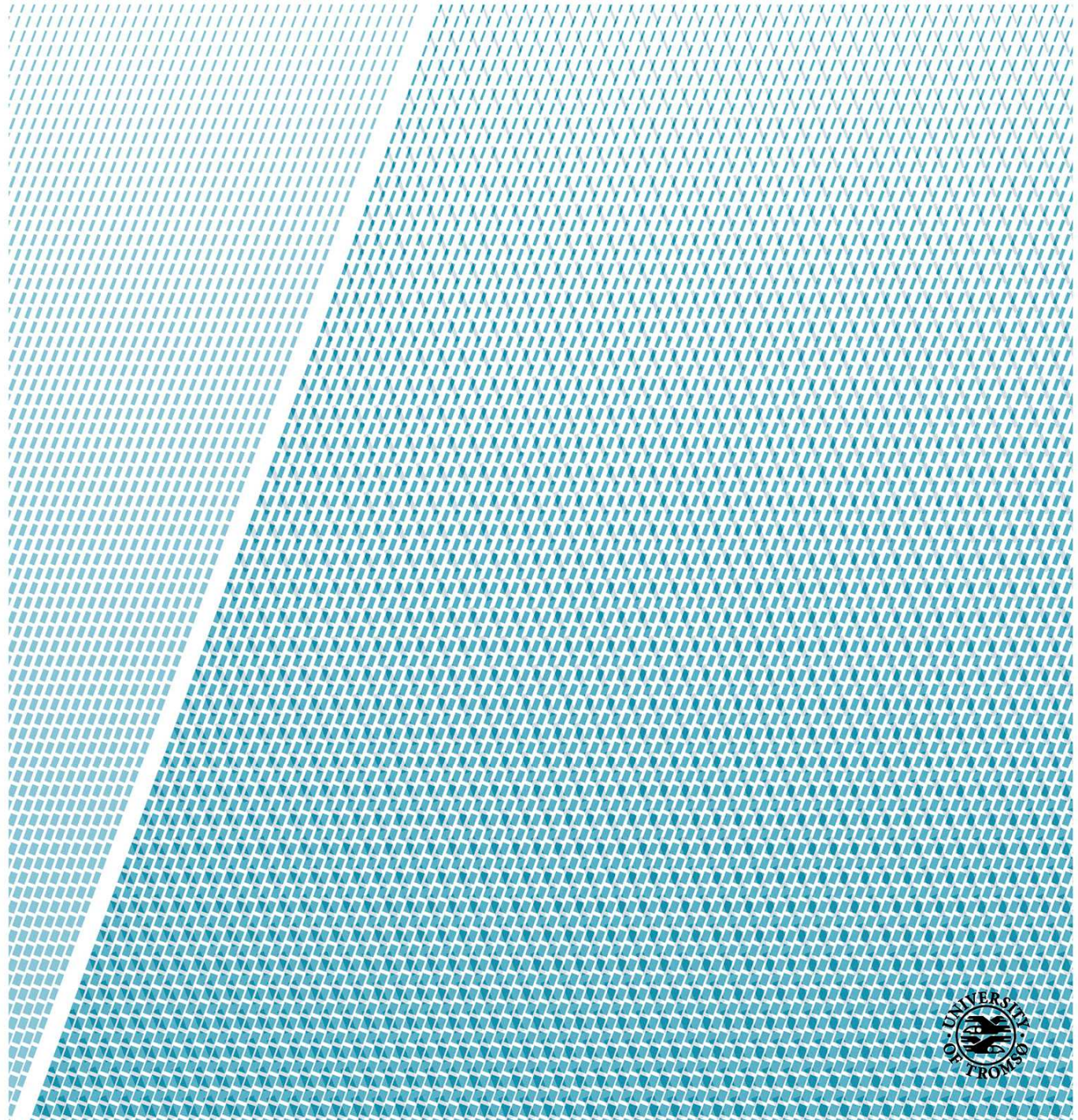


Department of Physics and Technology

“Physical and statistical based decomposition of Polarimetric Synthetic Aperture Radar images of Arctic Sea Ice”

Alberto Arienzo

Master thesis in applied physics and mathematics FYS-3941 - June 2015



To my loved mentor, Daisaku Ikeda.

To the Soka Gakkai International.

To my wonderful family.

Contents

1	Introduction	4
1.1	Motivations and goals	4
1.2	Structure of the thesis	5
1.3	Previous works	6
2	Polarimetric Radar Imaging	8
2.1	Electromagnetic Fields	8
2.1.1	Plane Waves	9
2.1.2	Polarimetry	10
2.2	SAR Theory	12
2.2.1	Airborne SAR and Spaceborne SAR	15
2.3	Polarimetric SAR	17
2.3.1	Polarimetric Coherency and Covariance Matrices	17
2.3.1.1	Bistatic Scattering Case	18
2.3.1.2	Monostatic Scattering Case	20
2.3.2	Speckle and Multilooking	22
2.3.3	Radar Cross Section	24
3	Arctic Sea Ice	28
3.1	Why Remote Sensing of Sea Ice is important?	28
3.2	Scattering Mechanisms	29
3.2.1	Surface Scattering	30
3.2.1.1	Single-Bounce Scattering	31
3.2.1.2	Bragg Model	32
3.2.1.3	Double-Bounce Scattering	34
3.2.1.4	Extended Bragg Model	35
3.2.2	Volume Scattering	37
3.3	Physical Model of Arctic Sea Ice	39
3.3.1	Sea Ice constituents	40
3.3.2	Terminology	41
3.3.3	First-year Ice vs Multi-Year Ice	42
3.3.4	Polarimetric Parameters of interest of Sea Ice	45

4	Polarimetric Decomposition Theorems	48
4.1	Coherent Decompositions	48
4.2	Eigenvector-based Decompositions	49
4.3	Model-Based Decompositions	51
4.3.1	Freeman and Durden Decomposition	51
4.3.2	Non-Negative Eigenvalue Decomposition	53
4.3.3	Sea Ice Two-Component Decomposition	55
4.4	Model-Based decompositions comparison	57
5	Model-Based Decomposition with Higher-Order Statistics	60
5.1	PolSAR Data Statistics	60
5.1.1	Product model and Texture	61
5.2	Model-based Decompositions with fourth-order statistics approach	62
5.2.1	Sea Ice Two-component Decomposition	65
5.2.2	Freeman and Durden Decomposition	67
5.2.3	Optimisation Algorithm	68
5.2.3.1	Relative weights	69
6	Data Material Description	70
6.1	SLC and MLC Data	70
6.2	Test Images	71
6.3	Real Images	72
6.4	Accuracy	72
7	Results	76
7.1	Traditional Model-Based Decompositions	76
7.2	Model-Based Decomposition using fourth-order statistics	78
7.2.1	Sea Ice Two-component Decomposition	79
7.2.1.1	Test Pattern	79
7.2.1.2	Real Images	89
7.2.1.3	Texture Analysis:	95
7.2.2	Freeman and Durden Decomposition	96
8	Conclusions	104
8.1	Summary	104
8.2	Future challenges	106
	Bibliography	108
A	Freeman and Durden Decomposition	112
B	Sea Ice Two-Component Decomposition	116

List of Figures

2.1	Representation of a monochromatic plane wave.	10
2.2	Electric field of a linearly polarized wave.	11
2.3	Electric field of a circularly polarized wave.	12
2.4	SAR geometry	13
2.5	Typical geometry of SAR antenna.	14
2.6	Broadside SAR geometry.	15
2.7	Spaceborne SAR geometry.	16
2.8	Typical implementation of a polarimetric radar.	18
2.9	Speckle formation mechanism.	22
2.10	Splitting of the Synthetic Aperture Length in L=3 subsets.	24
2.11	Radar cross section for a perfectly conducting sphere.	25
3.1	Global warming-Arctic Sea ice connection.	29
3.2	Current arctic sea ice extent with its lowest point reached in September 2012.	29
3.3	Classical problem of reflection and transmission at a plane dielectric interface.	30
3.4	Geometry of Single-Bounce Scattering Mechanism.	32
3.5	Geometry of Double-Bounce Scattering Mechanism.	35
3.6	Azimuth slope $\bar{\chi}$ introduced in the X-Bragg model.	35
3.7	Geometry of the volume scattering mechanism.	37
3.8	Temperature-salinity behavior of sea ice.	40
3.9	Cross Section of MultiYear-Ice.	44
3.10	Typical frequency bands used in sea ice remote sensing.	47
4.1	Uniform probability density function for the orientation angle θ in polar coordinates.	52
6.1	SLC Data Format.	70
6.2	Test images used to simulate Sea Ice Two-Component decomposition parameters.	72
6.3	Pauli decomposition of sea ice scene from Fram Strait, Greenland.	74
6.4	Pauli decomposition of San Francisco Bay, California.	75

7.1	Non Negative Eigenvalue decomposition of sea ice scene from Fram Strait, Greenland. Span normalised powers.	77
7.2	Traditional Freeman and Durden decomposition of sea ice scene from Fram Strait, Greenland. Span normalised powers.	78
7.3	Sea Ice Two-Component decomposition using second-order statistics and the optimisation strategy.	92
7.4	Sea Ice Two-Component decomposition using fourth-order statistics with the algebraic solution, for Non-Textured model.	93
7.5	Sea Ice Two-Component decomposition using fourth-order statistics and the optimisation strategy, for Non-Textured model.	94
7.6	Sea Ice Two-Component decomposition using fourth-order statistics and the optimisation strategy, for Textured model.	95
7.7	Texture power of the Sea Ice-Two component decomposition.	96
7.8	Traditional Freeman and Durden decomposition fixing β or α	98
7.9	Freeman and Durden decomposition obtained with the second-order moments and the optimisation algorithm.	99
7.10	Freeman and Durden decomposition obtained with the fourth-order moments for the Non-Textured model.	100
7.11	Freeman and Durden decomposition obtained with the fourth-order moments for the Textured model.	101
7.12	RGB images power fractions of the considered decompositions.	102

List of Tables

2.1	Representative Airborne and Spaceborne SAR parameters.	16
3.1	Sea Ice Stage of Development.	43
7.1	Sea Ice Two-Component decomposition using second-order statistics and the optimisation strategy, for Gaussian data.	81
7.2	Sea Ice Two-Component decomposition using fourth-order statistics for the Non-Textured model computed with the algebraic solution and Gaussian data.	82
7.3	Sea Ice Two-Component decomposition using fourth-order statistics and the optimisation strategy, for the Non-Textured model and Gaussian data.	83
7.4	Sea Ice Two-Component decomposition using fourth-order statistics and the optimisation strategy, for Textured model and Gaussian data.	84
7.5	Summary results for the various Sea Ice Two-Component decomposition with Gaussian data.	85
7.6	Second-Order and High-order methods comparison, with Gaussian data.	86
7.7	Sea Ice Two-Component decomposition using fourth-order moments and the optimisation algorithm for Non-Textured model and Non Gaussian data.	88
7.8	Sea Ice Two-Component decomposition using fourth-order moments and the optimisation algorithm for Textured model and Non Gaussian data.	89

Nomenclature

BSA	Backscatter Alignment
ENL	Equivalent Number of Looks
FSA	Forward Scatter Alignment
FY Ice	First-Year Ice
HPBW	Half Power Beam Width
MLC	Multi Look Complex
MY Ice	Multi-Year Ice
NNED	Non Negative Eigenvalue Decomposition
PDF	Probability Density Function
PO	Physical Optics
PolSAR	Polarimetric SAR
RCS	Radar Cross Section
RMSE	Root Mean Square Error
SAR	Synthetic Aperture Radar
SLC	Single Look Complex
SNR	Signal to Noise Ratio
SPM	Small Perturbation Method
SVD	Singular Value Decomposition
TE	Transverse Electric

Abstract

The studies about the climatic changes have always more underlined the importance of the climatic balance of the Arctic regions. For this reason the need of monitoring the Arctic becomes always more urgent. To measure the sea ice thickness, the sea ice cover, the motion of the glaciers and to discriminate the various kind of ice are only several of the challenges about the Arctic monitoring. But the extreme climatic conditions make the Arctic one of the most inaccessible regions on the Earth. Radar imaging and in particular polarimetric radar imaging provide indispensable instruments in this challenge. In our thesis work we analyzed a common topic in radar polarimetry: the model-based decompositions. Such decompositions have the goal of interpreting the scattering mechanism for each single pixel in the polarimetric image through statistical instruments, as the covariance or coherency matrix, and physical instruments, as the main laws of the electromagnetism in the context of the scattering theory. The model-based decompositions are typically characterized by a large number of unknowns, the parameters of the target, but usually they cannot be estimated for lack of enough equations. Typically, the model-based decomposition problems are underdetermined and in order to find an unique solution it is necessary fixing some parameters or making some prior assumptions. The ideal condition would be to have more equations in order to uniquely resolve the system, without approximations. This it is exactly the goal of our thesis work, introducing new equations using the fourth-order moments. Investigating such a possibility we analyzed a particular specific model-based decomposition for the sea ice: the Sea Ice Two-Component decomposition. The simulations have been made using test pattern especially built in such a way to have a solid and effective reference of the quality of the decomposition. Only after we tried with the real sea ice image of the Fram Strait, Greenland. The obtained test pattern results have shown a significant improvement in the parameters estimation compared to the second-order case. As regards the real simulations, we cannot affirm the same thing of the test patterns. However, we think the good test pattern results, are a preliminary confirm of the usefulness of the fourth-order moments in the model-based decompositions. To use the additional equations given by the fourth-order moments, it has enabled us: 1) to find an algebraic solution without fixing any parameters, 2) the possibility of including the product model and so to get the information texture for any model-based decomposition. However, often to find an analytic solution is very complicated. For this reason, we implemented an optimisation algorithm with a relative normalisation strategy that it allowed us: 1) to retrieve a solution when an algebraic solution cannot be found and retrieving a larger number of free parameters in respect to the traditional model-based decomposition, 2) to obtain smooth image thanks to the speckle robustness of the optimisation algorithm. Concluding, our work shows a preliminary possibility of using the fourth-order moments in the model-based decompositions.

Chapter 1

Introduction

1.1 Motivations and goals

In the last fifty years, it has been possible to see an important development concerning Radar systems and Remote Sensing. Historically, Radars were born in military context where the presence of impressive economic resources is well-known. This fact has definitely contributed to its majestic scientific development. It is easy to see how much nowadays radar systems are spread in several fields: meteorology, astronomy, geophysics, surveillance systems and diagnostic and therapeutic applications. A particularly important topic in radar studies is polarimetry. Radar polarimetry uses the polarization of the electromagnetic waves as additional parameter in order to get additional information about the target. Nowadays Synthetic Aperture Radar are considered as the last generation radars. SARs are basically pulsed radar mounted on airborne or spaceborne systems and they use the motion of the platform where they are placed in order to realize a spatial sampling illuminating the target for a longer time interval and to receive a large number of echoes from the target compared to the fixed radar systems. This technique achieves very high spatial resolution. Particularly innovative are the Polarimetric SAR or more commonly called PolSAR. These last are SAR that use the polarimetry and they can be considered the latest generation radar. The main characteristic of the PolSAR data is that they are related to a large amount of information about the considered target. Often, the number of physical parameters that influence the signal are greater than the measured terms. This fact has caused in PolSAR area the birth of several studies and method with the same goal: to find estimators in order to estimate the major number of parameters with an high degree of accuracy. One of the first method applied at the analysis of PolSAR data have been the “decompositions”. These methods consist of decomposing the covariance matrix in N components each of them is related to a particular scattering mechanism. The most used decompositions are the eigenvalue-decompositions and the model-based decomposition. The eigenvalue decompositions are based

on the eigenstructure of the covariance matrix while the model-based decomposition are based on the physics meaning of the covariance matrix. Typically the scattering mechanisms are three: surface scattering, volume scattering, and double-bounce scattering. The main characteristic of the model-based decomposition is that they are based on the physics scattering model derived from the laws of electromagnetism. Unfortunately, often the number of unknowns, the parameters describing the target, is more than the number of equations. In this sense, it is usual to make prior assumptions or approximations in order to resolve the problem uniquely. Typically the model-based decompositions use only the second-order statistics, the covariance matrix. It is hard to find research about polarimetry that use higher-order moments than the second-order. This is exactly that we tried to verify: to use the fourth-order moments in order to have a greater number of equations and so solve the problem without assumptions or approximations. This goal is very ambitious and it is important to mark that it has not been explored before. We think if we succeed it is possible to create a new trend in radar polarimetry. A large important section of this thesis work has been analyzing and implementing the specific model based-decomposition for the Sea ice proposed in [9]. Later we will refer to this decomposition as the Sea Ice Two-Component decomposition. In the literature it is easy to find a large number of articles about the model-based decompositions, but most of them propose model-based decomposition for urban area, forests, and vegetated areas. It is harder to find a model-based decomposition specified for sea ice. Let us try to understand why. Sea ice, in particular the Arctic sea ice, shows unique characteristics very different from any other matter usually analyzed in remote sensing. In our work we will describe the main electromagnetically properties of sea ice. Climatic changes and global warming are topical issues. It is well known that the Arctic climate plays a primary role in the world climatic balance. For this reason a lot of studies and research originates with the goal of monitoring and getting information about the Arctic regions. The extreme climatic conditions, as the darkness, very low temperatures, impressive snowfall and strong winds, make the Arctic one of the more inaccessible regions on the Earth. In this sense, Remote Sensing and Radar Systems provide essential tools for the ambitious challenge of monitoring of Arctic. In conclusion, the main goal of our work has been verifying the possibility of using fourth-order statistics in the model-based decomposition in order to extract a greater amount of information without using prior assumptions or approximations. In doing so, we widely analyzed the Sea Ice Two-component model and so we will show the development of this specified decomposition for sea ice.

1.2 Structure of the thesis

Let us see the chapters in review.

- Chapter 2 “Polarimetric Radar Imaging” : in this chapter we will recall the main concepts about the electromagnetic theory, Synthetic aperture radar and Polarimetric Synthetic Aperture radar.

- Chapter 3 “Arctic Sea Ice” : this chapter contains all the concepts about sea ice that we think are useful for the following chapters. In order to describe the Sea Ice we started by describing the physical model and finished with its electromagnetic behavior.
- Chapter 4 “Polarimetric Decomposition Theorems”: this chapter recalls the most important concepts related to our work. In particular we recalled all the concepts about radar polarimetry and we described with particular attention the most important model-based decomposition theorems. The model-based decomposition considered have been the Freeman and Durden decomposition, the Non Negative Eigenvalue Decomposition and the Sea Ice Two-Component decomposition. We concluded this chapter describing their differences.
- Chapter 5 “Model-Based Decomposition with Higher-Order Statistics”: this is the heart of our work. We started describing the PolSAR data statistics and recalling the product model and the texture concepts. Subsequently, we described the used approach to apply the higher-order statistics to the traditional model-based decomposition. Particularly important is the description of the used optimisation algorithm strategy.
- Chapter 6 “Data Material Description” : this chapter is completely dedicated to provide to the reader with information about the data used in our work. We described the used test images and the real images and we conclude describing the used accuracy in order to have a measure of the quality of the considered methods.
- Chapter 7 “Results”: In this chapter are shown all the results of the large amount of theory described before. This chapter will verify whether the theory described in Chapter 5 is appropriate. We will show the results starting from the test images and we will conclude with the more realistic images of Fram strait sea ice, Greenland, and the San Francisco Bay.

1.3 Previous works

The master thesis work finds its roots in two articles:

1. “Model-based polarimetric decomposition of Arctic sea ice.” [T. Eltoft, A. P. Doulgeris, and J. Grahn] [9].
2. “Can higher-order statistics add information in model-based polarimetric decompositions?” [A. P. Doulgeris and T. Eltoft.] [7].

The first article proposed the Sea Ice Two-Component decomposition. The second paper, a natural and historical continuation of the first article, shows the interesting possibility to use the higher-order moments, specially the fourth-order moments, in order to have enough equations for estimating all the polarimetric parameters.

Chapter 2

Polarimetric Radar Imaging

The goal of this chapter is to introduce the basics of Polarimetric Radar Imaging. This is a multidisciplinary topic that involves electromagnetism, statistical signal and image processing, remote sensing and radar fundamentals. Remote sensing is defined as the acquisition of information about an object without being in physical contact with it. Information is acquired by detecting and measuring changes that the object imposes on the surrounding field, be it an electromagnetic, acoustic or potential field. This could include an electromagnetic field emitted or reflected by the object, acoustic waves reflected or perturbed by the object or perturbations of the surrounding gravity or magnetic field due to the presence of the object. Remote sensing techniques cover the whole electromagnetic spectrum from low-frequency radio waves through the microwave, submilliliter, far infrared, near infrared, ultraviolet, x-ray and gamma-ray regions of the spectrum [8]. RADAR is the acronym of Radio Detection and Ranging and uses mainly electromagnetic waves from radio frequencies [3-300] MHz up to microwave frequencies [1-40] GHz. Radar principle is relatively simple: it radiates electromagnetic waves towards the surrounding environment and receives the reflected echoes. From the modification of the received echoes, respect to the transmitted signal, it is possible to obtain information about the environment. In this work, we will pay attention to a particular Radar Sensor: Polarimetric Synthetic Aperture Radar. During the thesis, we will recall the most important concepts of the cited topics in order to simplify the subsequent argument.

2.1 Electromagnetic Fields

Electromagnetic theory is the basement of many modern applications. Radar, Remote Sensing and Communications systems are ones of these. It is easy to understand the importance of electromagnetic theory in Radar and Remote Sensing. For this reason, we will briefly recall the electromagnetic theory starting from the Maxwell's Equations.

2.1.1 Plane Waves

The basic laws of electricity and magnetism can be summarized by the Maxwell equations. In the absence of sources and in the case of an infinite medium they are:

$$\begin{aligned}\nabla \cdot \mathbf{B} &= 0 & \nabla \times \mathbf{H} &= \frac{\partial \mathbf{D}}{\partial t} \\ \nabla \cdot \mathbf{D} &= 0 & \nabla \times \mathbf{E} &= -\frac{\partial \mathbf{B}}{\partial t}\end{aligned}\tag{2.1}$$

where \mathbf{E} and \mathbf{B} are electric and magnetic field quantities, \mathbf{D} and \mathbf{H} are corresponding derived fields, related to \mathbf{E} and \mathbf{B} through the polarization \mathbf{P} and the magnetization \mathbf{M} of the material medium by the constitutive relations for linear, isotropic media:

$$\mathbf{D} = \varepsilon \mathbf{E} \quad \mathbf{B} = \mu \mathbf{H}\tag{2.2}$$

where ε and μ are the dielectric constant and the magnetic constant, respectively. In general ε and μ may be complex functions of the frequency. Assuming solutions with harmonic time dependence $e^{-i\omega t}$ ¹, the equations for the amplitudes \mathbf{E} can be written as:

$$\begin{aligned}\nabla \cdot \mathbf{B} &= 0 & \nabla \times \mathbf{H} + i\omega \mathbf{D} &= 0 \\ \nabla \cdot \mathbf{D} &= 0 & \nabla \times \mathbf{E} - i\omega \mathbf{B} &= 0\end{aligned}\tag{2.3}$$

Then the equations for \mathbf{E} and \mathbf{H} are:

$$\begin{aligned}\nabla \times \mathbf{E} - i\omega \mathbf{B} &= 0 \\ \nabla \times \mathbf{B} + i\omega \mu \varepsilon \mathbf{E} &= 0\end{aligned}\tag{2.4}$$

By combining the two equations we get the Helmholtz wave equation:

$$(\nabla^2 + \mu \varepsilon \omega^2) \begin{Bmatrix} \mathbf{E} \\ \mathbf{B} \end{Bmatrix} = 0\tag{2.5}$$

Consider as a possible solution a plane wave traveling in the x direction, we find that the wave number k and the frequency ω are related by:

$$k = \sqrt{\mu \varepsilon} \omega\tag{2.6}$$

With the convention that the physical electric and magnetic fields are obtained by taking the real parts of complex quantities, we can write the fields as:

$$\begin{aligned}\mathbf{E}(\mathbf{x}, t) &= \mathcal{E} e^{i\mathbf{k}\mathbf{n}\cdot\mathbf{x} - i\omega t} \\ \mathbf{B}(\mathbf{x}, t) &= \mathcal{B} e^{i\mathbf{k}\mathbf{n}\cdot\mathbf{x} - i\omega t}\end{aligned}\tag{2.7}$$

considering an electromagnetic plane wave of frequency f and wave vector $\mathbf{k} = k\mathbf{n}$, where \mathcal{E} , \mathcal{B} , and \mathbf{n} are constant vectors. By the definition of k , it is

¹ i is the imaginary unit.

necessary that \mathbf{n} be a unit vector such that $\mathbf{n} \cdot \mathbf{n} = 1$. The divergence equations in Equation [2.1] require that:

$$\mathbf{n} \cdot \mathbf{E} = 0 \quad \mathbf{n} \cdot \mathbf{B} = 0 \quad (2.8)$$

This means that \mathbf{E} and \mathbf{B} are both perpendicular to the direction of propagation \mathbf{n} . Such wave is called transverse wave:

$$\mathcal{H} = \mathbf{n} \times \mathcal{E} / Z \quad (2.9)$$

where $Z = \sqrt{\mu/\epsilon}$ is an impedance. In vacuum, $Z = Z_0 = \sqrt{\frac{\mu_0}{\epsilon_0}} = 120\pi$, the impedance of free space [18].

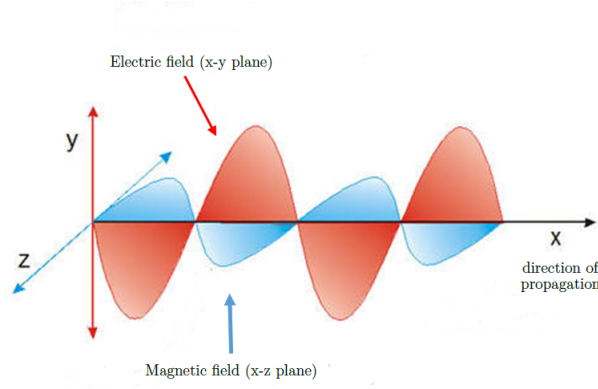


Figure 2.1: Representation of a monochromatic plane wave.

2.1.2 Polarimetry

Polarization is a characteristic of the electromagnetic waves and it describes the oscillation direction of the electric field vector during the wave propagation in the space. Considering the fields in Equation [2.7] and introducing a set of mutually orthogonal real vectors $[\epsilon_1, \epsilon_2, \mathbf{n}]$, it is so possible to describe a linearly polarized wave with polarization vector ϵ_1 . Considering a second wave, linearly polarized into direction ϵ_2 and linearly independent from the first wave, it is so possible to combine the two waves to define the more general homogeneous plane wave $\mathbf{E}(\mathbf{x}, t)$ propagating in the $\mathbf{k} = k\mathbf{n}$ direction:

$$\begin{aligned} \mathbf{E}_1 &= \epsilon_1 \mathcal{E}_1 e^{i\mathbf{k} \cdot \mathbf{x} - i\omega t} \\ \mathbf{E}_2 &= \epsilon_2 \mathcal{E}_2 e^{i\mathbf{k} \cdot \mathbf{x} - i\omega t} \end{aligned} \quad (2.10)$$

with

$$\mathbf{B}_j = \sqrt{\mu\epsilon} \frac{\mathbf{k} \times \mathbf{E}_j}{k} \quad j = 1, 2 \quad (2.11)$$

$$\mathbf{E}(\mathbf{x}, t) = (\epsilon_1 \mathcal{E}_1 + \epsilon_2 \mathcal{E}_2) e^{i\mathbf{k} \cdot \mathbf{x} - i\omega t} \quad (2.12)$$

The amplitudes, \mathcal{E}_1 and \mathcal{E}_2 are complex numbers, so it is possible to use their phase difference to describe a different polarization from linear. If \mathcal{E}_1 and \mathcal{E}_2 have the same phase $\mathbf{E}(\mathbf{x}, t)$ it is called a linearly polarized wave with its polarization vector forming an angle $\theta = \arctan(\frac{\mathcal{E}_2}{\mathcal{E}_1})$ with ϵ_1 and a magnitude $E = \sqrt{\mathcal{E}_1^2 + \mathcal{E}_2^2}$ as shown in the following figure:

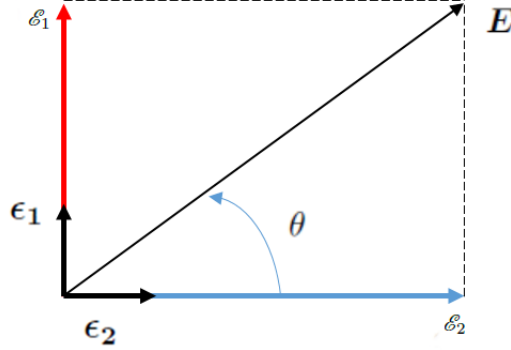


Figure 2.2: Electric field of a linearly polarized wave.

If \mathcal{E}_1 and \mathcal{E}_2 have different phases, then $\mathbf{E}(\mathbf{x}, t)$ is elliptically polarized. To clarify this point, let us consider the simplest case, circular polarization. Then \mathcal{E}_1 and \mathcal{E}_2 have the same magnitude, but differ in phase by ninety degrees, $\delta_x - \delta_y = \pm\pi/2$. The wave $\mathbf{E}(\mathbf{x}, t)$ becomes:

$$\mathbf{E}(\mathbf{x}, t) = \mathcal{E}_0(\epsilon_1 \pm i\epsilon_2) e^{i\mathbf{k} \cdot \mathbf{x} - i\omega t} \quad (2.13)$$

with \mathcal{E}_0 the common real amplitude. Considering ϵ_1 and ϵ_2 in the x and y directions, respectively, and taking the real part of Equation [2.10], then

$$\begin{aligned} \mathbf{E}_x(\mathbf{x}, t) &= \mathcal{E}_0 \cos(kz - \omega t + \delta_x) \\ \mathbf{E}_y(\mathbf{x}, t) &= \mathcal{E}_0 \cos(kz - \omega t + \delta_y) = \mp \mathcal{E}_0 \sin(kz - \omega t + \delta_x) \end{aligned} \quad (2.14)$$

For a fixed point in space, the electric vector is constant in magnitude, but rotates in a circle with a frequency ω , as shown in the following figure:

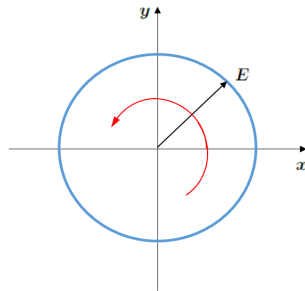


Figure 2.3: Electric field of a circularly polarized wave.

For the positive case ($\epsilon_1 + i\epsilon_2$), the rotation is counterclockwise when the observer is facing into the incoming wave. Such a wave is called left circularly polarized. For the negative case ($\epsilon_1 - i\epsilon_2$), the rotation of \mathbf{E} is clockwise when looking into wave and is called right circularly polarized. It is important to notice that the elliptical polarization is the general case [18].

2.2 SAR Theory

Synthetic Aperture Radars (SARs) are radar systems particularly used for Remote Sensing. They are mounted on airborne or spaceborne systems. SAR is basically a pulsed radar that uses advanced pulse compression techniques. SAR systems and antennas array have some similarities. In the SAR case, we have only one moving antenna transmitting pulses and receiving their echoes in some different positions. This operation mode is called Synthetic Array. The increased use of SAR in the Remote Sensing is based upon three main principles:

1. SAR is an active system, so it can work in darkness and unfavorable meteorological conditions.
2. If microwave frequencies are used, the clouds and precipitations are almost completely invisible at radar.
3. SAR are competitive with and complementary to multispectral radiometers as the primary remote sensing instruments[19].

SAR image formation is done by pointing a radar beam approximately perpendicular to the sensor's motion vector, transmitting phase-encoded pulses and recording the radar echoes as they reflect off the Earth's surface. To form an image, intensity measurements must be taken in two orthogonal directions. In the SAR context, one dimension is parallel to the radar beam, as the time delay of the received echo is proportional to the distance from the sensor, along the image's x-axis. The second dimension of the image is given by travel of the sensor itself. As the sensor moves along in a nominally straight line above the

Earth's surface, the radar beam sweeps along the ground approximately the same speed. The y-dimension is called azimuth or along-track [6]. Let us see in the following figure the general SAR terminology and geometry:

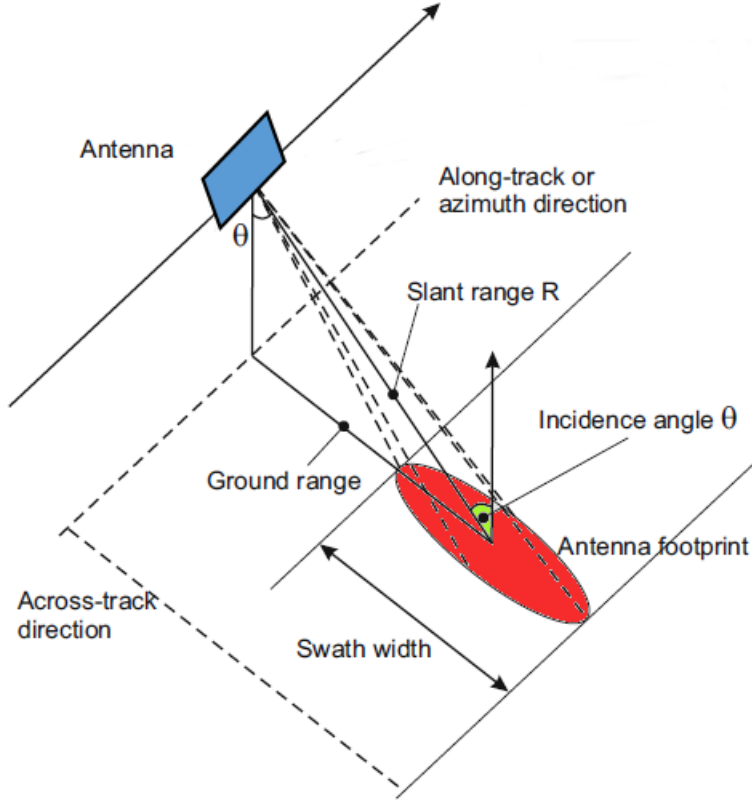


Figure 2.4: SAR geometry

The image, is obtained, with modifications, from [1].

The slant range resolution is given by:

$$\delta_r = \frac{c}{2B} \quad (2.15)$$

where c is the speed of light and B is the transmitted signal bandwidth. The ground range resolution, called swath width in Figure [2.4], defined as the projection of slant range onto the ground, is given by:

$$\delta_x = \frac{\delta_r}{\sin \theta} \quad (2.16)$$

Often, the antennas used in SAR system are phased array of aperture antennas, rectangular and foldable. This last characteristic is very useful to reduce the

size during launch.

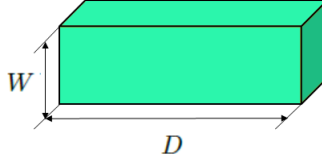


Figure 2.5: Typical geometry of SAR antenna.

For a fixed physical real aperture antenna, it is known that the Half Power Beam Width (HPBW), is:

$$\beta = a \cdot \frac{\lambda}{D} \quad (2.17)$$

where a is the coefficient dependent on the distribution of current in the aperture. Typically a is very close to one. From now we will consider a equals one so the HPBW becomes:

$$\beta = \frac{\lambda}{D} \quad (2.18)$$

Let us consider the broadside geometry for a SAR of Figure [2.6]. Generally, β is small enough to consider the following approximations valid:

$$\tan \frac{\beta}{2} \simeq \frac{\beta}{2} \quad (2.19)$$

In this way the expression of the size of the footprint in azimuthal direction, or more simply the azimuth resolution, is given by:

$$\begin{aligned} \delta_{az} &= \\ &= 2R_0 \tan \frac{\beta}{2} \simeq \\ &\simeq R_0 \frac{\lambda}{D} \end{aligned} \quad (2.20)$$

From such a relationship, it is possible to notice that the azimuth resolution is directly proportional to λ and R_0 but inversely proportional to D . For focused SARs, SARs that use Doppler techniques that allow to reach very high spatial resolutions, the azimuth resolution becomes:

$$\delta_{az} = \frac{D}{2}$$

This result is very important because now the azimuth resolution is only related to the antenna size in azimuth direction and not by R_0 and λ . Accordingly, one may think of decreasing D to improve δ_{az} , but this strategy has some

limitations because to avoid Doppler ambiguity, it is necessary to satisfy the following inequality:

$$D \cdot W > \frac{4\lambda h v \sin \theta}{c \cdot \cos^2 \theta} \quad (2.21)$$

where $D \cdot W$ is the antenna area.

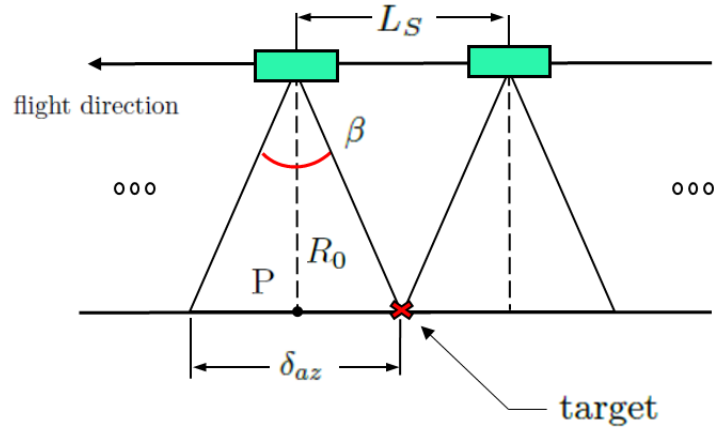


Figure 2.6: Broadside SAR geometry.

L_s is the synthetic aperture length defined as the length of the sensor path during the time that a target remains within the radar beam.

2.2.1 Airborne SAR and Spaceborne SAR

Airborne SARs resolutions are exactly given by Equation [2.15] and Equation [2.20]. Spaceborne SAR and Airborne SAR are characterized by the same ground-range resolution. The only one difference is the azimuth resolution. Let us consider in the following figure, the particular geometry for this type of SAR.

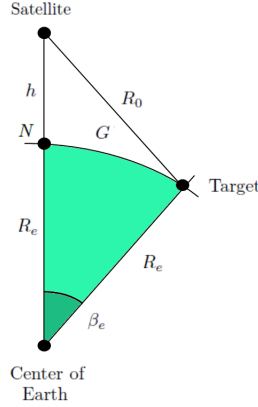


Figure 2.7: Spaceborne SAR geometry.

The image, is obtained, with modifications, from [6].

R_e is the radius of the Earth, h is the altitude of the platform and G is the ground-range, defined as the arc length along the Earth's surface from the nadir point, N , to the target. The corresponding azimuth resolution for an orbital SAR is given by:

$$\delta_{az} = \frac{R_e}{R_e + h} \cdot \frac{D}{2} \quad (2.22)$$

Generally speaking, airborne SARs tend to have better resolution than spaceborne SARs, both in range and in azimuth, because of the shorter antenna lengths and higher bandwidths employed. They also have a higher SNR, because of their large power supplies and shorter operating ranges [6]. Table [2.1] gives a general view of the main characteristics and differences between airborne and spaceborne SAR systems. We will consider the AIRSAR mission and RADARSAT-2 mission, Airborne SAR and Spaceborne SAR, respectively. In our work we will only use images from these two types of radars.

		AIRSAR	RADARSAT-2	
<i>Parameter</i>	<i>Symbol</i>			<i>Units</i>
Bands		L, P, C	C	
Bandwidth	B	20, 40, 80	100	MHz
Range resolution	δ_x	7.5, 3.75, 1.875	4.7	m
Azimuth resolution	δ_{az}	1	28	m
Swath width	S	10	25	km
Altitude	h	8	798	km
Nominal speed	v	778	8	km/h

Table 2.1: Representative Airborne and Spaceborne SAR parameters.

2.3 Polarimetric SAR

If a radiated electromagnetic wave is scattered by an object and one observes this wave in the far field of the scatterer, the scattered wave can, again, be adequately described by a two dimensional vector. In this abstract way, one can consider the scatterer as a mathematical operator that takes one two-dimensional complex vector and changes that into another two dimensional vector, the scattered wave [34]. Mathematically a scatterer can be characterized by a complex 2×2 scattering matrix:

$$\mathbf{E}^s = \frac{e^{-jkr}}{r} \begin{bmatrix} S_{hh} & S_{hv} \\ S_{vh} & S_{vv} \end{bmatrix} \mathbf{E}^i = \frac{e^{-jkr}}{r} [\mathbf{S}] \mathbf{E}^i \quad (2.23)$$

where \mathbf{E}^i is the incident electric field on the target transmitted by the radar antenna. $[\mathbf{S}]$ describes how the scatterer modifies the incident electric field vector and \mathbf{E}^s is the scattered electric field vector incident on the receiving radar antenna. We must consider that the scattering matrix elements are complex quantities and also that the scattering matrix is function of the radar frequency, the scattering material and the considered reference system. The diagonal elements of \mathbf{S} are called “copolar” terms and the off-diagonal elements are called “cross-polar”. Considering S_{ij} , the first subscript indicates the polarization of the incident electric field while the second subscript indicates the polarization of the scattered electric field towards the receiving antenna [34]. e^{-jkr}/r is the well known Green function that describes the propagation for spherical waves. It must be noticed that this relation is only valid in the near field. Before to continue it is important to briefly recall the most used coordinates systems in radar polarimetry. There exist two principal conventions regarding the polarimetric scattering theory: forward scatter alignment, FSA, and backscatter alignment, BSA. In both cases, the electric fields of the incident and the scattered waves are expressed in local coordinates systems centered on the transmitting and receiving antennas, respectively. In the monostatic case, the backscattering matrix, also called the Sinclair matrix, expressed in the FSA convention, can be related to the matrix of the monostatic BSA convention as follows:

$$\mathbf{S}_{BSA} = \begin{bmatrix} -1 & 0 \\ 0 & 1 \end{bmatrix} \mathbf{S}_{FSA} \quad (2.24)$$

Let us see a typical implementation of a polarimetric radar in Figure [2.8]: the Radar, in our case SAR, transmits a wave of one polarization and it receives echoes in two orthogonal polarizations simultaneously. Then is transmitted a wave with the other polarization. In this way, it is possible to acquire four images: one each for the HH, HV, VH, and VV channel. For this reason, polarimetric SARs are called Multichannel SARs.

2.3.1 Polarimetric Coherency and Covariance Matrices

Now let us define the most used basis sets in radar polarimetry. From these bases it is possible to define the “target-vectors” which are a vectorized representation

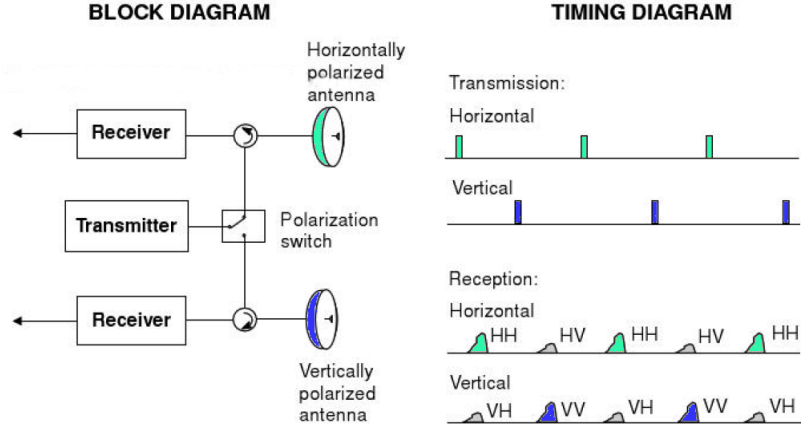


Figure 2.8: Typical implementation of a polarimetric radar.
The image, is obtained, with modifications, from [34].

of the corresponding scattering matrix \mathbf{S} .

2.3.1.1 Bistatic Scattering Case

First we consider the bistatic scattering case. The following part is derived from [19]. This is the case when two antennae are used, one to transmit and one to receive, placed in different positions. One of these basis sets is the complex Pauli spin matrix basis set defined as:

$$\{\Psi_P\} = \left\{ \sqrt{2} \begin{bmatrix} 1 & 0 \\ 0 & 1 \end{bmatrix}, \sqrt{2} \begin{bmatrix} 1 & 0 \\ 0 & -1 \end{bmatrix}, \sqrt{2} \begin{bmatrix} 0 & 1 \\ 1 & 0 \end{bmatrix}, \sqrt{2} \begin{bmatrix} 0 & -i \\ i & 0 \end{bmatrix} \right\} \quad (2.25)$$

The corresponding “4-D κ -target vector” is:

$$\boldsymbol{\kappa} = \frac{1}{\sqrt{2}} [S_{hh} + S_{vv} \quad S_{hh} - S_{vv} \quad S_{hv} + S_{vh} \quad i(S_{hv} - S_{vh})]^T \quad (2.26)$$

Another basis set is the Lexicographic matrix basis set defined as:

$$\{\Psi_L\} = \left\{ 2 \begin{bmatrix} 1 & 0 \\ 0 & 0 \end{bmatrix}, 2 \begin{bmatrix} 0 & 1 \\ 0 & 0 \end{bmatrix}, 2 \begin{bmatrix} 0 & 0 \\ 1 & 0 \end{bmatrix}, 2 \begin{bmatrix} 0 & 0 \\ 0 & 1 \end{bmatrix} \right\} \quad (2.27)$$

and the corresponding “4-D $\boldsymbol{\Omega}$ -target vector” is:

$$\boldsymbol{\Omega} = [S_{hh} \quad S_{hv} \quad S_{vh} \quad S_{vv}]^T \quad (2.28)$$

The total received power from the radar is called Span and is defined as :

$$Span(\mathbf{S}) = Tr(\mathbf{S}\mathbf{S}^H) = |\boldsymbol{\kappa}|^2 = |\boldsymbol{\Omega}|^2 =$$

$$= |S_{hh}|^2 + |S_{vh}|^2 + |S_{hv}|^2 + |S_{vv}|^2 \quad (2.29)$$

Now, we recall briefly the concept of a distributed target. This concept derives by the fact that usually the radar targets are not stationary or fixed but change with time. Typical examples are the motion of water surface or clouds of water droplets. This is particularly true in the case of SAR, where the sensor is moving with respect to the target and illuminating in time the different parts of an extended volume or surface. The radar will receive the time-averaged samples of scattering from a set of different single targets. The set of single targets from which samples are obtained is called a “distributed radar target”. An important type of distributed target is that of an ensemble of targets generated by random processes. Each single target member of the ensemble is then a realization or sample event of the underlying random processes. The scattered return from a distributed radar target which is illuminated by a monochromatic plane wave with fixed frequency and polarization will in general be of the form of a partially polarized plane wave. The state of a partially polarized wave is described by the complex correlations of the electric field components [15]. From Equation [2.23] we can apply the same concept directly to the scattering matrix and so the target vector. Thus, we can define the 4×4 Polarimetric Coherency \mathbf{T} matrix from the 4-D $\boldsymbol{\kappa}$ -target vector:

$$\mathbf{T} = \langle \boldsymbol{\kappa} \boldsymbol{\kappa}^H \rangle = \quad (2.30)$$

$$= \frac{1}{2} \begin{bmatrix} \langle |S_{hh} + S_{vv}|^2 \rangle & \langle (S_{hh} + S_{vv})(S_{hh} - S_{vv})^* \rangle & \cdots \\ \langle (S_{hh} - S_{vv})(S_{hh} + S_{vv})^* \rangle & \langle |S_{hh} - S_{vv}|^2 \rangle & \cdots \\ \langle (S_{hv} + S_{vh})(S_{hh} + S_{vv})^* \rangle & \langle (S_{hv} + S_{vh})(S_{hh} - S_{vv})^* \rangle & \cdots \\ \langle i(S_{hv} - S_{vh})(S_{hh} + S_{vv})^* \rangle & \langle i(S_{hv} - S_{vh})(S_{hh} - S_{vv})^* \rangle & \cdots \\ \cdots & \langle (S_{hh} + S_{vv})(S_{hv} + S_{vh})^* \rangle & \langle -i(S_{hh} + S_{vv})(S_{hv} - S_{vh})^* \rangle \\ \cdots & \langle (S_{hh} - S_{vv})(S_{hv} + S_{vh})^* \rangle & \langle -i(S_{hh} - S_{vv})(S_{hv} - S_{vh})^* \rangle \\ \cdots & \langle |S_{vh} + S_{hv}|^2 \rangle & \langle -i(S_{hv} + S_{vh})(S_{hv} - S_{vh})^* \rangle \\ \cdots & \langle i(S_{hv} - S_{vh})(S_{hv} + S_{vh})^* \rangle & \langle |S_{hv} - S_{vh}|^2 \rangle \end{bmatrix}$$

From the 4-D \mathbf{k} -target vector it is possible to define the 4×4 Polarimetric Covariance \mathbf{C} matrix:

$$\mathbf{C} = \langle \boldsymbol{\Omega} \boldsymbol{\Omega}^H \rangle = \quad (2.31)$$

$$= \begin{bmatrix} \langle |S_{hh}|^2 \rangle & \langle S_{hh}S_{hv}^* \rangle & \langle S_{hh}S_{vh}^* \rangle & \langle S_{hh}S_{vv}^* \rangle \\ \langle S_{hv}S_{hh}^* \rangle & \langle |S_{hv}|^2 \rangle & \langle S_{hv}S_{vh}^* \rangle & \langle S_{hv}S_{vv}^* \rangle \\ \langle S_{vh}S_{hh}^* \rangle & \langle S_{vh}S_{hv}^* \rangle & \langle |S_{vh}|^2 \rangle & \langle S_{vh}S_{vv}^* \rangle \\ \langle S_{vv}S_{hh}^* \rangle & \langle S_{vv}S_{hv}^* \rangle & \langle S_{vv}S_{vh}^* \rangle & \langle |S_{vv}|^2 \rangle \end{bmatrix}$$

where $\langle \dots \rangle$ is the temporal or spatial ensemble averaging, defined as:

$$\langle x(t) \rangle = \lim_{T \rightarrow \infty} \frac{1}{T} \int_0^T x(t) dt \quad (2.32)$$

$$\langle x \rangle = \frac{1}{L} \sum_{i=1}^L x_i \quad (2.33)$$

It is possible to show that \mathbf{T} and \mathbf{C} matrices are Hermitian positive semidefinite. This point is particularly important because:

- The eigenvalues of a Hermitian matrix are real.
- A Hermitian matrix is positive semidefinite if and only if the eigenvalues are nonnegative.
- The eigenvectors of a Hermitian matrix corresponding to distinct eigenvalues are orthogonal [14].

The relation between the coherency \mathbf{T} and covariance \mathbf{C} matrices is given by:

$$\mathbf{T} = \mathbf{U}_4 \mathbf{C} \mathbf{U}_4^{-1} \quad (2.34)$$

and inversely:

$$\mathbf{C} = \mathbf{U}_4^{-1} \mathbf{T} \mathbf{U}_4 \quad (2.35)$$

where \mathbf{U}_4 is the special unitary transformation matrix defined as:

$$\mathbf{U}_4 = \frac{1}{\sqrt{2}} \begin{bmatrix} 1 & 0 & 0 & 1 \\ 1 & 0 & 0 & -1 \\ 0 & 1 & 1 & 0 \\ 0 & i & -i & 0 \end{bmatrix} \quad (2.36)$$

2.3.1.2 Monostatic Scattering Case

In the monostatic case, when one single antenna is used for to transmit and receive, we have:

$$S_{hv} = S_{vh} \quad (2.37)$$

that derives from the reciprocity theorem. In this way, the complex Pauli spin and Lexicographic matrix basis set become:

$$\{\Psi_P\} = \left\{ \sqrt{2} \begin{bmatrix} 1 & 0 \\ 0 & 1 \end{bmatrix} \sqrt{2} \begin{bmatrix} 1 & 0 \\ 0 & -1 \end{bmatrix} \sqrt{2} \begin{bmatrix} 0 & 1 \\ 1 & 0 \end{bmatrix} \right\} \quad (2.38)$$

$$\{\Psi_L\} = \left\{ 2 \begin{bmatrix} 1 & 0 \\ 0 & 0 \end{bmatrix} 2\sqrt{2} \begin{bmatrix} 0 & 1 \\ 0 & 0 \end{bmatrix} 2 \begin{bmatrix} 0 & 0 \\ 0 & 1 \end{bmatrix} \right\} \quad (2.39)$$

and the corresponding “3-D κ -target vector” and “3-D Ω -target vector” are :

$$\kappa = \frac{1}{\sqrt{2}} [S_{hh} + S_{vv} \quad S_{hh} - S_{vv} \quad 2S_{hv}]^T \quad (2.40)$$

$$\Omega = [S_{hh} \quad \sqrt{2}S_{hv} \quad S_{vv}]^T \quad (2.41)$$

The new formulation of the Span is:

$$\begin{aligned} \text{Span}(\mathbf{S}) &= \text{Tr}(\mathbf{S}\mathbf{S}^H) = |\kappa|^2 = |\Omega|^2 = \\ &= |S_{hh}|^2 + 2|S_{hv}|^2 + |S_{vv}|^2 \end{aligned} \quad (2.42)$$

In the same way as seen for the bistatic case, we can define the 3×3 coherency \mathbf{T} and covariance \mathbf{C} matrices as:

$$\begin{aligned} \mathbf{T} &= \langle \kappa \kappa^H \rangle = \quad (2.43) \\ &= \frac{1}{2} \begin{bmatrix} \langle |S_{hh} + S_{vv}|^2 \rangle & \langle (S_{hh} + S_{vv})(S_{hh} - S_{vv})^* \rangle & 2 \langle (S_{hh} + S_{vv})S_{hv}^* \rangle \\ \langle (S_{hh} - S_{vv})(S_{hh} + S_{vv})^* \rangle & \langle |S_{hh} - S_{vv}|^2 \rangle & 2 \langle (S_{hh} - S_{vv})S_{hv}^* \rangle \\ 2 \langle S_{hv}(S_{hh} + S_{vv})^* \rangle & 2 \langle S_{hv}(S_{hh} - S_{vv})^* \rangle & 4 \langle |S_{hv}|^2 \rangle \end{bmatrix} \end{aligned}$$

$$\begin{aligned} \mathbf{C} &= \langle \Omega \Omega^H \rangle = \quad (2.44) \\ &= \begin{bmatrix} \langle |S_{hh}|^2 \rangle & \sqrt{2} \langle S_{hh}S_{hv}^* \rangle & \langle S_{hh}S_{vv}^* \rangle \\ \sqrt{2} \langle S_{hv}S_{hh}^* \rangle & 2 \langle |S_{hv}|^2 \rangle & \sqrt{2} \langle S_{hv}S_{vv}^* \rangle \\ \langle S_{vv}S_{hh}^* \rangle & \sqrt{2} \langle S_{vv}S_{hv}^* \rangle & \langle |S_{vv}|^2 \rangle \end{bmatrix} \end{aligned}$$

The relation between \mathbf{T} and \mathbf{C} is exactly the same seen previously for the bistatic case:

$$\mathbf{T} = \mathbf{U}_3 \mathbf{C} \mathbf{U}_3^{-1} \quad (2.45)$$

and inversely:

$$\mathbf{C} = \mathbf{U}_3^{-1} \mathbf{T} \mathbf{U}_3 \quad (2.46)$$

where the only difference is represented from \mathbf{U}_3 which is the special unitary transformation matrix defined as:

$$\mathbf{U}_3 = \frac{1}{\sqrt{2}} \begin{bmatrix} 1 & 0 & 1 \\ 1 & 0 & -1 \\ 0 & \sqrt{2} & 0 \end{bmatrix} \quad \mathbf{U}_3^{-1} = \frac{1}{\sqrt{2}} \begin{bmatrix} 1 & 1 & 0 \\ 0 & 0 & \sqrt{2} \\ 1 & -1 & 0 \end{bmatrix} \quad (2.47)$$

2.3.2 Speckle and Multilooking

SAR images are affected by the well-known Speckle noise. As the wave interacts with the target, each scatterer contributes a backscattered wave with a phase and amplitude change, so the total returned modulation of the incident wave is:

$$Ae^{i\varphi} = \sum_{n=1}^N A_n e^{i\varphi_n} \quad (2.48)$$

The received waves from each scatterer, although coherent in frequency, are no longer coherent in phase. The sum can be constructive, giving a strong signal sometimes called also up-fading, or destructive, giving a weak signal or also called down-fading. From this, it is easy to understand that the observed signal will be affected by interference effects as a consequence of the phase differences between scatterers. In practice, we can think of the phase as being uniformly distributed and independent of the amplitude [3].

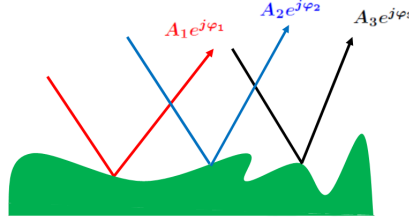


Figure 2.9: Speckle formation mechanism.
The image is obtained, with modifications, from [3].

This type of noise is visible in SAR images as “granular” noise. For large numbers of statistically identical scatterers [25], we can assert that:

- the observed in-phase and quadrature components $z_1 = A \cos \varphi$ and $z_2 = A \sin \varphi$, will be independent identically distributed Gaussian random variables with mean zero and variance σ and so they have a joint probability density function:

$$p_{z_1, z_2}(z_1, z_2) = \frac{1}{\pi} \exp\left(-\frac{z_1^2 + z_2^2}{\sigma}\right) \quad (2.49)$$

- the observed phase φ will be uniformly distributed over $[-\pi, +\pi]$
- the amplitude A will have a Rayleigh distribution

$$p_A(A) = \frac{2A}{\sigma} \exp\left(-\frac{A^2}{\sigma}\right) \quad A \geq 0 \quad (2.50)$$

- the observed intensity $I = A^2$ will have a negative exponential distribution

$$p_I(I) = \frac{1}{\sigma} \exp\left(-\frac{I}{\sigma}\right) \quad I \geq 0 \quad (2.51)$$

It is important to notice that, with the exception of the phase distribution, they are completely characterized by a single parameter σ which corresponds to the average intensity returned to the radar, defined as the Radar Cross Section in the last section of this chapter. It is common to refer to the speckle with the multiplicative noise model, given by:

$$I = \sigma w \quad (2.52)$$

where w , the speckle, is exponentially distributed:

$$p_w(w) = e^{-w} \quad (2.53)$$

Multilooking

A way to improve the estimation of σ and to reduce the speckle is to average L independent intensity values related to the same position. This process, called Multilooking, maintains the mean intensity σ but reduces the estimator variance to σ^2/L . Independent looks can be obtained either by splitting the Doppler bandwidth within the imaging system or making a spatial averaging between neighboring pixels. In both cases, the cost to be paid for the estimation accuracy improvement is a spatial resolution loss by a factor L . The first technique consists to split the set of samples used for the full synthetic aperture into several adjacent subsets. Each of these subsets can be used to form a separate image, known as Look, each of which views a given point from a slightly different angle. Splitting the synthetic aperture into L_S nonoverlapping sections means that each of them has an effective aperture of length L_S/L , so the resolution is degraded by a factor L . The loss of resolution is justified by the fact that now the target is illuminated for a smaller interval time and the corresponding total backscatter will be constituted by a smaller number of echoes. The second technique, done as post processing after a well-focused image is generated, consists in a spatial average between neighboring pixels. In PolSAR, it is common to refer to:

$$\langle C \rangle_{\Omega} = \frac{1}{L} \sum_{i=1}^L \Omega_i \Omega_i^H \quad (2.54)$$

$$\langle C \rangle_{\kappa} = \frac{1}{L} \sum_{i=1}^L \kappa_i \kappa_i^H \quad (2.55)$$

where the symbol H denotes the conjugate transpose operator or simply the Hermitian operator. It is possible moving a small window over each pixel in the image and using the pixel values to calculate the average and then replacing

the central pixel with the new value. The window is moved along in both the row and column dimension one pixel at a time, until the entire image has been covered. This method requires that the data are available in Single Look Complex format, SLC. We conclude with the definition of the equivalent number of looks, ENL. ENL is a parameter of multilook SAR images, which describes the degree of averaging applied to the SAR measurements during data formation and postprocessing [2]. There exists a lot definitions in the literature. We will consider the traditional and the most used version:

$$ENL = \frac{E[I]^2}{var[I]} \quad (2.56)$$



Figure 2.10: Splitting of the Synthetic Aperture Length in L=3 subsets.

2.3.3 Radar Cross Section

The Radar Cross Section, [31], of a target is the area intercepting that amount of power that, when scattered equally in all directions, produces an echo at the radar equal to that from the target, or in other terms:

$$\begin{aligned} \sigma &= \frac{\text{power reflected toward source/unit solid angle}}{\text{incident power density}/4\pi} = \\ &= \lim_{R \rightarrow \infty} 4\pi R^2 \left| \frac{E_s}{E_i} \right|^2 \end{aligned} \quad (2.57)$$

The limit $R \rightarrow \infty$ indicates that such an expression is valid only in the far field. Dimensionally the RCS is a surface and it is expressed in $[m^2]$. In theory, the scattered field, and hence the radar cross section, can be determined by solving the Maxwell's equations with the proper applied boundary conditions. Unfortunately, the determination of the radar cross section with Maxwell's equations can be accomplished only for the most simple of shapes, and solutions valid

over a large range of frequencies are not easy to obtain. The radar cross section of a simple sphere with radius a is shown in Figure [2.1] as a function of its circumference measured in wavelengths, λ .

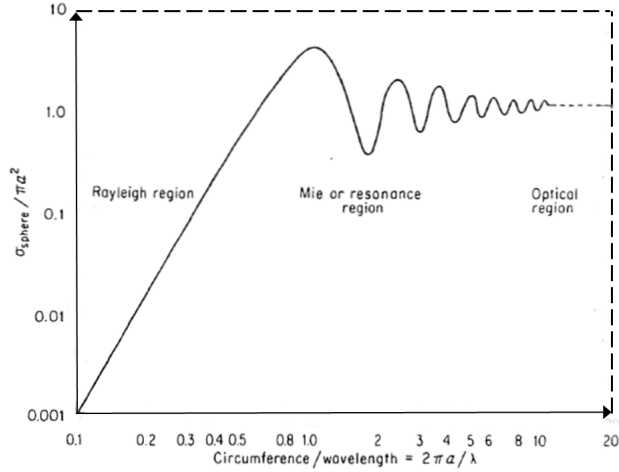


Figure 2.11: Radar cross section for a perfectly conducting sphere.
The image, is obtained, with modifications, from [31].

It is possible to notice that the RCS is highly dependent from the frequency, $f = c/\lambda$, where c is the speed of light in vacuum. In cases different from the sphere, the RCS is function of several parameters like the polarization p , angle of incidence θ , target attitude and target dielectric constant ε .

$$\sigma = \sigma[\lambda, \theta, p, \varepsilon] \quad (2.58)$$

The region where the size of the sphere is small compared with the wavelength is called the Rayleigh region. This region is particularly important because is the most common case in typical radar applications and because the radar cross section varies as :

$$\sigma \propto \frac{1}{\lambda^4} \quad (2.59)$$

In SAR systems it is often used the backscattering coefficient σ^0 , defined as the radar cross section per unit surface area. Such a parameter is dimensionless. In Polarimetric SAR systems such parameter becomes:

$$\sigma_{\mu\tau\nu\kappa}^0 = \lim_{\substack{R \rightarrow \infty \\ A \rightarrow \infty}} \frac{4\pi R^2 \langle E_{\mu s} E_{\nu s}^* \rangle}{A \langle E_{\tau i} E_{\kappa i}^* \rangle} \quad (2.60)$$

where subscripts μ, ν, τ and κ indicate the polarization used, subscripts i and s

stand for incident and scattered fields, respectively, R is the distance from the radar and A is the illuminated area [23].

Chapter 3

Arctic Sea Ice

In this chapter we will describe the main characteristics, physic, and electromagnetic, of the Arctic sea ice. First, we will show the details of all the scattering models used in our thesis work.

3.1 Why Remote Sensing of Sea Ice is important?

World climate is changing and a global warming is observed. Arctic climate warming plays an important role in the balance of the global climate. One of the most dramatic indicators of the Arctic warming is the decline of the sea ice cover. It manifests as a decrease in the ice extent, ice thickness, and the length of the ice season [36]. We can resume the connections between the global and Arctic climate warming through Figure [3.1]. We can notice that Arctic and in particular Arctic Sea Ice are indicators of how much the global climate is changing. In this sense, monitoring of Arctic Sea Ice plays a primary role. From the point of view of weather and climate, and so from the sea ice monitoring point of view, the most essential questions are how much the area covered by sea ice is decreasing, how much the ice and snow thicknesses is decreasing, and how much the melting and ice-free period is lengthening? [36]. To respond to these questions it is crucial to have the appropriate instruments and measurements. Arctic regions are unfriendly and the climate conditions are very strong. Darkness, extremely low temperatures, heavy snowfalls and strong winds make the Arctic regions one of the most inaccessible place on the Earth. In this sense, Remote sensing and Radar can provide indispensable measurements. Passive or active sensors mounted on satellites, drones, helicopters or airplanes are exactly the instruments used in the challenging goal of Arctic sea ice monitoring.

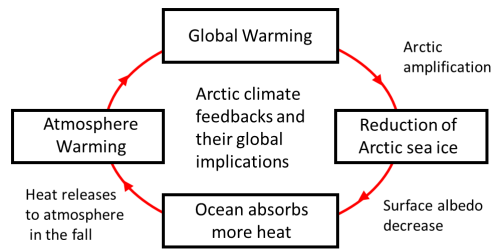


Figure 3.1: Global warming-Arctic Sea ice connection. The image is obtained from[27].

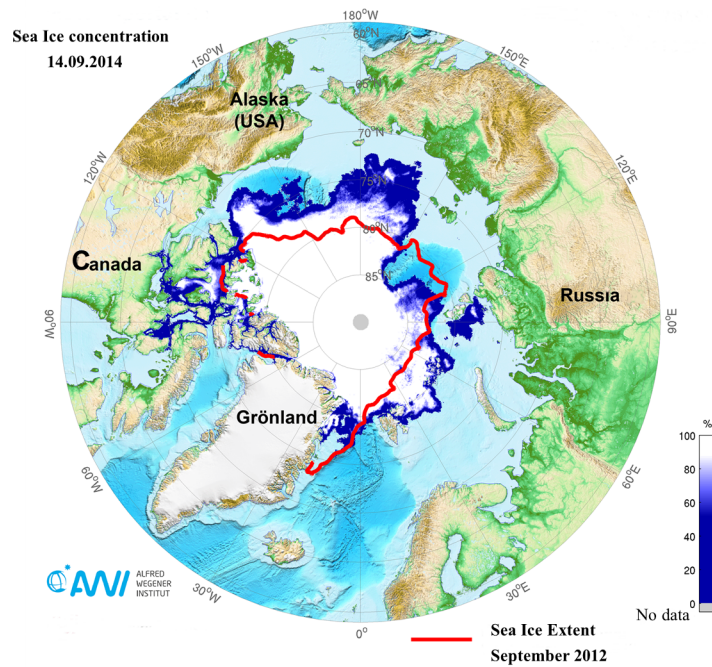


Figure 3.2: Current arctic sea ice extent with its lowest point reached in September 2012.

The image is obtained, with modifications, from the Alfred Wegener Institute website.

3.2 Scattering Mechanisms

Introducing the physical model of sea ice and its relative electromagnetic behavior, we consider it important to recall the main scattering mechanism models.

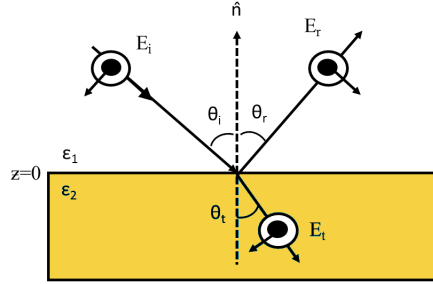


Figure 3.3: Classical problem of reflection and transmission at a plane dielectric interface.

The image, is obtained, with modifications, from [4].

To explain the backscattering and its corresponding scattering type, for a single pixel, is the heart of the Decomposition Theorems in Radar Polarimetry. It is easy to understand that the better defined are the scattering models, the better will be the corresponding interpretation.

3.2.1 Surface Scattering

Surface scattering occurs when an electromagnetic wave strikes a surface. This scattering type is strongly affected by the surface geometrical properties. The surface small-scale geometric shape, also called roughness can be statistically characterized by its root mean square h relative to a mean flat surface. Typically, a surface is statistically characterized by the surface height autocorrelation function. The surface correlation length ℓ is the separation after which the deviation from the mean surface for two points are statistically independent and mathematically is defined as the length after which the autocorrelation function is less than $1/e$ [8]. In order to describe in detail the surface scattering it is important to start from the Fresnel equations, the solutions of the classical problem of reflection and transmission at a plane dielectric interface [4]. This problem is summarized in Figure[3.3]. Fresnel equations together with Snell's Law describe the behavior of light when moving between different media. For simplicity we are considering only the horizontal polarization case, also called Transverse Electric problem, TE. The upper medium and lower medium are characterized by the dielectric constants ε_1 and ε_2 , respectively. From the basic laws of electromagnetism, the reflected wave is such that the angle of incidence equals the angle of reflection, and the transmitted wave obeys Snell's law, given by:

$$\frac{n_1}{n_2} = \frac{\sin \theta_t}{\sin \theta_i} n = \sqrt{\varepsilon_r} \quad (3.1)$$

where n is the refractive index and the subscripts i , r , and t indicate incidence angle, reflected angle and transmitted angle, respectively. For each polarization

combination we have two unknowns: the reflected and transmitted electric field components [4]. A solution can be obtained using the continuity equations, matching the tangential components of \mathbf{E} and \mathbf{H} at the interface $z = 0$:

$$H_r^S \cos \theta_r - H_i^S \cos \theta_i = -H^S \cos \theta_t \quad (3.2)$$

In this way, we obtain two equations for the two unknown coefficients:

$$\begin{aligned} E_i^H + E_r^H &= E_t^H \\ n_1(E_i^H - E_r^H) \cos \theta_i &= n_2 E_t^H \cos \theta_t \end{aligned} \quad (3.3)$$

Transverse Magnetic problem, TM, or rather the vertical polarization case, can be resolved with an analogue procedure. Combining the TM and TE problem solutions we can obtain the reflection \mathbf{R} and transmission \mathbf{T} matrices, also called Fresnel equations:

$$\mathbf{R} = \begin{bmatrix} R_{hh} & 0 \\ 0 & R_{vv} \end{bmatrix} \quad \mathbf{T} = \begin{bmatrix} T_{hh} & 0 \\ 0 & T_{vv} \end{bmatrix} \quad (3.4)$$

where:

$$R_{hh} = \frac{n_1 \cos \theta_i - n_2 \cos \theta_t}{n_1 \cos \theta_i + n_2 \cos \theta_t} \quad R_{vv} = \frac{n_2 \cos \theta_i - n_1 \cos \theta_t}{n_2 \cos \theta_i + n_1 \cos \theta_t} \quad (3.5)$$

$$T_{hh} = \frac{2n_1 \cos \theta_i}{n_1 \cos \theta_i + n_2 \cos \theta_t} \quad T_{vv} = \frac{2n_1 \cos \theta_i}{n_2 \cos \theta_i + n_1 \cos \theta_t} \quad (3.6)$$

It is possible to reformulate the reflection Fresnel coefficients using the Snell's law and considering the upper medium as free space $\varepsilon_1 = 1$. In this way, we arrive to the most common expression in radar scattering problems:

$$R_{hh} = \frac{\cos \theta_i - \sqrt{\varepsilon_2 - \sin^2 \theta_i}}{\cos \theta_i + \sqrt{\varepsilon_2 - \sin^2 \theta_i}} \quad R_{vv} = \frac{\varepsilon_2 \cos \theta_i - \sqrt{\varepsilon_2 - \sin^2 \theta_i}}{\varepsilon_2 \cos \theta_i + \sqrt{\varepsilon_2 - \sin^2 \theta_i}} \quad (3.7)$$

3.2.1.1 Single-Bounce Scattering

Now we recall the polarization properties of the scattering matrix for rough surfaces. We start considering that a perfectly smooth surface has zero backscatter for oblique incidence. However, most natural surfaces are not smooth and their backscattering is always observed. The followed procedure is described by the Physical Optics, PO, that consists of estimating the currents induced on the surface. PO assumes that the current induced on any surface element of finite size L is the same of that induced on an infinite tangent plane. The only change from the Fresnel equations is then to account for the finite extent L of the surface and this means that integrals over the surface must be considered [4]. Considering a simple uniform current of limited physical extent L we obtain the following expression for the scattered field:

$$S(\theta, \lambda) = \frac{2\sqrt{\pi}L}{\lambda} \cos \theta \cdot \frac{\sin(\beta L \sin \theta)}{\beta L \sin \theta} \begin{bmatrix} S_{hh}(\theta, \varepsilon_r) & 0 \\ 0 & S_{vv}(\theta, \varepsilon_r) \end{bmatrix} \quad (3.8)$$

where :

$$S_{hh} = \frac{\sqrt{\varepsilon_2 - \sin^2 \theta} - \cos \theta}{\cos \theta + \sqrt{\varepsilon_2 - \sin^2 \theta}} \quad S_{vv} = \frac{\varepsilon_2 \cos \theta - \sqrt{\varepsilon_2 - \sin^2 \theta}}{\varepsilon_2 \cos \theta + \sqrt{\varepsilon_2 - \sin^2 \theta}} \quad (3.9)$$

It is important to recall that this expression is valid when $L \gg \lambda$, or rather in high frequency conditions, where the Physical Optics is valid. Otherwise, if $L \ll \lambda$, rather low frequency conditions, the *sinc* function and so the corresponding backscattering tend to zero. This surface scattering mechanism is also called Specular Surface Scattering [4]. The single bounce scattering can be summarized by the following figure:

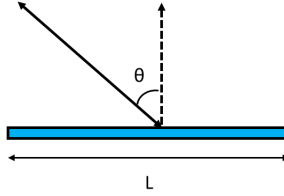


Figure 3.4: Geometry of Single-Bounce Scattering Mechanism.

3.2.1.2 Bragg Model

Until now we have considered rough surfaces without defining when a surface is called rough. Several criteria exist to decide if a surface is smooth or rough. The most commonly used one is the so-called Rayleigh criterion that classifies a surface as rough if the root mean square height satisfies $h > \lambda/8 \cos \theta$. When the surface facet is large compared to the wavelength, $L \gg \lambda$ but the surface is not smooth over the surface correlation length ℓ , a good model to describe this type of scattering is the *Small Perturbation Model*, *SPM*, often referred to as the *Bragg model*. In this case the solution for the scattered field can be obtained as a perturbation of that from the underlying smooth surface and an analytical solution obtained for the scattering matrix in terms of an infinite series [4]. A good approximation is obtained keeping only the first term of the series. In practice, this means to have :

$$\frac{2\pi}{\lambda} \cdot h < 0.3 \quad (3.10)$$

that constitutes a good low-frequency approximation, where λ is the wavelength of the incident wave. The scattered field from an arbitrary rough surface characterized by a height function $z(x, y)$, which satisfy the above defined approximation, is given by [4] :

$$\mathbf{E}_{pq}^S = i2\beta \cos \theta B_{pq} \hat{Z}(\beta_x + \beta \sin \theta, \beta_y) \quad (3.11)$$

where:

$$\begin{aligned}
B_{hh} &= \frac{(1 - \varepsilon_r) \cos \varphi_s}{\left(\cos \theta_s + \sqrt{\varepsilon_r - \sin^2 \theta_s} \right) \left(\varepsilon_r \cos \theta + \sqrt{\varepsilon_r - \sin^2 \theta} \right)} \\
B_{hv} &= \frac{-(1 - \varepsilon_r) \sin \varphi_s \sqrt{\varepsilon_r - \sin^2 \theta}}{\left(\cos \theta_s + \sqrt{\varepsilon_r - \sin^2 \theta_s} \right) \left(\varepsilon_r \cos \theta + \sqrt{\varepsilon_r - \sin^2 \theta} \right)} \\
B_{vh} &= \frac{(1 - \varepsilon_r) \sin \varphi_s \sqrt{\varepsilon_r - \sin^2 \theta}}{\left(\cos \theta_s + \sqrt{\varepsilon_r - \sin^2 \theta} \right) \left(\varepsilon_r \cos \theta + \sqrt{\varepsilon_r - \sin^2 \theta} \right)} \\
B_{vv} &= \frac{(1 - \varepsilon_r) \varepsilon_r \sin \theta \sin \theta_s - \sqrt{\varepsilon_r - \sin^2 \theta_s} \sqrt{\varepsilon_r - \sin^2 \theta} \cos \varphi_s}{\left(\varepsilon_r \cos \theta_s + \sqrt{\varepsilon_r - \sin^2 \theta_s} \right) \left(\varepsilon_r \cos \theta + \sqrt{\varepsilon_r - \sin^2 \theta} \right)} \\
\hat{Z}(\beta_x, \beta_y) &= \frac{1}{2\pi} \int \int z(x, y) e^{-i(\beta_x x + \beta_y y)} \partial x \partial y \quad (3.12)
\end{aligned}$$

where \hat{Z} is the Fourier Transform of the surface height autocorrelation function. Notice that \hat{Z} is a power spectral density.

$$\beta = \frac{2\pi}{\lambda} \quad \beta_x = -\beta \sin \theta_s \cos \varphi_s \quad \beta_y = -\beta \sin \theta_s \cos \sin \varphi$$

For the special case of backscatter we have:

$$\theta_s = \theta \quad \varphi_s = \pi \quad (3.13)$$

and then:

$$\mathbf{E}_{p,q}^S = i2\beta \cos \theta B_{pq} \hat{Z}(2\beta \sin \theta) \quad (3.14)$$

$$B_{hh} = \frac{\cos \theta - \sqrt{\varepsilon_r - \sin^2 \theta}}{\cos \theta + \sqrt{\varepsilon_r - \sin^2 \theta}} = R_{hh} \quad (3.15)$$

$$B_{hv} = B_{vh} = 0 \quad (3.16)$$

$$B_{vv} = \frac{(\varepsilon_r - 1) [\sin^2 \theta - \varepsilon_r (1 + \sin^2 \theta)]}{\varepsilon_r \cos \theta + \sqrt{\varepsilon_r - \sin^2 \theta}} \neq R_{vv} \quad (3.17)$$

The most important observation from the derived results is that the Bragg Model has the same reflection HH coefficient of the Fresnel Equations but the VV reflection coefficient is completely different. Also we can note that the surface roughness information is completely contained in \hat{Z} , which is common to all polarization channels. This shows the importance of Radar Polarimetry

that often considers the ratio of the polarization channels and so allows the cancellation of the roughness effects. We conclude with the final expression of the Bragg Coherency matrix \mathbf{T} . The corresponding \mathbf{k} -target vector is:

$$\boldsymbol{\kappa} = \frac{1}{\sqrt{2}} \begin{bmatrix} B_{hh} + B_{vv} & B_{hh} - B_{vv} & 0 \end{bmatrix}^T \quad (3.18)$$

and so the form of the Bragg surface model Coherency matrix \mathbf{T} is given by:

$$\mathbf{T}_s = \langle \boldsymbol{\kappa} \boldsymbol{\kappa}^H \rangle = f_s \begin{bmatrix} 1 & \beta^* & 0 \\ \beta & |\beta|^2 & 0 \\ 0 & 0 & 0 \end{bmatrix} \quad (3.19)$$

where:

$$f_s = \frac{|B_{hh} + B_{vv}|^2}{2} \quad \beta = \frac{B_{hh} - B_{vv}}{B_{hh} + B_{vv}} \quad (3.20)$$

3.2.1.3 Double-Bounce Scattering

A particular case of specular scattering is the Double-Bounce scattering or also called Dihedral Scattering. This mechanism arises when we have two orthogonal surfaces shaping an angle of $\pi/2$. In this case, as shown in Figure [3.5], a wave is incident with an angle θ on the surface A and is reflected in according to the Fresnel equations, and then is incident on the second surface B at angle $\pi/2 - \theta$, [4]. It is possible to notice that the total angle of reflection is π . The total scattering matrix is simply the product of the Bragg scattering matrix of each bounce scattering matrix of the corresponding surface:

$$\mathbf{S} = [\mathbf{S}_A] \cdot [\mathbf{S}_B] = \begin{bmatrix} B_{hh(A)} B_{hh(B)} e^{i2\gamma_h} & 0 \\ 0 & B_{vv(A)} B_{vv(B)} e^{i2\gamma_v} \end{bmatrix} \quad (3.21)$$

In addition, the propagating factors, $e^{j2\gamma_h}$ and $e^{j2\gamma_v}$, are introduced to describe the propagation attenuation and phase changes. The corresponding \mathbf{k} -target vector is:

$$\boldsymbol{\kappa} = \frac{1}{\sqrt{2}} \begin{bmatrix} B_{hh(A)} B_{hh(B)} e^{i2\gamma_h} + B_{vv(A)} B_{vv(B)} e^{i2\gamma_v} & \dots \\ \dots & B_{hh(A)} B_{hh(B)} e^{i2\gamma_h} + B_{vv(A)} B_{vv(B)} e^{i2\gamma_v} & 0 \end{bmatrix} \quad (3.22)$$

$$\mathbf{T}_{db} = \langle \boldsymbol{\kappa} \boldsymbol{\kappa}^H \rangle = f_d \begin{bmatrix} |\alpha|^2 & \alpha & 0 \\ \alpha^* & 1 & 0 \\ 0 & 0 & 0 \end{bmatrix} \quad (3.23)$$

where:

$$f_d = \frac{1}{2} |B_{hh(A)} B_{hh(B)} + B_{vv(A)} B_{vv(B)}|^2 \quad (3.24)$$

$$\alpha = e^{i2(\gamma_h - \gamma_v)} \frac{B_{hh(A)} B_{hh(B)} - B_{vv(A)} B_{vv(B)}}{B_{hh(A)} B_{hh(B)} + B_{vv(A)} B_{vv(B)}}$$

The Double-Bounce scattering can be described by the following figure:

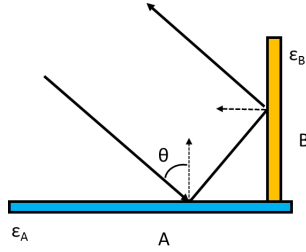


Figure 3.5: Geometry of Double-Bounce Scattering Mechanism.

3.2.1.4 Extended Bragg Model

The Bragg Model is a good model for surface scattering but has some limitations. The validity range of the Bragg scattering model is limited to the low roughness domain. In this way the Bragg model does not account the cross-polarized terms typical for rough natural surfaces. In order to extend the validity range of the Bragg Model we use the *Extended Bragg Model*, also called *X-Bragg Model*. Let us see the procedure in [4][12], in order to define this model. The procedure produces a smooth transition from the extreme case of a very rough surface up to a smooth surface:

$$\begin{array}{ccc} \textit{Rough Surface} & \rightarrow & \textit{Smooth Surface} \\ \beta \cdot h \gg 1 & & \beta \cdot h \ll 1 \end{array} \quad (3.25)$$

The transition is done considering the major perturbation to the smooth case arises from micro-variations in surface slope when the roughness increases.

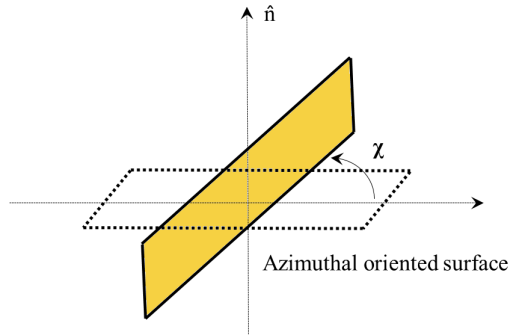


Figure 3.6: Azimuth slope $\bar{\chi}$ introduced in the X-Bragg model.
Image obtained and modified from [12].

This method consists of rotating the Bragg coherency matrix \mathbf{T} about an angle $\bar{\chi}$ in the plane perpendicular to the scattering plane and averaging over a particular distribution. In this sense $\bar{\chi}$ can be seen as the mean azimuth slope.

In fact, in the presence of a surface with azimuthal slope $\bar{\chi}$, the Bragg coherency matrix \mathbf{T}_s can be written as:

$$\mathbf{T}_s = \langle \boldsymbol{\kappa} \boldsymbol{\kappa}^H \rangle = f_s \begin{bmatrix} 1 & \beta^* & 0 \\ \beta & |\beta|^2 & 0 \\ 0 & 0 & 0 \end{bmatrix}$$

which when rotated, transforms to:

$$\begin{aligned} \mathbf{T}_s &= \begin{bmatrix} 1 & 0 & 0 \\ 0 & \cos 2\bar{\chi} & \sin 2\bar{\chi} \\ 0 & -\sin 2\bar{\chi} & \cos 2\bar{\chi} \end{bmatrix} \begin{bmatrix} 1 & \beta^* & 0 \\ \beta & |\beta|^2 & 0 \\ 0 & 0 & 0 \end{bmatrix} \begin{bmatrix} 1 & 0 & 0 \\ 0 & \cos 2\bar{\chi} & -\sin 2\bar{\chi} \\ 0 & \sin 2\bar{\chi} & \cos 2\bar{\chi} \end{bmatrix} = \\ &= \begin{bmatrix} 1 & \beta^* \cos 2\bar{\chi} & \beta^* \sin 2\bar{\chi} \\ \beta \cos 2\bar{\chi} & |\beta|^2 \cos^2 2\bar{\chi} & |\beta|^2 \cos 2\bar{\chi} \sin 2\bar{\chi} \\ -\beta \sin 2\bar{\chi} & -|\beta|^2 \cos 2\bar{\chi} \sin 2\bar{\chi} & |\beta|^2 \sin^2 2\bar{\chi} \end{bmatrix} \end{aligned} \quad (3.26)$$

Considering $\bar{\chi}$ randomly oriented, it is plausible to choose a uniform distribution:

$$p(\bar{\chi}) = \partial\bar{\chi}/\delta \quad \text{with} \quad \begin{array}{l} |\bar{\chi}| < \delta/2 \\ 0 \leq \delta \leq \pi \end{array} \quad (3.27)$$

In this sense, δ , the width of the distribution, is a measure of how much the roughness perturbs the Bragg model and for this reason is considered a measure of the surface roughness. Low values of δ indicate smooth surface while high values denote rough surface. Averaging \mathbf{T}_s over such a distribution:

$$\langle \mathbf{T} \rangle = \int \mathbf{T}_s(\bar{\chi}) p(\bar{\chi}) \partial\bar{\chi} \quad (3.28)$$

and calculating the following integrals:

$$T_{11} = \int p(\bar{\chi}) \partial\bar{\chi} = \frac{1}{\delta} \int_{-\delta/2}^{\delta/2} \partial\bar{\chi} = 1 \quad (3.29)$$

$$T_{12} = \int p(\bar{\chi}) \partial\bar{\chi} = \frac{1}{\delta} \int_{-\delta/2}^{\delta/2} \beta^* \cos 2\bar{\chi} \partial\bar{\chi} = \beta^* \text{sinc}(2\delta) \quad (3.30)$$

$$\begin{aligned} T_{13} &= \int \beta^* \sin 2\bar{\chi} p(\bar{\chi}) \partial\bar{\chi} = \frac{1}{\delta} \int_{-\delta/2}^{\delta/2} \beta^* \sin 2\bar{\chi} \partial\bar{\chi} = \\ &= \frac{\beta^*}{\delta} \left[-\frac{\cos 2\delta}{2} + \frac{\cos 2\delta}{2} \right] = 0 \end{aligned} \quad (3.31)$$

$$T_{21} = T_{12}^* = \beta \text{sinc}(2\delta) \quad (3.32)$$

$$T_{22} = \int |\beta|^2 \cos^2 2\bar{\chi} p(\bar{\chi}) \partial\bar{\chi} = \frac{1}{\delta} \int_{-\delta/2}^{\delta/2} |\beta|^2 \cos^2 2\bar{\chi} \partial\bar{\chi} =$$

$$= \frac{|\beta|^2}{\delta} \left[\frac{\delta}{2} + \frac{\sin 4\delta}{8} \right] = \frac{|\beta|^2}{2} (1 + \text{sinc}(4\delta)) \quad (3.33)$$

$$\begin{aligned} T_{23} &= \int |\beta|^2 \cos 2\bar{\chi} \sin 2\bar{\chi} p(\bar{\chi}) \partial\bar{\chi} = \frac{1}{\delta} \int_{-\delta/2}^{\delta/2} |\beta|^2 \cos 2\bar{\chi} \sin 2\bar{\chi} \partial\bar{\chi} = \\ &= \frac{|\beta|^2}{\delta} \left[-\frac{\cos 4\delta}{8} + \frac{\cos 4\delta}{8} \right] = 0 \end{aligned} \quad (3.34)$$

$$T_{31} = T_{13} = 0 \quad (3.35)$$

$$T_{32} = T_{23} = 0 \quad (3.36)$$

$$\begin{aligned} T_{33} &= \int |\beta|^2 \sin^2 2\bar{\chi} p(\bar{\chi}) \partial\bar{\chi} = \frac{1}{\delta} \int_{-\delta/2}^{\delta/2} |\beta|^2 \sin^2 2\bar{\chi} \partial\bar{\chi} = \\ &= \frac{|\beta|^2}{\delta} \left[\frac{\delta}{2} - \frac{\sin 4\delta}{8} \right] = \frac{|\beta|^2}{2} (1 - \text{sinc}(4\delta)) \end{aligned} \quad (3.37)$$

we can write the final expression of the X-Bragg coherency matrix $\mathbf{T}_{\mathbf{X}\mathbf{b}}$:

$$\mathbf{T}_{\mathbf{X}\mathbf{b}} = f_s \begin{bmatrix} 1 & \beta \text{sinc}(2\delta) & 0 \\ \beta^* \text{sinc}(2\delta) & \frac{1}{2} |\beta|^2 (1 + \text{sinc}(4\delta)) & 0 \\ 0 & 0 & \frac{1}{2} |\beta|^2 (1 - \text{sinc}(4\delta)) \end{bmatrix} \quad (3.38)$$

where f_s and β are given by Equation [3.20].

3.2.2 Volume Scattering

The second important class of polarimetric scattering is volume scattering. Volume scattering occurs when the medium contains local inhomogeneities that cause variations in dielectric properties. Inhomogeneities allow a penetration of the wave into the media. In this way, the wave is scattered and influenced from a distributed cloud of scatterers.

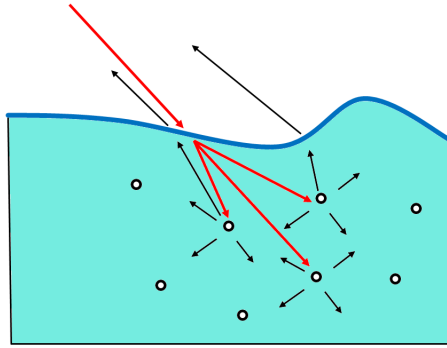


Figure 3.7: Geometry of the volume scattering mechanism.

Particularly important in volume scattering is the depth penetration that is related to dielectric properties and to the wavelength. The relative permittivity ε_r of a medium :

$$\varepsilon_r = \varepsilon' - j\varepsilon'' \quad (3.39)$$

is a complex number that characterizes the electrical properties of the media itself. The real part, ε' , is called dielectric constant and gives the contrast with respect to free space or air, where $\varepsilon'_{air} = 1$. The imaginary part, ε'' , is called dielectric loss factor and gives the electromagnetic loss of the material [13]. If we consider an electromagnetic plane wave propagating in the z direction, the intensity of the electric field at point z can be expressed as:

$$E(z) = E_0 e^{-\gamma z} \quad (3.40)$$

where E_0 is the intensity field at $z = 0$. The complex propagation constant of the medium is denoted by γ and is given by:

$$\gamma = \alpha + j\beta \quad (3.41)$$

where α is the absorption constant what describes the transformation of energy into other forms and β is the phase constant that is equal to the wave number $k = 2\pi/\lambda$ in a lossless medium. They are related to the complex permittivity by:

$$\alpha = k_0 |Im(\sqrt{\varepsilon})| \quad \beta = k_0 |Re(\sqrt{\varepsilon})| \quad (3.42)$$

where k_0 is the wave number in free space. Part of a wave incident upon the surface of a medium from the air in the z -direction is transmitted across the boundary into the medium. The penetration depth is defined as the depth at which the wave is attenuated to $1/e$:

$$\frac{P(z = \delta_p)}{P(z = 0)} = \frac{1}{e} \rightarrow \delta_p = \frac{\lambda}{2\pi n''} = \frac{\lambda}{2\pi |Im(\sqrt{\varepsilon_r})|} \quad (3.43)$$

Often, for most materials in microwave remote sensing the imaginary part is much smaller than the real part:

$$\frac{\varepsilon''}{\varepsilon'} < 0.1 \rightarrow \delta_p \simeq \frac{\lambda}{2\pi} \frac{\sqrt{\varepsilon'}}{\varepsilon''} \quad (3.44)$$

This condition is also called “good conductor” approximation. The penetration depth indicates the maximum depth of the medium that contributes to the backscattering. A complete dissertation would require finding the solution of Maxwell’s equations expanding the field in terms of vector spheroidal wave functions and matching the coefficients across the boundary for each layer of the medium. Finite elements, finite difference equations and T-matrix approximations are all valid methods to this purpose [24]. In the literature, there exists many models to describe volume scattering. In our work, we choose to use a model based on the Strong Fluctuation Theory under the first-order distorted

Born approximation for spheroidal and ellipsoidal scatterers with different orientation distributions, as discussed in [23]. Restarting from the form of the covariance matrix of a reciprocal medium with azimuth symmetry, we easily obtain the final form of the volume scattering covariance matrix \mathbf{C} :

$$\mathbf{C}_v = \begin{bmatrix} S_{hh}S_{hh}^* & \sqrt{2}S_{hh}S_{hv}^* & S_{hh}S_{vv}^* \\ \sqrt{2}S_{hh}^*S_{hv} & 2S_{hv}S_{hv}^* & \sqrt{2}S_{vv}^*S_{hv} \\ S_{hh}^*S_{vv} & \sqrt{2}S_{vv}S_{hv}^* & S_{vv}S_{vv}^* \end{bmatrix} = \quad (3.45)$$

$$= f_v \begin{bmatrix} 1 & 0 & \rho \\ 0 & (1-\rho) & 0 \\ \rho^* & 0 & 1 \end{bmatrix} \quad (3.46)$$

where:

$$\rho = \frac{S_{hh}S_{vv}^*}{\sqrt{S_{hh}S_{hh}^* \cdot S_{vv}S_{vv}^*}} \quad (3.47)$$

The corresponding coherency \mathbf{T} matrix is given by:

$$\mathbf{T}_v = f_v \begin{bmatrix} (1+\rho) & 0 & 0 \\ 0 & (1-\rho) & 0 \\ 0 & 0 & (1-\rho) \end{bmatrix} \quad (3.48)$$

The ρ parameter, also called shape parameter, is real and is included within [0, 1]. Values of ρ lower than 1/3 tend to indicate a prolate form of the scatterers, like dipoles, instead when ρ tends gradually to one the shape tends to be spherical. This characteristic will be particularly important for the Sea Ice. Values of ρ below 1/3 have difficult physical interpretation and so we will consider it included in [1/3,1].

3.3 Physical Model of Arctic Sea Ice

Sea ice is one of the most complex earth terrain. Sea ice is produced when seawater freezes and this occurs when the layer of air-seawater interface has a temperature about $-1.8^\circ C$. In remote sensing, materials of interest are generally classified into one of the following groups [13]:

1. Homogeneous substances
2. Electrolytic solutions
3. Heterogeneous mixtures

First group examples are pure water and ice, sea water and brine are representative materials for the second group and sea ice and snow for the third group. In this sense sea ice can be seen as a mixture of crystals, air pockets and liquid brine inclusions, while snow as a mixture of air, ice particles and possibly liquid

water inclusions [13]. The complexity of sea ice is attributed to its inhomogeneous composition, crystallography, structure, growth process, thermodynamic variations, and environmental effects [23]. Electromagnetic properties of sea ice are strongly related to the temperature and salinity. During the winter, near the top of the ice layer the temperature is low and the salinity is high. Moving into the middle of the ice the temperature increases, while the salinity decreases.

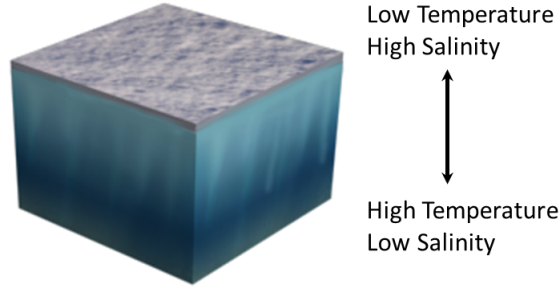


Figure 3.8: Temperature-salinity behavior of sea ice.

Particularly important is the sea ice growth that is determined by environmental conditions, winds and sea currents.

3.3.1 Sea Ice constituents

Let us see the most important sea ice constitutive elements. The following part is derived from [13].

Sea Water: Sea water has a complex permittivity that is exceptionally high. The dielectric behavior of pure water follows the Debye equation:

$$\varepsilon_w = \varepsilon_{w\infty} + \frac{\varepsilon_{w0} - \varepsilon_{w\infty}}{1 + j2\pi f\tau_w} \quad (3.49)$$

where ε_{w0} is the static dielectric of pure water, $\varepsilon_{w\infty}$ is the high-frequency limit of ε_w and τ is the relaxation time of pure water. Salts increase the dielectric loss of water adding free charges carriers. Hence, the loss factor of seawater includes an additional term due to ionic conductivity and the complex permittivity of seawater follows the modified Debye equation:

$$\varepsilon_{sw} = \varepsilon_{sw\infty} + \frac{\varepsilon_{sw0} - \varepsilon_{sw\infty}}{1 + j2\pi f\tau_{sw}} - j \frac{\sigma_{sw}}{\varepsilon_0} \quad (3.50)$$

where σ_{sw} is the ionic conductivity of sea water. Thus, we can consider sea water as the poorest emitter in sea ice scenes.

Freshwater Ice: Freshwater ice is free from salt, but usually it includes air bubbles and impurities. Pure ice, frozen distilled water, is an idealization

of freshwater ice. It has been experimentally shown that the relative dielectric constant of pure and freshwater ice is constant :

$$\varepsilon'_i = 3.17 \quad (3.51)$$

between 10 MHz and 1000 GHz.

Snow: many differences exist between dry snow and wet snow. Snow on ice serves as a thermal blanket, since snow has a thermal conductivity much less than that of sea ice. In addition, it may provides an impedance matching function and reduces the effects of surface roughness. Electromagnetically, dry snow is a dielectric mixture of ice and air and therefore its complex permittivity is governed by the dielectric properties of ice, snow density and ice particle shape. Since the real part of the permittivity of ice is practically independent of temperature, the dielectric constant of dry snow is only a function of density:

$$\varepsilon'_{ds} = \begin{cases} 1 + 1.9\rho_{ds} & \text{if } \rho_{ds} < 0.5 \text{ g/cm}^3 \\ 0.51 + 2.88\rho_{ds} & \text{if } \rho_{ds} \geq 0.5 \text{ g/cm}^3 \end{cases} \quad \text{between } 3 - 37\text{GHz} \quad (3.52)$$

where ρ_{ds} is the dry snow density. Electromagnetically, wet snow is a three-component dielectric mixture consisting of ice particles, air, and liquid water. The complex permittivity of ice and water depend on frequency and temperature, consequently, the permittivity of wet snow is a function of frequency, volumetric water content, snow density and the shape of ice particles.

Air Bubbles and Brine Pockets: air and brine inclusions play a key role in the formation of sea ice scattering mechanism. We will see later that air bubbles and brine pockets are characteristic of old and young ice, respectively.

3.3.2 Terminology

We consider it important to recall the main definitions of sea ice and furthermore its stage of development. The following part is derived from [21].

New Ice is a general term for recently formed ice which includes frazil ice, grease ice, slush, and shuga. These types of ice are composed of ice crystals which are only weakly frozen together and have a definite form only while they are afloat. It can be subdivided in:

- **Frazil Ice** : fine plates of ice suspended in water
- **Grease Ice** : a later stage of freezing than frazil ice where the crystals have coagulated forming a dense layer on the surface. The grease term derives from the opacity of this type of ice.

- **Slush** : snow which is saturated with water on ice surfaces.
- **Shuga** : an accumulation of soft white ice blocks having a diameter of a few centimeters across.

Nilas: a thin elastic crust of ice, easily flexible on waves and grow under pressure forming a tangled network of ice pieces. Nilas may be subdivided into dark nilas and light nilas:

- **Dark nilas** : nilas of very little thickness and which is very dark in color.
- **Light nilas** : thicker and lighter in color than dark nilas.

Young Ice: ice in transition stage between nilas and FY-ice. May be subdivided into grey ice and grey-white ice.

- **Grey-Ice** : young ice less elastic than nilas and easily breakable under pressure.
- **Grey-white ice** : young ice thicker than grey-ice which is more likely to ridge under pressure.

First-Year Ice: sea ice of not more than one winter's growth, developing from young ice. It may be subdivided into thin medium and thick first year ice.

Old Ice: sea ice which has survived at least one summer's melt. Typically is smoother than first-year ice. It may be subdivided into second year ice and multi-year ice:

- **Second Year Ice** : old ice which has survived only one summer's melt. Thicker than FY-ice and often out of water. In contrast to multi-year ice, summer melting produces a regular pattern of numerous small puddles.
- **Multi-Year Ice** : old ice which has survived at least two summer's melt. This ice is usually blue in color and salt free.

In Table [3.1] is reported the sea ice Stage of Development.

3.3.3 First-year Ice vs Multi-Year Ice

From our work perspective, it is important to analyze the physical differences between first-year ice and multi-year ice.

First-Year Ice

Ice growth begins with the formation of small platelets and needles, called frazil. As frazil crystals continue forming, a dense mixture of unconsolidated crystals and seawater is created, commonly referred to as grease ice. Under quiet conditions, the frazil crystal begin to coalesce, freezing together to form a solid elastic

Ice Type	Subtype	Thickness
<i>New Ice</i>		< 10 cm
	<i>Frazil Ice</i> <i>Grease Ice</i> <i>Slush</i> <i>Shuga</i>	
<i>Nilas</i>		< 10 cm
	<i>Dark Nilas</i> <i>Light nilas</i>	< 5 cm 5 ~ 10 cm
<i>Young Ice</i>		10 ~ 30 cm
	<i>Grey Ice</i> <i>Grey-White Ice</i>	10 – 15cm 15 ~ 30 cm
<i>First-Year (MY) Ice</i>		≥ 30 cm
	<i>Thin FY-Ice</i>	<i>First stage</i> 20 ~ 50 cm <i>Second Stage</i> 50 ~ 70 cm
	<i>Medium</i> <i>Thick</i>	70 ~ 120 cm > 120 cm
<i>Old Ice</i>		~ 2 m
	<i>Second year Ice</i> <i>Multi-Year (MY)Ice</i>	~ 2 m ~ 2 m

Table 3.1: Sea Ice Stage of Development.

cover, called nilas [32]. The action of wind and sea waves should not be underestimated. Arctic weather is very unfriendly and usually the wind speed is near to 4 and 6 m/s, but during the snow storms can reach 25 m/s. The joined action of wind and waves causes the formation of pancake ice, which consists of circular masses of semiconsolidated frazil. The final crystal structure that develops contains vertically elongated columnar crystals aligned to the direction of heat flow and having their axis generally orthogonal to the ice-water interface. Each of these elongated crystals contain a particular substructure. Within each grain, pure ice plates are separated by parallel layers of brine inclusions. This form of the columnar crystals is particularly important because it determines the vertical elongation of brine pockets and strongly influences the FY-Ice scattering mechanism.

Multi-Year Ice

Multi-year ice, MY-Ice, is old ice which has survived at least two summer's melt. The most important process in sea ice evolution is the desalination. There are

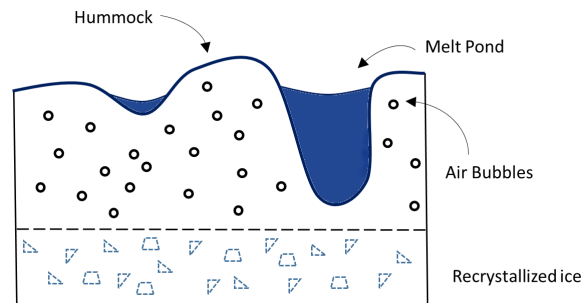


Figure 3.9: Cross Section of MultiYear-Ice.
The image is obtained, with modifications, from [26].

several desalination mechanisms: brine migration caused by thermal gradient, expulsion by pressure in brine pockets, drainage by gravity, and flushing by surface meltwater [23]. The main effects of salinity decrease can be summarized as a significant decreasing in the brine inclusion volume and their corresponding enlargement that implies a formation of drainage channels and a density reduction. Melting snow and ice provide a source of fresh water that percolating through the ice, contributes to the salinity reduction of the upper layer. Furthermore, warming causes a retexturing of the crystals that become more rounded and there is an increasing of the porosity of the upper layers [32]. During the melt season the drainage channels born from the desalination process, will be partially empty. During freezing time, the characteristic air bubbles of MY-Ice will be the remaining empty regions of the drainage channels formed in summer. From this it is possible to explain two facts: the typical vertical orientation of the air bubbles and the tangled network of air bubbles near the surface. Multiyear ice is typically composed of three scattering features [32]: hummocks, melt ponds and ridges. To analyze the MY-Ice structure in terms of hummocks and melt ponds is important because their physical differences serve to illustrate the importance of the upper layer characteristics that determine the microwave signature for MY-Ice. Figure [3.9] shows a schematic cross section of MY-Ice. It is possible to notice that hummock surface can be modeled as convex while the melt pond surface can be seen as concave. Typically, hummock surfaces are exposed to more solar radiation and will melt a significant amount of water and the desalination process will be more significant than in melt ponds. In fact, the concave surface of melt pond ice does not allow a significant formation of a drainage network [30]. This confirms the dense population of air bubbles in hummock ice compared than the melt ponds. Melt pools typically are very smooth surface and so the corresponding backscatter will be weak. It has been shown that backscatter of hummock and melt pool differs in intensity by a factor about 32 [26]. The typical size of air bubbles is approximately less than 2 mm, so air bubbles can be modeled as Rayleigh scatterers. Several studies have been done about the air bubbles shape [28][30]. The typical assumption

for MY-Ice air bubbles is a non perfect spherical shape, but many studies show a more realistic oblate shape.

Summary

From an electromagnetic perspective, the most important difference between FY and MY ice is the salinity. FY-Ice has high salinity, particularly near the surface. MY-Ice, because of the desalination process, can be considered with zero-salinity. The salinity strongly influences backscattering. High values of salinity corresponds to high values of dielectric loss factor. Otherwise, low values of salinity corresponds to low values of dielectric loss factor. For this reason, FY-Ice scattering can be mainly modeled as surface scattering and MY-Ice scattering as volume scattering.

$$FY - ice : \uparrow \text{Salinity} \rightarrow \uparrow \varepsilon'' \downarrow \delta_p \rightarrow \text{Surface Scattering}$$

$$MY - ice : \downarrow \text{Salinity} \rightarrow \downarrow \varepsilon'' \uparrow \delta_p \rightarrow \text{Volume Scattering}$$

Although, the main scattering mechanism for FY-Ice is surface scattering, there may also be a portion of volume scattering. This component is caused by the presence of brine pockets. In this sense, studies about the size distribution of brine pockets are very important. One of these, is surely the work presented in [28] where it has been affirmed that brine pockets are more elongated than air bubbles. If we assume an oblate shape for air bubbles we may consider a prolate, needle-like, shape for brine pockets. This clearly shows the importance of the shape parameter ρ defined in the volume scattering matrix of Equation [3.47]. In this sense we can see ρ as an ulterior parameter in order to discriminate MY-Ice and FY-Ice. Another important difference between FY and MY ice is the thickness. Arctic FY-Ice grows to a maximum thickness about 2 m in a single season [32]. Arctic MY-Ice shows a mean thickness in the interval of 3 and 4 meters. In addition, the surface features are very different. Typically deformed FY-Ice is characterized by sharp ridges and blocks. MY-Ice typically shows smoothed deformations caused by the action of the time.

3.3.4 Polarimetric Parameters of interest of Sea Ice

We conclude the Arctic Sea Ice chapter with its most important polarimetric signatures. The following part is derived from [22]. A typical problem for many ice types is that the HH and VV intensities, often, show the same characteristics. Nevertheless, the HH channel can be used to discriminate rough and smooth level ice better than VV channel. The cross-pol intensity, $|S_{hv}|^2$, is not sensitive to the incidence angle and is relatively independent of wind conditions compared to HH or VV.

Span:

$$SPAN = |S_{hh}|^2 + |S_{vh}|^2 + |S_{hv}|^2 + |S_{vv}|^2 \quad (3.53)$$

The total power, typically is greater for MY than FY ice due to the fact the MY-Ice gives an additional depolarized component of backscatter along with the predominantly co-pol returns from FY-Ice of equivalent surface roughness.

Geometric Brightness:

$$GB = \sqrt[d]{\det(\mathbf{C})} \quad (3.54)$$

where d is the number of polarimetric channels in \mathbf{C} . The geometric brightness is another way of representing the total power of the multi-channel radar. It is the geometric mean of all channels, while Span is arithmetic. This parameter is sensitive to the roughness, geometric shape and orientation of the illuminating target.

Phase difference: It is the most important polarimetric parameter that shows the correlation of the two-copol returns :

$$\theta_{hh-vv} = \arctan \left| \frac{\text{Im} \{ \langle S_{hh} S_{vv}^* \rangle \}}{\text{Re} \{ \langle S_{hh} S_{vv}^* \rangle \}} \right| \quad (3.55)$$

If the surface is lossy, the co-pol phase term becomes negative and with increasing negative phase difference with increasing the incidence angle. This parameters increases with the increasing of the dielectric constant of the surface. Thus, the co-pol phase difference in the range of 45-50 is largest for open water and typically around -5 at L-band.

Co-Polarization Ratio:

$$R_{vv/hh} = \frac{\langle S_{vv} S_{vv}^* \rangle}{\langle S_{hh} S_{hh}^* \rangle} \quad (3.56)$$

Its value is determined by the dielectric constant of the surface. It is useful to separate open water from thin-ice types. First-year and multi-year ice have values about 1. Open water and new ice have the largest observed values.

Cross-Polarization Ratio:

$$R_{hv/gb} = \frac{\langle S_{hv} S_{hv}^* \rangle}{GB} \quad (3.57)$$

The cross-polarization ratio has been shown to be useful to distinguish ice types and estimating ice age.

Optimum frequency, polarization, and incidence angle

Frequency, polarization and incidence angle are key factors in remote sensing of sea ice. In this sense it is legitimate to ask if there exists an optimum frequency, polarization and incidence angle. Before answering, let us see the typical frequency bands used in sea ice remote sensing.

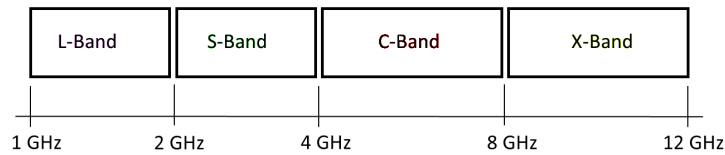


Figure 3.10: Typical frequency bands used in sea ice remote sensing.
The frequency bands information are taken from [17].

During winter the most critical point is discriminating FY-Ice and MY-Ice. This can be done evaluating the dominating scattering mechanism: volume or surface scattering. Reminding that in Rayleigh region the radar cross section increase as λ^6 we can choose an opportune wavelength in order to have surface scattering as the main scattering mechanism. Also the wavelength should be short enough to have a strong volume scattering. Observations and predictions argue that discrimination at C-Band will be much better than at L-Band and that results at X-Band will be similar to those at C-Band but with additional dynamic range. The ability to discriminate improved with decreasing frequency with the greatest separation at L-Band. For all season capability, selection of a C-Band frequency is a very reasonable choice when we operate with only a single frequency [26]. For many ice types, VV and HH intensities are very similar. However, VV channel shows 5 to 7 db more than HH channel for calm open water. VV channel shows also 2 to 3 db than HH channel for very thin ice. MY-Ice shows more depolarization than FY-Ice and so the Cross-polarization has been shown to increase the range between MY and FY ice returns by an additional 3 db. This is attributed to the very weak depolarization that occurs for smooth and slightly rough surfaces. A priori, there does not exist an exact optimum value of the incidence angle. The best solution would be to have more incident angle observations. Anyway, the optimum incidence angle range is from 20 to 70 degrees. Normal incident angles are dominated by surface scattering and coherence effects. The worst range is from 10 to 15 degrees, where the main scattering mechanism is not very well defined [26].

Chapter 4

Polarimetric Decomposition Theorems

Having defined the Coherency \mathbf{T} and Covariance \mathbf{C} matrices in Chapter 2, now we can introduce the “Target decomposition theorems” well-known in radar polarimetry. These theorems have the goal of understanding the scattering mechanisms corresponding to the polarimetric signatures in PolSAR images. There are many types of these decomposition theorems. We shall cite the most important:

- Model-based decomposition
- Eigenvalue-Eigenvector decomposition
- Scattering matrix \mathbf{S} coherent decomposition

In our work, we shall focus only on the model-based decompositions but we will briefly recall the Eigenvector-based decomposition and the coherent decomposition because they will be useful later.

4.1 Coherent Decompositions

Coherent decompositions have the goal of representing the scattering matrix \mathbf{S} as a combination of basis matrices corresponding to N canonical scattering mechanisms [10][19].

$$\mathbf{S} = \sum_{i=1}^N \alpha_i \mathbf{S}_i \quad (4.1)$$

Now we consider only the most important coherent decomposition: the Pauli decomposition. In this decomposition the scattering matrix \mathbf{S} is expressed as sum of the complex Pauli matrix basis set, defined in Equation [2.25]:

$$\mathbf{S} = \begin{bmatrix} S_{hh} & S_{hv} \\ S_{vh} & S_{vv} \end{bmatrix} = \alpha [\mathbf{S}_a] + \beta [\mathbf{S}_b] + \gamma [\mathbf{S}_c] + \mu [\mathbf{S}_d] \quad (4.2)$$

where:

$$\mathbf{S}_a = \begin{bmatrix} 1 & 0 \\ 0 & 1 \end{bmatrix} \quad \mathbf{S}_b = \begin{bmatrix} 1 & 0 \\ 0 & -1 \end{bmatrix} \quad \mathbf{S}_c = \begin{bmatrix} 0 & 1 \\ 1 & 0 \end{bmatrix} \quad \mathbf{S}_d = \begin{bmatrix} 0 & -i \\ i & 0 \end{bmatrix}$$

$$\alpha = \frac{1}{\sqrt{2}}(S_{hh} + S_{vv}) \quad \beta = \frac{1}{\sqrt{2}}(S_{hh} - S_{vv}) \quad \gamma = \frac{1}{\sqrt{2}}(S_{hv} + S_{vh}) \quad \mu = \frac{1}{\sqrt{2}}(S_{hv} - S_{vh})$$

The Pauli decomposition provides four main scattering mechanisms:

1. Single or odd Bounce scattering from a sphere, a plate or a trihedral.
2. Double or even Bounce scattering from a dihedral oriented at 0 degrees.
3. Double bounce or even Bounce scattering from a dihedral oriented at $\pi/4$.
4. Antisymmetric components of \mathbf{S} .

From now on, we will consider the monostatic case, $S_{hv} = S_{vh}$, then $\mu = 0$ and the Span is given by:

$$Span = |S_{hh}|^2 + |S_{vv}|^2 + 2|S_{hv}|^2 = |\alpha|^2 + |\beta|^2 + |\gamma|^2 \quad (4.3)$$

The RGB color-coded is:

$$\mathbf{Red} = |\beta|^2 \quad \mathbf{Green} = |\gamma|^2 \quad \mathbf{Blue} = |\alpha|^2 \quad (4.4)$$

4.2 Eigenvector-based Decompositions

Eigenvector-decomposition is based on the eigenstructure of the coherency \mathbf{T}_3 matrix. In the first chapter we have mentioned the properties of \mathbf{T} and \mathbf{C} matrices which derived by the Hermitian property:

- The eigenvalues of a Hermitian matrix are real.
- A Hermitian matrix is positive semidefinite if and only if the eigenvalues are nonnegative.
- The eigenvectors of a Hermitian matrix corresponding to distinct eigenvalues are orthogonal.

From this it is possible to decompose the Coherency \mathbf{T}_3 matrix as:

$$\mathbf{T}_3 = \mathbf{U}_3 \mathbf{\Sigma}_3 \mathbf{U}_3^{-1} \quad (4.5)$$

where:

$$\mathbf{\Sigma}_3 = \begin{bmatrix} \lambda_1 & 0 & 0 \\ 0 & \lambda_2 & 0 \\ 0 & 0 & \lambda_3 \end{bmatrix} \quad (4.6)$$

$\lambda_1, \lambda_2, \lambda_3$ are the real and nonnegative eigenvalues of \mathbf{T}_3 and $\mathbf{U}_3 = [\mathbf{u}_1 \ \mathbf{u}_2 \ \mathbf{u}_3]$ is the special unitary transformation matrix defined in Equation [2.47]. It is

important to notice that $\lambda_1 > \lambda_2 > \lambda_3 > 0$. This decomposition associates each eigenvector of \mathbf{T}_3 to three deterministic scattering mechanisms: surface scattering, dihedral scattering and volume scattering. The eigenvector $[\mathbf{u}_i]$, specifies the type of scattering mechanism and the eigenvalue $[\lambda_i]$, specifies its relative magnitude [5]. In this way, we can write:

$$\mathbf{T}_3 = \sum_{i=1}^3 \lambda_i \mathbf{u}_i \mathbf{u}_i^H \quad (4.7)$$

$$Span = \lambda_1 + \lambda_2 + \lambda_3 \quad (4.8)$$

From the eigenvalues it is possible to define the pseudo probabilities P_i :

$$P_i = \lambda_i / \sum_{j=1}^3 \lambda_j \quad (4.9)$$

In this way we can define the following parameters:

Entropy:

$$H = - \sum_{i=1}^3 P_i \log_3(P_i) \quad (4.10)$$

The polarimetric scattering entropy is a statistical measure of the randomness of the scattering process. When the eigenvalues are equal we have $H = 1$ and this means that the scattering process is completely random. A high entropy value means that the target is represented by more than one scattering mechanism and they are equal in strength. A depolarizing surface is characterized by a non-zero entropy value. Low values means that the target is dominated by a single scattering mechanism and a weakly depolarizing scattering process. H is whitening [0,1].

Anisotropy:

$$A = \frac{\lambda_2 - \lambda_3}{\lambda_2 + \lambda_3} \quad (4.11)$$

The polarimetric anisotropy is the complementary parameter to the entropy. When the entropy is high is difficult to distinguish the scattering process and in such cases the anisotropy is very useful for to do this.

Mean angle alpha:

$$\bar{\alpha} = \sum_{i=1}^3 \alpha_i P_i \quad (4.12)$$

The $\bar{\alpha}$ parameter indicates the type of the average dominant scattering process occurring $[0^\circ - 90^\circ]$. Low values, $[40^\circ - 90^\circ]$, are interpreted as surface scattering. Values ranging from $[40^\circ \sim 53^\circ]$ are interpreted as volume scattering and the remaining region $[53^\circ, 90^\circ]$ determines when double bounce scattering occurs. The previous part has been derived from [22].

4.3 Model-Based Decompositions

The scattering matrix \mathbf{S} is only able to characterize the so-called coherent or pure scatterers. To describe distributed scatterers, we need some statistical descriptors. Precisely, second order polarimetric descriptors are the covariance \mathbf{C} and coherency \mathbf{T} matrices, described in Equations [2.30] and [2.31]. The basic idea behind the decomposition, model-based and eigenvector based, is to hypothesize that the measured covariance matrix can be modeled as the combination of a number of individual matrices representing scattering as predicted by physical models [34]. Now let us see the main model-based decomposition theorems.

4.3.1 Freeman and Durden Decomposition

Freeman and Durden decomposition is one of the most used model-based decomposition theorem in radar polarimetry. This decomposition considers three possible scattering mechanisms: volume, surface and double-bounce scattering [19]. Surface scattering is modeled as Bragg surface, described in Section [3.2.1.2]. The corresponding covariance \mathbf{C}_s matrix is given by:

$$\mathbf{T}_s = \langle \boldsymbol{\kappa} \boldsymbol{\kappa}^H \rangle = f_s \begin{bmatrix} 1 & \beta^* & 0 \\ \beta & |\beta|^2 & 0 \\ 0 & 0 & 0 \end{bmatrix} \quad (4.13)$$

where

$$f_s = \frac{|B_{hh} + B_{vv}|^2}{2} \quad \beta = \frac{B_{hh} - B_{vv}}{B_{hh} + B_{vv}} \quad (4.14)$$

Double-Bounce scattering is modeled by scattering from a dihedral corner reflector, described in Section [3.2.1.3]. The corresponding covariance \mathbf{C}_{db} matrix is given by:

$$\mathbf{T}_{db} = \langle \boldsymbol{\kappa} \boldsymbol{\kappa}^H \rangle = f_{db} \begin{bmatrix} |\alpha|^2 & \alpha & 0 \\ \alpha^* & 1 & 0 \\ 0 & 0 & 0 \end{bmatrix} \quad (4.15)$$

where

$$f_{db} = \frac{1}{2} |B_{hh(A)} B_{hh(B)} + B_{vv(A)} B_{vv(B)}|^2 \quad (4.16)$$

$$\alpha = e^{i2(\gamma_h - \gamma_v)} \frac{B_{hh(A)} B_{hh(B)} - B_{vv(A)} B_{vv(B)}}{B_{hh(A)} B_{hh(B)} + B_{vv(A)} B_{vv(B)}} \quad (4.17)$$

and $R_{1v}, R_{1h}, R_{2h}, R_{2v}$ are the Fresnel coefficients for the first surface and the second surface, respectively. The term $\exp \pm 2i(\gamma_h - \gamma_v)$ indicates the propagation effects and their relative phase changes. Volume scattering is modeled considering a cloud of randomly oriented very thin cylinder-like scatterers. The average covariance volume $\langle \mathbf{T}_v \rangle_\theta$ matrix is given by:

$$\langle \mathbf{T}_v \rangle_\theta = \frac{f_v}{2} \begin{bmatrix} 1 & 0 & 0 \\ 0 & 1/2 & 0 \\ 0 & 0 & 1/2 \end{bmatrix} \quad (4.18)$$

where the subscript θ indicates the average in respect to its probability function. Freeman and Durden decomposition considers an uniform distribution for the orientation angle θ :

$$p(\theta) = \partial\theta/2\pi \quad 0 \leq \theta \leq 2\pi \quad (4.19)$$

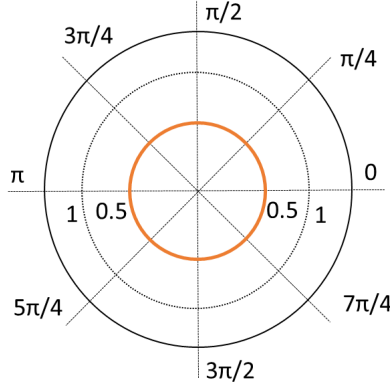


Figure 4.1: Uniform probability density function for the orientation angle θ in polar coordinates.

Appendix A gives the complete derivation of the volume covariance matrix. Considering the three scattering mechanisms are uncorrelated, the total covariance \mathbf{C} matrix is given by the sum of each covariance matrix:

$$\begin{aligned} \mathbf{T} &= \mathbf{T}_s + \mathbf{T}_{db} + \langle \mathbf{T}_v \rangle_\theta = \\ &= \begin{bmatrix} f_s + f_{db} |\alpha|^2 + \frac{f_v}{2} & f_s \beta^* + f_{db} \alpha & 0 \\ f_s \beta + f_{db} \alpha^* & f_s |\beta|^2 + f_{db} + \frac{f_v}{4} & 0 \\ 0 & 0 & \frac{f_v}{4} \end{bmatrix} \end{aligned} \quad (4.20)$$

Finally we can write the general form of the Freeman and Durden decomposition:

$$\langle [\mathbf{T}] \rangle = f_s [\mathbf{T}_{surface}] + f_{db} [\mathbf{T}_{double-bounce}] + f_v [\mathbf{T}_{volume}] \quad (4.21)$$

The system is undetermined having 4 equations in 5 unknowns. Subtracting the common term f_v , the system reduces to 3 equations in 4 unknowns, but it is always undetermined. It is clear that prior assumptions must be taken. vanZyl proposed in [33] a criterion to decide whether double-bounce or surface scatter is dominant based on the sign of the real part of the co-pol term of \mathbf{T} :

$$Double - Bounce : Re \{ S_{hh} S_{vv}^* \} \leq 0 \rightarrow \beta = +1$$

$$\text{Surface} : \text{Re} \{S_{hh}S_{vv}^*\} \geq 0 \rightarrow \alpha = -1$$

According to this criterion, fixing α or β , the system has the same number of equations and unknowns and so it is possible to find a unique solution. The Span and the corresponding powers associated with the three scattering mechanisms are given by:

$$\text{Span} = \text{Trace}(\mathbf{T}) = P_s + P_v + P_{db} \quad (4.22)$$

$$P_s = f_s(1 + |\beta|^2) \quad P_v = f_v \quad P_{db} = f_{db}(1 + |\alpha|^2)$$

The previous part has been derived from [19].

4.3.2 Non-Negative Eigenvalue Decomposition

Non-Negative Eigenvalue decomposition, NNED, is a hybrid decomposition proposed by vanZyl in [35]. Hybrid because it combines Eigenvalue decomposition and the traditional Model-Based Decomposition. This particular decomposition was born by the fact that Model-based Decomposition shows some pixels with negative powers. This is clearly physically meaningless. It is possible to show that negative power arises by an overestimation of the volume contribution. Negative power means that the covariance \mathbf{C} matrix has negative eigenvalues. NNED has the purpose to avoid the negativity of the eigenvalues. To do this, a scale parameter q is introduced. Let us see the mathematical procedure. Consider the following measured covariance $\langle \mathbf{C} \rangle$ matrix and the predicted covariance $[\mathbf{C}_{model}]$ matrix of the considered model-based decomposition :

$$\langle \mathbf{C} \rangle = \begin{bmatrix} \varepsilon & 0 & \rho \\ 0 & \eta & 0 \\ \rho^* & 0 & \xi \end{bmatrix} \quad [\mathbf{C}_{model}] = \begin{bmatrix} \varepsilon_m & 0 & \rho_m \\ 0 & \eta_m & 0 \\ \rho_m^* & 0 & \xi_m \end{bmatrix} \quad (4.23)$$

From the form of these matrices it is possible to notice that the reflection symmetry condition is assumed. The heart of this method consists of subtracting the predicted “model” covariance matrix, weighted by a real scale coefficient q , from the measured covariance $\langle \mathbf{C} \rangle$ matrix. In this way, the remainder covariance $[\mathbf{C}_{rem}]$ matrix can be written as:

$$[\mathbf{C}_{rem}] = \langle \mathbf{C} \rangle - q [\mathbf{C}_{model}] \quad (4.24)$$

$$[\mathbf{C}_{rem}] = \begin{bmatrix} \varepsilon & 0 & \rho \\ 0 & \eta & 0 \\ \rho^* & 0 & \xi \end{bmatrix} - q \begin{bmatrix} \varepsilon_m & 0 & \rho_m \\ 0 & \eta_m & 0 \\ \rho_m^* & 0 & \xi_m \end{bmatrix} \quad (4.25)$$

The real parameter q is the variable that makes it possible to avoid negative eigenvalues. This is achieved by maximizing q with the condition that the eigenvalues are non-negative. To do this means to find the maximum value of

q . If $q = 1$ we obtain exactly the original model-based decomposition. Let us write the eigenvalues of $[\mathbf{C}_{rem}]$, that are the roots of the following equation:

$$(\eta - \eta_m - \lambda) \left\{ \lambda^2 - (\varepsilon + \xi - q\varepsilon_m - q\xi_m)\lambda + (\varepsilon + q\varepsilon_m)(\xi - q\xi_m) - |\rho - \rho_m|^2 \right\} = 0 \quad (4.26)$$

$$\lambda_1 = \frac{1}{2}(Y + X)$$

$$\lambda_2 = \frac{1}{2}(Y - X)$$

$$\lambda_3 = \eta - q\eta$$

$$Y = \varepsilon + \xi - q\varepsilon_m - q\xi_m$$

$$X = \sqrt{Y^2 - 4(\varepsilon - \varepsilon_m)(\xi - \xi_m) + 4|\rho - \tau\rho_m|^2} \quad (4.27)$$

Since $\lambda_1 \geq \lambda_2$ the maximum value of q is found when the smallest renaming eigenvalue is equals to zero. To dictate $\lambda_2 = 0$ means to resolve the following quadratic equation:

$$(\varepsilon - q\varepsilon_m)(\xi - q\xi) = |\rho - q\rho_m|^2 \quad (4.28)$$

The corresponding roots are:

$$q_{1,2} = \frac{1}{2(\varepsilon_m\xi_m - |\rho_m|^2)} \cdot (Z \pm \sqrt{Z^2 - 4(\varepsilon_m\xi_m - |\rho_m|^2)(\varepsilon\xi - |\rho|^2)})$$

where :

$$Z = \varepsilon\xi_m + \xi\varepsilon_m - \rho\rho_m^* - \rho^*\rho_m \quad (4.29)$$

To dictate $\lambda_3 = 0$ means:

$$\eta - q\eta_m = 0 \quad (4.30)$$

Choosing the smallest roots among $[q_1, q_2, q_3]$ we obtain the value of q that provides non-negative eigenvalues:

$$q = \min \begin{cases} q_1 \\ q_2 \\ q_3 = \eta/\eta_m \end{cases} \quad (4.31)$$

Once the volume scattering has been removed, it is possible to continue using the traditional model-based decomposition. NNED considers an eigenvalue-decomposition for the total covariance \mathbf{C} matrix: can be written as:

$$\langle \mathbf{C} \rangle = \lambda_1 [\mathbf{C}_1] + \lambda_2 [\mathbf{C}_2] + \lambda_3 [\mathbf{C}_3] + \lambda_{diff} [\mathbf{C}_{diff}] \quad (4.32)$$

Now it is clear why we have called NNED an hybrid method. It is possible to obtain the intensities by :

$$\begin{aligned} I_{volume} &= Trace \{q [\mathbf{C}_{model}]\} \\ I_{surface} &= Trace \{\lambda_1 [\mathbf{C}_1]\} \\ I_{double-bounce} &= Trace \{\lambda_2 [\mathbf{C}_2]\} \end{aligned} \quad (4.33)$$

The last matrix $[C_{diff}]$ will include additional cross-polarized power that could represent terrain effects and rough surface scattering and typically this matrix is ignored. This section has been derived from [35].

4.3.3 Sea Ice Two-Component Decomposition

Now let us see a specific model-based decomposition developed for Sea Ice in [9]. This decomposition considers only two scattering mechanisms: surface scattering and volume scattering. Double-bounce scattering is typically negligible in sea ice scenes and for this reason it is not considered in this decomposition. Surface scattering is modeled with the Extended Bragg model and the volume model assumes randomly oriented scattering elements described by the shape parameter ρ . The coherence decomposition can be written as:

$$\mathbf{T} = f_s \mathbf{T}_s + f_v \mathbf{T}_v \quad (4.34)$$

where:

$$\mathbf{T}_s = \begin{bmatrix} 1 + |\beta|^2 & \beta \text{sinc}(2\delta) & 0 \\ \beta^* \text{sinc}(2\delta) & \frac{1}{2} |\beta|^2 (1 + \text{sinc}(4\delta)) & 0 \\ 0 & 0 & \frac{1}{2} |\beta|^2 (1 - \text{sinc}(4\delta)) \end{bmatrix} \quad (4.35)$$

$$\mathbf{T}_v = \begin{bmatrix} (1 + \rho) & 0 & 0 \\ 0 & (1 - \rho) & 0 \\ 0 & 0 & (1 - \rho) \end{bmatrix} \quad (4.36)$$

where all parameters are exactly the same as defined in Sections [3.2.1.4] and [3.2.2]. The form of \mathbf{T}_v denotes the assumption of azimuth symmetry. Azimuth symmetry is a strong assumption but for sea ice scenes is often valid. Span is given by:

$$Span = Trace \{ \mathbf{T} \} = f_s (1 + |\beta|^2) + f_v (3 - \rho) = P_s + P_v \quad (4.37)$$

Later, we will use a normalised form of the coherency \mathbf{T} matrix :

$$\tilde{\mathbf{T}}_s = \frac{1}{(1 + |\beta|^2)} \begin{bmatrix} 1 & \beta \text{sinc}(2\delta) & 0 \\ \beta^* \text{sinc}(2\delta) & \frac{1}{2} |\beta|^2 (1 + \text{sinc}(4\delta)) & 0 \\ 0 & 0 & \frac{1}{2} |\beta|^2 (1 - \text{sinc}(4\delta)) \end{bmatrix} \quad (4.38)$$

$$\tilde{\mathbf{T}}_v = \frac{1}{3 - \rho} \begin{bmatrix} (1 + \rho) & 0 & 0 \\ 0 & (1 - \rho) & 0 \\ 0 & 0 & (1 - \rho) \end{bmatrix} \quad (4.39)$$

The normalisation in respect to the total power entails that the Span is equals to one and f_v and f_s are between $[0, 1]$.

$$Span = Trace \{ \tilde{\mathbf{T}} \} \quad (4.40)$$

$$f_s + f_v = 1 \quad (4.41)$$

Assuming the two scattering mechanisms are uncorrelated, the total normalised coherency $\tilde{\mathbf{T}}$ matrix is given by the sum of each covariance matrix and we can redefine the Sea Ice Two-Component decomposition as:

$$\tilde{\mathbf{T}} = \begin{bmatrix} \tilde{T}_{11} & \tilde{T}_{12} & 0 \\ \tilde{T}_{21} & \tilde{T}_{22} & 0 \\ 0 & 0 & \tilde{T}_{33} \end{bmatrix} \quad (4.42)$$

where :

$$\tilde{T}_{11} = \frac{f_s}{(1 + |\beta|^2)} + f_v \frac{(1 + \rho)}{3 - \rho} \quad (4.43)$$

$$\tilde{T}_{22} = f_s \frac{|\beta|^2 (1 + \text{sinc}(4\delta))}{2(1 + |\beta|^2)} + f_v \frac{(1 - \rho)}{3 - \rho} \quad (4.44)$$

$$\tilde{T}_{33} = f_s \frac{|\beta|^2 (1 - \text{sinc}(4\delta))}{2(1 + |\beta|^2)} + f_v \frac{(1 - \rho)}{3 - \rho} \quad (4.45)$$

$$\tilde{T}_{12} = \frac{f_s \beta \text{sinc}(2\delta)}{(1 + |\beta|^2)} \quad (4.46)$$

This model has 5 unknowns f_v , f_s , β , δ , ρ but only 4 equations. To solve this system it is necessary to fix one parameter or to take some kind of prior assumptions. Otherwise, it is possible to use an optimisation algorithm. It is important to notice that the speckle has not been considered yet. Fixing one parameter, for example δ , we can find an algebraic solution, given by:

$$|\beta| = \frac{|T_{22} - T_{33}|}{|T_{12}| \cos(2\delta)} \quad (4.47)$$

$$\angle\beta = \angle T_{12} \quad (4.48)$$

$$f_s = \frac{|T_{12}| (1 + |\beta|^2)}{\beta \text{sinc}(2\delta)} \quad (4.49)$$

$$f_v = 1 - f_s \quad (4.50)$$

$$\rho = \frac{3|\beta|^2 [T_{11} - (T_{22} - T_{33})] + (2 - |\beta|^2) f_v}{|\beta|^2 [T_{11} - (T_{22} - T_{33})] + (2 + |\beta|^2) f_v} \quad (4.51)$$

Reminding that :

$$\beta = \frac{B_{hh} - B_{vv}}{B_{hh} + B_{vv}} \quad (4.52)$$

where R_{hh} and R_{vv} are reflections coefficients defined in Equations [3.15] [3.17],

we can see that β has an important physical meaning: it is related to the dielectric constant ε and the incidence angle θ . In particular, high values of β are expected by open water that has a high dielectric constant. In Chapter 3, during the X-Bragg model description, we have seen that δ is the parameter which controls the depolarization as well as the cross-polarized power level. If $\delta = 0$, the Extended-Bragg model converges to the Bragg model [11]. We can see δ as a measure of surface roughness. High values of δ denote rough surfaces while low values denote smooth surfaces. The limit of the X-Bragg model is the ambiguity given by the *sinc* function. To avoid this ambiguity we must choose δ below $\pi/4$. This fact should not be underestimated because it limits the surface roughness measure. The shape parameter ρ is the most critical parameter and it is the only one of the volume scattering model. Shape parameter ρ lies between $[0,1]$, but typical values are between $[1/3, 1]$ where low values denote volume scattering caused by prolate, needle-shape particles, or more simply dipoles, typical for the upper layer of new and first-year ice. High values of ρ are expected for volume scattering caused by oblate or spherical particles, like air-bubbles or brine-pockets typical for multi-year ice. For open water we expect high values of f_s and low values of δ . For smooth first-year ice we expect low values of ρ and low values of δ . First-year ice is characterized by strong surface scattering while multi-year ice by volume scattering. For this reason we expect high values of f_s and low values of f_v for first-year ice and the opposite for multi-year ice. Summarizing with the Sea Ice Two-Component decomposition it might be possible to discriminate open water, smooth and deformed first-year ice, and multi-year ice. A possible future work could be to apply a specific classification algorithm for sea ice scenes. In Chapter 7 we will see, in detail, the results for this decomposition.

4.4 Model-Based decompositions comparison

Now we see a brief review of the main model-based decompositions in order to evaluate their advantages and disadvantages.

Freeman and Durden Decomposition

The main advantages of the Freeman and Durden decomposition are the relative simplicity and that it is mainly based on the physics of the scattering mechanisms. The Freeman and Durden decomposition is particularly useful for earth terrain and forest scenes, but is not for sea ice scenes. Previously, we have showed that the volume scattering contribution is modeled considering randomly oriented dipoles. In some regions, for example vegetated areas, volume contribution tends to be overestimated causing negative power associated to surface or double-bounce scattering and so causing a loss of physical meaning. Another possible deficiency of the Freeman and Durden decomposition is the reflection symmetry assumption that is not always valid, specially in urban areas. From our work perspective, the most critical point is the need to take “prior” assumption that allows to find an unique solution for this model. Our goal is

precisely to find a way to avoid this kind of assumption using the fourth-order statistical moments. This point will be more clear in the next chapter.

Non Negative Eigenvalue Decomposition

The Non Negative Eigenvalue decomposition allows to avoid the problem of negative power that occurs in Freeman and Durden decomposition. NNED is particularly used for forest land scenes. One of NNED problems is that the cross-polarized power is ignored. This power could be useful to measure the surface roughness, particularly used in sea ice scenes where surface scattering is typically dominant. Later, we will show the results for NNED applied to Freeman and Durden and Sea Ice Two-Component decompositions and we will show if it is possible to obtain extra information using the fourth-order statistics.

Sea Ice Two-Component Decomposition

The Sea Ice Two-Component decomposition has the goal to introduce a specific decomposition for sea ice scenes. To model sea ice polarimetric signatures is very challenging, because, as previously described, the scattering mechanism is different for new ice and multi-year ice and is dependent from the particular physical structure of these two types of ice. Double-bounce scattering typically is not prevalent in sea ice scenes and this is the reason because it is ignored in this decomposition. The Sea Ice Two-Component improves the typical surface scattering model using the Extended Bragg surface model, also known as X-Bragg model. Volume scattering is modeling through the ρ parameter, defined in Section [3.2.2]. This decomposition has more unknowns than equations and to find an unique solution is necessary to fix one parameter or make prior assumptions, typical for model-based decompositions. The Sea Ice Two-Component decomposition has been the first decomposition in [7] where it has been shown that fourth-order statistics can improve traditional model-based decompositions, removing prior assumptions. This point will be more clear in the next chapter where we will explain the theory and the procedure behind the use of higher-order statistics.

Chapter 5

Model-Based Decomposition with Higher-Order Statistics

In this chapter we will briefly recall the most important concept about the statistics of PolSAR data and then we will show the heart of our work describing the high-order statistics approach applied to the model-based decompositions. We will give particular emphases to the Sea Ice Two-Component decomposition because it is the decomposition chosen by us to demonstrate the usefulness of the higher-order statistics. Then we will apply the same method to the Freeman and Durden decomposition.

5.1 PolSAR Data Statistics

In Section [2.3.2] we have seen the expressions of the covariance and coherency matrices, obtained after the multilooking process that for simplicity we rewrite it:

$$\mathbf{C}_\Omega = \frac{1}{L} \sum_{i=1}^L \boldsymbol{\Omega}_i \boldsymbol{\Omega}_i^H \quad \mathbf{C}_\kappa = \frac{1}{L} \sum_{i=1}^L \boldsymbol{\kappa}_i \boldsymbol{\kappa}_i^H$$

where L is the nominal number of looks. These two quantities are typically used to represent Multilook PolSAR data. It is usual to assume that the scattering vectors, $\boldsymbol{\Omega}$ or $\boldsymbol{\kappa}$, have zero mean and are circular complex multivariate Gaussian distributed :

$$\boldsymbol{\Omega} \sim \mathcal{N}_d^{\mathbb{C}}(\mathbf{0}, \boldsymbol{\Sigma}_\Omega) \quad \boldsymbol{\kappa} \sim \mathcal{N}_d^{\mathbb{C}}(\mathbf{0}, \boldsymbol{\Sigma}_\kappa) \quad (5.1)$$

where $\mathbf{0}$ is a column vector of zeros, d is the dimension of $\boldsymbol{\Omega}$ or $\boldsymbol{\kappa}$ and

$$\boldsymbol{\Sigma}_\Omega = E[\boldsymbol{\Omega} \boldsymbol{\Omega}^H] \quad \boldsymbol{\Sigma}_\kappa = E[\boldsymbol{\kappa} \boldsymbol{\kappa}^H] \quad (5.2)$$

are the covariance matrices of $\mathbf{\Omega}$ and $\mathbf{\kappa}$, respectively. The PDF of $\mathbf{\Omega}$ and $\mathbf{\kappa}$ are given by:

$$p_{\mathbf{\Omega}}(\mathbf{\Omega}; \mathbf{\Sigma}) = \frac{1}{\pi^d |\mathbf{\Sigma}_{\mathbf{\Omega}}|} \exp(-\mathbf{\Omega}^H \mathbf{\Sigma}_{\mathbf{\Omega}}^{-1} \mathbf{\Omega}) \quad (5.3)$$

$$p_{\mathbf{\kappa}}(\mathbf{\kappa}; \mathbf{\Sigma}) = \frac{1}{\pi^d |\mathbf{\Sigma}_{\mathbf{\kappa}}|} \exp(-\mathbf{\kappa}^H \mathbf{\Sigma}_{\mathbf{\kappa}}^{-1} \mathbf{\kappa}) \quad (5.4)$$

where $|\cdot|$ is the matrix determinant. If $L \geq d$ and the $\mathbf{\Omega}$ and $\mathbf{\kappa}$ are independent and then we can define the scaled covariance and coherency matrix as:

$$\mathbf{Z} = L\mathbf{C}_{\mathbf{\Omega}} \quad \mathbf{Z} = L\mathbf{C}_{\mathbf{\kappa}} \quad (5.5)$$

that are complex Wishart distributed:

$$p_{\mathbf{Z}}(\mathbf{Z}; L, \mathbf{\Sigma}) = \frac{|\mathbf{Z}|^{L-d}}{|\mathbf{\Sigma}|^L \Gamma_d(L)} \exp(-\text{trace}(\mathbf{\Sigma}^{-1} \mathbf{Z})) \quad (5.6)$$

where $\mathbf{\Sigma} = E[\mathbf{Z}]/L = E[\mathbf{C}_{\mathbf{\kappa}, \mathbf{\Omega}}]$. $\Gamma_d(L)$ is the multivariate Gamma function that plays as a normalisation factor and it is given by:

$$\Gamma_d(L) = \pi^{d(d-1)/2} \prod_{i=0}^{d-1} \Gamma(L-i) \quad (5.7)$$

where $\Gamma(L)$ is the standard Euler gamma function. Summarizing we can write:

$$\mathbf{Z} \sim \mathcal{W}_d^{\mathbb{C}}(L, \mathbf{\Sigma}) \quad (5.8)$$

5.1.1 Product model and Texture

The randomness of a SAR measurement is mainly attributed to two unrelated factors, speckle and texture [2]. The texture is the spatial variation of the radar cross section, which can be associated with a group of scatterers. Gaussian models do not consider the texture but only the speckle. In this sense, many statistical models include the texture as a separate random variable. This family of models is called *product model* and it has been shown to be a successful model of SAR signals. Before exploring the PolSAR product model it is useful to recall the product model for single channel SAR. In Section [2.3.2] we have seen the multiplicative noise model for speckle for single-look data. As described in [25], for L-looks, the intensity I can be represented as the product of the RCS with a speckle term w whose PDF is given by:

$$p(w) = \frac{L^L w^{L-1}}{\Gamma(L)} e^{-Lw} \quad (5.9)$$

This model forms the basis of reconstruction filters and segmentation methods but always derives from the product model that we write as:

$$S = \sqrt{\sigma} w \quad (5.10)$$

where S represents the observed complex SAR data, w is the speckle modeled as circular zero-mean complex Gaussian with unit variance and σ is the RCS. The intensity data is given by :

$$I = |S|^2 = \sigma |w|^2 \quad (5.11)$$

Now we can introduce the PolSAR data product model, that is also called the multivariate product model. Using the same procedure in [37] we can write the scattering vector, $\boldsymbol{\kappa}$ or $\boldsymbol{\Omega}$, as a product of two independent stochastic processes :

$$\boldsymbol{\kappa} = \sqrt{\tau} \mathbf{w} \quad \boldsymbol{\Omega} = \sqrt{\tau} \mathbf{w} \quad (5.12)$$

The \mathbf{w} process is the speckle:

$$\mathbf{w} \sim \mathcal{N}_d^{\mathbb{C}}(\mathbf{0}, \boldsymbol{\Sigma}_{\mathbf{w}}) \quad (5.13)$$

while the second process is the texture. The PDF of the texture is arbitrary, but its mean is always unitary :

$$E[\tau] = 1 \quad (5.14)$$

In the literature, it is possible to find many studies about the PDF of the polarimetric texture. The best PDF choice is not unique and it depends on the particular scene analyzed. Two of these possible choices are the Gamma distribution and the Dirac delta distribution. If τ is Gamma distributed the scattering vector follows the K-distribution while if τ is constant, Dirac delta distributed, the scattering vector follows the Gaussian distribution. However, we can always consider the texture independent of the polarization. In the multilook domain, the product model becomes:

$$\mathbf{Z} = \tau_L \mathbf{W} \quad (5.15)$$

where \mathbf{Z} is the same defined in Equation [5.5] and \mathbf{W} is the covariance matrix for the speckle, multiplied for the number of looks:

$$\mathbf{W} = L \cdot \frac{1}{L} \sum_{i=1}^L \mathbf{w}_i \mathbf{w}_i^H \quad (5.16)$$

that it is assumed complex Wishart distributed:

$$\mathbf{W} \sim \mathcal{W}_d^{\mathbb{C}}(L, \boldsymbol{\Sigma}_{\mathbf{w}}) \quad (5.17)$$

5.2 Model-based Decompositions with fourth-order statistics approach

Traditional decomposition are used to decompose the covariance or coherency matrix as a sum of covariance or coherency matrices corresponding to one of N scattering mechanism:

$$\langle [\mathbf{C}] \rangle = \sum_{i=1}^N P_i \mathbf{C}_i \quad \langle [\mathbf{T}] \rangle = \sum_{i=1}^N P_i \mathbf{T}_i \quad (5.18)$$

e.g.

$$\langle [\mathbf{T}] \rangle = P_s[\mathbf{T}_{surface}] + P_v[\mathbf{T}_{volume}] \quad (5.19)$$

In addition, each matrix is multiplied for the power P_i of a such scattering mechanism. This form of \mathbf{C} or \mathbf{T} can be reformulated in an equivalent form defining the power fractions as:

$$f_i = P_i/SPAN \quad P_i = f_i \cdot SPAN \quad (5.20)$$

where P_i is the power of the corresponding scattering mechanism. Considering the normalised covariance or coherency matrix in respect to the Span:

$$\langle [\tilde{\mathbf{C}}] \rangle = \langle [\mathbf{C}] \rangle / SPAN \quad \langle [\tilde{\mathbf{T}}] \rangle = \langle [\mathbf{T}] \rangle / SPAN \quad (5.21)$$

we can rewrite the decomposition as:

$$\langle [\mathbf{C}] \rangle = \sum_{i=1}^N f_i \mathbf{C}_i = \sum_{i=1}^N f_i \cdot SPAN \cdot \tilde{\mathbf{C}}_i = \sum_{i=1}^N P_i \tilde{\mathbf{C}}_i \quad (5.22)$$

$$\langle [\mathbf{T}] \rangle = \sum_{i=1}^N f_i \mathbf{T}_i = \sum_{i=1}^N f_i \cdot SPAN \cdot \tilde{\mathbf{T}}_i = \sum_{i=1}^N P_i \tilde{\mathbf{T}}_i \quad (5.23)$$

It is important to not confuse the normalised matrices $\tilde{\mathbf{T}}$ and $\tilde{\mathbf{C}}$ with the traditional matrices \mathbf{T} and \mathbf{C} , although, the formulation is completely equivalent. For example, if we consider the Sea-Ice Two-component decomposition, with the traditional form we have:

$$\langle [\mathbf{T}] \rangle = f_s[\mathbf{T}_{surface}] + f_v[\mathbf{T}_{volume}] \quad (5.24)$$

and with the new, but equivalent, formulation we have:

$$\langle [\mathbf{T}] \rangle = P_s[\tilde{\mathbf{T}}_{surface}] + P_v[\tilde{\mathbf{T}}_{volume}] \quad (5.25)$$

$$\langle [\mathbf{C}] \rangle = P_s[\tilde{\mathbf{C}}_{surface}] + P_v[\tilde{\mathbf{C}}_{volume}] \quad (5.26)$$

but using the Equation [5.20] we obtain:

$$\langle [\mathbf{C}] \rangle = f_s \cdot SPAN \cdot [\tilde{\mathbf{C}}_{surface}] + f_v \cdot SPAN \cdot [\tilde{\mathbf{C}}_{volume}] \quad (5.27)$$

$$\langle [\mathbf{T}] \rangle = f_s \cdot SPAN \cdot [\tilde{\mathbf{T}}_{surface}] + f_v \cdot SPAN \cdot [\tilde{\mathbf{T}}_{volume}]$$

In the same way proposed in [7], we can see the decomposition as mixing fractions leads to a statistical interpretation as a probabilistic mixture. If we report this approach to the scattering vector, we can write:

$$p_{\mathbf{k}}(\mathbf{k}) = \sum_{j=1}^N f_j p_j(\mathbf{k}) \quad (5.28)$$

or

$$p_{\mathbf{\Omega}}(\mathbf{\Omega}) = \sum_{j=1}^N f_j p_j(\mathbf{\Omega}) \quad (5.29)$$

Now, let us see the procedure to compute the fourth-order moments of the scattering vector. Using the Span normalised formulation we can write:

$$\begin{aligned} \langle [\mathbf{T}] \rangle &= \sum_{i=1}^N f_i \cdot SPAN \cdot \tilde{T}_i \\ \langle [\mathbf{C}] \rangle &= \sum_{i=1}^N f_i \cdot SPAN \cdot \tilde{C}_i \end{aligned} \quad (5.30)$$

Now we compute the expression of the second-order moments and the fourth-order moments. The second-order moment of k_i is furthermore given as:

$$E[|k_i|^2] = \sum_{j=1}^N f_j \int k_i k_i^H p_{k_{i,j}}(k_i) dk_i = \sum_{j=1}^N f_j E[|k_{i,j}|^2] = \sum_{j=1}^N f_j T_{ii,j}$$

The fourth-order moment of k_i is given as:

$$E[|k_i|^4] = \sum_{j=1}^N f_j \int |k_i|^4 p_{k_{i,j}}(k_i) dk_i = \sum_{j=1}^N f_j E[|k_{i,j}|^4] \quad (5.31)$$

In our model $E[|k_{i,j}|^4]$ is given as:

$$E[|k_{i,j}|^4] = \int_{(\tau_j)} \tau_j^2 p_{\tau_j}(\tau_j) \left(\int_{(k_i)} |k_i|^4 p_{k_{i,j}}(k_i) dk_i \right) d\tau_j = 2E[\tau_j^2] \tilde{T}_{ii,j}^2 \quad (5.32)$$

The multiplicative factor 2 is the kurtosis of \mathbf{w} . Indeed, recalling the skewness and kurtosis definitions for a zero-mean random variable X :

$$skewness \equiv \frac{E[X^3]}{\sigma^3} \quad (5.33)$$

$$kurtosis \equiv \frac{E[X^4]}{\sigma^4} \quad (5.34)$$

we have :

$$\begin{aligned} skewness &= 0 \\ kurtosis &= 3 \end{aligned} \quad (5.35)$$

if X is a Gaussian random variable or:

$$\begin{aligned} skewness &= 0 \\ kurtosis &= 2 \end{aligned} \quad (5.36)$$

if X is a complex Gaussian random variable. Inserted the Equation [5.32] into [5.31] we get the final expressions of the fourth-order moments of the scattering vectors:

$$E[|k_i|^4] = \sum_{j=1}^N f_j 2E[\tau^2] SPAN^2 \tilde{T}_{ii,j}^2 \quad (5.37)$$

$$E[|\Omega_i|^4] = \sum_{j=1}^N f_j 2E[\tau^2] SPAN^2 \tilde{C}_{ii,j}^2 \quad (5.38)$$

where $\tilde{T}_{ii,j}$ and $\tilde{C}_{ii,j}$ are the i^{th} diagonal elements of the j^{th} model matrix. The procedure to compute the fourth-order moment of the Lexicographic vector Ω_i is analogue.

5.2.1 Sea Ice Two-component Decomposition

Restarting from the Sea Ice-Two component decomposition, described in Section [4.3.3], now we can rewrite it using the new Span normalised formulation:

$$\langle [T] \rangle = f_s \cdot SPAN \cdot [\tilde{T}_s] + f_v \cdot SPAN \cdot [\tilde{T}_{volume}] \quad (5.39)$$

$$\tilde{T}_s = \frac{1}{(1 + |\beta|^2)} \begin{bmatrix} 1 & \beta \text{sinc}(2\delta) & 0 \\ \beta^* \text{sinc}(2\delta) & \frac{1}{2} |\beta|^2 (1 + \text{sinc}(4\delta)) & 0 \\ 0 & 0 & \frac{1}{2} |\beta|^2 (1 - \text{sinc}(4\delta)) \end{bmatrix} \quad (5.40)$$

$$\tilde{T}_v = \frac{1}{3 - \rho} \begin{bmatrix} (1 + \rho) & 0 & 0 \\ 0 & (1 - \rho) & 0 \\ 0 & 0 & (1 - \rho) \end{bmatrix} \quad (5.41)$$

The normalisation in respect to the total power entails that the Span is equals to one and f_v and f_s are between $[0, 1]$, so we can write:

$$f_s + f_v = 1 \quad (5.42)$$

Assuming the two scattering mechanisms are uncorrelated, the total normalised coherency \tilde{T} matrix is given by the sum of each covariance matrix and we can write the Sea Ice Two-Component decomposition as:

$$\tilde{T} = \begin{bmatrix} \tilde{T}_{11} & \tilde{T}_{12} & 0 \\ \tilde{T}_{21} & \tilde{T}_{22} & 0 \\ 0 & 0 & \tilde{T}_{33} \end{bmatrix} \quad (5.43)$$

where :

$$\tilde{T}_{11} = \frac{f_s \cdot SPAN}{(1 + |\beta|^2)} + f_v \cdot SPAN \cdot \frac{(1 + \rho)}{3 - \rho} \quad (5.44)$$

$$\tilde{T}_{22} = \frac{1}{2} f_s \cdot SPAN \cdot \frac{|\beta|^2 (1 + \text{sinc}(4\delta))}{(1 + |\beta|^2)} + f_v \cdot SPAN \cdot \frac{(1 - \rho)}{3 - \rho} \quad (5.45)$$

$$\tilde{T}_{33} = \frac{1}{2} f_s \cdot SPAN \cdot \frac{|\beta|^2 (1 - \text{sinc}(4\delta))}{(1 + |\beta|^2)} + f_v \cdot SPAN \cdot \frac{(1 - \rho)}{3 - \rho} \quad (5.46)$$

$$\tilde{T}_{12} = f_s \cdot SPAN \cdot \frac{\beta^* \text{sinc}(2\delta)}{(1 + |\beta|^2)} \quad (5.47)$$

The expressions of the fourth-order moments are given by:

$$\langle k_1 \rangle^4 = 2E[\tau^2] SPAN^2 \cdot \left(f_s \cdot \left[\frac{1}{(1 + |\beta|^2)} \right]^2 + f_v \cdot \left[\frac{(1 + \rho)}{3 - \rho} \right]^2 \right) \quad (5.48)$$

$$\langle k_2 \rangle^4 = 2E[\tau^2] SPAN^2 \cdot \left(f_s \cdot \left[\frac{|\beta|^2 (1 + \text{sinc}(4\delta))}{2(1 + |\beta|^2)} \right]^2 + f_v \cdot \left[\frac{(1 - \rho)}{3 - \rho} \right]^2 \right) \quad (5.49)$$

$$\langle k_3 \rangle^4 = 2E[\tau^2] SPAN^2 \cdot \left(f_s \cdot \left[\frac{|\beta|^2 (1 - \text{sinc}(4\delta))}{2(1 + |\beta|^2)} \right]^2 + f_v \cdot \left[\frac{(1 - \rho)}{3 - \rho} \right]^2 \right) \quad (5.50)$$

Using these three new equations and considering the Span equation we have 8 equations and 7 unknowns. In this way it is possible to find an algebraic solution without needing to fix any parameter or making some kind of prior assumptions. The unknowns for such a decomposition are:

$$f_s \quad f_v \quad \delta \quad \rho \quad Re\{\beta\} \quad Im\{\beta\} \quad E[\tau^2] \quad (5.51)$$

It is important to consider two different cases:

$$1) \text{Non-Textured Data} : E[\tau^2] = 1 \quad (5.52)$$

$$2) \text{Textured Data} : E[\tau^2] \neq 1$$

The second case, that considers the texture, is the more general case and we expect best result from it. It is important to remember that we do not know anything about the distribution of the texture and we assume no particular hypothesis about its distribution. The power of the texture is a new variable although we know its mean. From this parameter it is possible to see how much the texture distribution deviates from the Gaussian distribution. This part will be shown in Chapter 7. Appendix B gives the complete procedure in order to obtain the algebraic solution for the Non-Textured data case. To find an algebraic solution for the Textured data case is more complicated and may not even be possible. This could be a part of a future work.

5.2.2 Freeman and Durden Decomposition

Now, in order to conclude our work, we present an application of the higher-order statistics approach to the most traditional model-based decomposition: the Freeman and Durden decomposition. It is important to remember that such a decomposition requires some prior assumptions in order to find a unique solution. This problem will be avoided using the fourth-order equation, as we show now. Restarting from the Freeman and Durden decomposition, defined in Section [4.3.1], we rewrite it using the Span normalised formulation :

$$\langle [\mathbf{T}] \rangle = f_s \cdot SPAN \cdot [\tilde{\mathbf{T}}_{surface}] + f_v \cdot SPAN \cdot [\tilde{\mathbf{T}}_{volume}] + f_{db} \cdot SPAN \cdot [\tilde{\mathbf{T}}_{double-bounce}] \quad (5.53)$$

where:

$$\tilde{\mathbf{T}}_s = \frac{1}{(1 + |\beta|^2)} \begin{bmatrix} 1 & \beta^* & 0 \\ \beta & |\beta|^2 & 0 \\ 0 & 0 & 0 \end{bmatrix} \quad (5.54)$$

$$\tilde{\mathbf{T}}_v = \frac{1}{2} \begin{bmatrix} 1 & 0 & 0 \\ 0 & 1/2 & 0 \\ 0 & 0 & 1/2 \end{bmatrix} \quad (5.55)$$

$$\tilde{\mathbf{T}}_{db} = \frac{1}{(1 + |\alpha|^2)} \begin{bmatrix} |\alpha|^2 & \alpha & 0 \\ \alpha^* & 1 & 0 \\ 0 & 0 & 0 \end{bmatrix} \quad (5.56)$$

The normalisation in respect to the total power entails that the Span is equals to one and $[f_v, f_s, f_{db}]$ are between $[0, 1]$ so :

$$f_s + f_v + f_{db} = 1 \quad (5.57)$$

Assuming the three scattering mechanisms are uncorrelated, the total normalised coherency $\tilde{\mathbf{T}}$ matrix is given by the sum of each covariance matrix and we can redefine the Freeman and Durden decomposition as:

$$\tilde{\mathbf{T}} = \begin{bmatrix} \tilde{T}_{11} & \tilde{T}_{12} & 0 \\ \tilde{T}_{21} & \tilde{T}_{22} & 0 \\ 0 & 0 & \tilde{T}_{33} \end{bmatrix} \quad (5.58)$$

$$\tilde{T}_{11} = \frac{f_s \cdot SPAN}{(1 + |\beta|^2)} + f_{db} \cdot SPAN \cdot \frac{|\alpha|^2}{(1 + |\alpha|^2)} + f_v \cdot \frac{1}{2} \quad (5.59)$$

$$\tilde{T}_{22} = \frac{f_s \cdot SPAN \cdot |\beta|^2}{(1 + |\beta|^2)} + \frac{f_{db} \cdot SPAN}{(1 + |\alpha|^2)} + f_v \cdot \frac{1}{4} \quad (5.60)$$

$$\tilde{T}_{12} = f_s \cdot SPAN \cdot \frac{\beta^*}{(1 + |\beta|^2)} + f_{db} \cdot SPAN \cdot \frac{\alpha}{(1 + |\alpha|^2)} \quad (5.61)$$

$$\tilde{T}_{33} = f_v \cdot SPAN \cdot \frac{1}{4} \quad (5.62)$$

Now, we write the expression of the fourth-order components:

$$\langle \kappa_1 \rangle^4 = 2E[\tau^2] SPAN^2 \cdot \left(f_s \cdot \left[\frac{1}{(1 + |\beta|^2)} \right]^2 + f_{db} \cdot \left[\frac{|\alpha|^2}{(1 + |\alpha|^2)} \right]^2 + f_v \cdot \frac{1}{4} \right) \quad (5.63)$$

$$\langle \kappa_2 \rangle^4 = 2E[\tau^2] SPAN^2 \cdot \left(f_s \cdot \left[\frac{|\beta|^2}{(1 + |\beta|^2)} \right]^2 + f_{db} \cdot \left[\frac{1}{(1 + |\alpha|^2)} \right]^2 + f_v \cdot \frac{1}{16} \right) \quad (5.64)$$

$$\langle \kappa_3 \rangle^4 = 2E[\tau^2] SPAN^2 f_v \cdot \frac{1}{16} \quad (5.65)$$

Summarizing, the “new” decomposition has 8 equations and 8 unknowns:

$$f_s \quad f_v \quad f_{db} \quad Re\{\beta\} \quad Im\{\beta\} \quad Re\{\alpha\} \quad Im\{\alpha\} \quad E[\tau^2] \quad (5.66)$$

The traditional Freeman and Durden decomposition consider β is real, but it can be considered as complex, in more general case. We choose this last hypothesis.

5.2.3 Optimisation Algorithm

We have just seen that to use the new three fourth-order equations allows to have, at least, the same number of equations and unknowns. However, to find a close form solution is not always easy. For this reason, and to contrast the speckle, we choose to use an optimisation algorithm. This choice has also been done considering the speckle perspective. In fact, with the optimisation algorithm it is possible to consider the speckle that it is not possible with the algebraic or analytic solution. In the Results Chapter we will show the speckle robustness of the chosen optimisation strategy. The software used to realize the simulation is Matlab. We have used two types of optimisation algorithm: a genetic algorithm and a nonlinear algorithm. The Matlab functions used are *Particle Swarm* and *Fmincon*. Particle Swarm is a particular genetic algorithm that simulates the behavior of the nature, in particular that of the insects. Fmincon is a typical non-linear solver. Particle swarm, being a genetic algorithm, improves its accuracy with increasing the computation time. Fmincon, instead, shows more speed, precision and speckle robustness. For these last reasons we have chosen to show the results obtained using Fmincon. In order to implement the optimisation algorithm, we have defined the cost function as the sum of each equation constituting the coherency matrix \mathbf{T} as:

$$J(x) = (x_1)^2 + (x_2)^2 + (x_3)^2 + (x_4)^2 + (x_5)^2 + (x_6)^2 + (x_7)^2 \quad (5.67)$$

where:

$$x_1 = \tilde{T}_{11} - \tilde{T}_{11measured}; \quad x_2 = \tilde{T}_{22} - \tilde{T}_{22measured}; \quad (5.68)$$

$$x_3 = \tilde{T}_{33} - \tilde{T}_{33measured}; \quad x_4 = \left| \tilde{T}_{12} \right| - \left| \tilde{T}_{12measured} \right| \quad (5.69)$$

$$x_5 = \langle k_1 \rangle^4 - \langle k_{1measured} \rangle^4; \quad x_6 = \langle k_2 \rangle^4 - \langle k_{2measured} \rangle^4 \quad (5.70)$$

$$x_7 = \langle k_3 \rangle^4 - \langle k_{3measured} \rangle^4 \quad (5.71)$$

and the $\tilde{\mathbf{T}}$ is derived from the model given the current or testing parameters.

5.2.3.1 Relative weights

In order to improve the quality of the optimisation, we choose to utilize a weighted cost function. Our goal is to balance the error introduced by each equation. In particular, we would like to model the error introduced by each equation as a random variable with zero mean and unitary variance. The starting point has been to introduce the relative weights considering that the Coherency matrix \mathbf{T} typically shows higher values for T_{11} compared than T_{33} .

$$J(x) = \alpha_1(x_1)^2 + \alpha_2(x_2)^2 + \alpha_3(x_3)^2 + \alpha_4(x_4)^2 + \alpha_5(x_5)^2 + \alpha_6(x_6)^2 + \alpha_7(x_7)^2 \quad (5.72)$$

where:

$$\alpha_1 = 1/T_{11measured}^2; \alpha_2 = 1/T_{22measured}^2 \quad \alpha_3 = 1/T_{33measured}^2 \quad (5.73)$$

$$\alpha_4 = 1/\sqrt{T_{11measured} \cdot T_{22measured}} \quad (5.74)$$

$$\alpha_5 = 1/\left\{ \langle k_{1measured} \rangle^4 \right\}^2 \quad (5.75)$$

$$\alpha_6 = 1/\left\{ \langle k_{2measured} \rangle^4 \right\}^2 \quad (5.76)$$

$$\alpha_7 = 1/\left\{ \langle k_{3measured} \rangle^4 \right\}^2 \quad (5.77)$$

The relative weights choice has been validated from the results. However, the challenging part is to model the weight for T_{12} . It is known that T_{12} is not real but complex. We have to say we used an optimisation algorithm for real value. For this reason we considered the absolute value of T_{12} and so we can use as its weight the root square of the correlation between T_{11} and T_{22} . It is important to reiterate that this is only a first approach but we think a more analyzed study about the theoretical variance of each equation, can allow to get better results.

Chapter 6

Data Material Description

Before to show the results, we think it is important to recall the information about the Polarimetric Data used and the metric used to evaluate the performance of the studied decomposition theorems.

6.1 SLC and MLC Data

PolSAR data are usually express in SLC and MLC format. SLC is the acronyms of Single Look Complex. SLC data represents the vectorized scattering matrix defined in Equation [2.23]. In this way, we can see SLC data as a D -dimensional array :

$$SLC : [D, N_x, N_y] \tag{6.1}$$

where D is equal to 3 in monostatic case or equals to 4 in the bistatic scattering case and N_x and N_y represent the x and y coordinates, respectively. Let us see in the following figure the SLC data format:

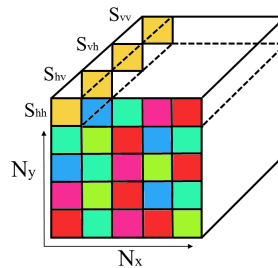


Figure 6.1: SLC Data Format.

Notice that for each pixel is characterized by a vectorized form of the 2×2 scattering $[S]$ matrix. MLC is the acronyms of Multi Look Complex and is obtained trough the multilooking process defined in Equations [2.54] and [2.55].

If we consider the $\boldsymbol{\kappa}$ vector defined in Equations [2.26] and [2.40] for each pixel we obtain the Coherency \mathbf{T} matrix, otherwise the covariance \mathbf{C} matrix if we consider $\boldsymbol{\Omega}$ vector defined in Equations [2.27] and [2.41].

$$MLC : [D, D, N_x/W_x, N_y/W_y] \quad (6.2)$$

where W_x and W_y are the x and y dimensions of the particular chosen window to realize the spatial average. We have seen that the Multilooking process reduces the spatial resolution but is very useful to reduce the image size and so the image processing time. It is possible to notice that the L -parameter defined in Equations [2.54] or [2.55] corresponds to the window area, given by $[W_x \cdot W_y]$. Being the elements of the complex scattering matrix, it is obvious that SLC and MLC data are complex valued.

6.2 Test Images

The most part of our work has been focused on the Sea Ice Two-Component decomposition. The main problem for the Sea Ice scenes is often not having ground truth measurements. In this way, it is difficult to evaluate if a decomposition is reliable or not. In order to have a fast and sure way to compare the quality of such a decomposition we used test images. Exactly as shown in [7] we used a Coherency matrix test-pattern, with 6x6 blocks, using different parameter values taken from real values for sea ice and ocean. Data have been generated using an hard probabilistic mixture model for the scattering vector $\boldsymbol{\kappa}$:

$$p_k(\boldsymbol{\kappa}) = \sum_{j=1}^{N_c} f_j \mathcal{N}_d^{\mathbb{C}}(0, T_j) \quad (6.3)$$

with the multivariate complex Gaussian data model. We have used a large window to realize the multilooking, 50×50 , in order to suppress the speckle. Suddenly we will refer to Equation [6.3] as Gaussian data. Furthermore, we will also generate the same data using an hard probabilistic mixture model for k but with the multivariate complex K-Distribution data model :

$$p_k(\boldsymbol{\kappa}) = \sum_{j=1}^{N_c} f_j \mathcal{K}_d^{\mathbb{C}}(0, T_j) \quad (6.4)$$

It is important to recall that the K-distribution for the scattering vector originates from the assumption of a texture τ Gamma distributed:

$$p_\tau(\tau) = \frac{(\alpha\tau)^\alpha}{\tau\Gamma(\alpha)} \exp(-\alpha\tau) \quad (6.5)$$

In our implementation we used $\alpha = 10$. In the following figure are shown the test-images so built:

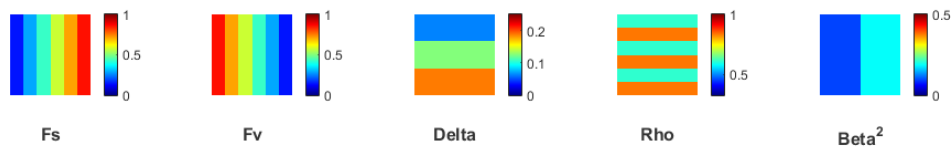


Figure 6.2: Test images used to simulate Sea Ice Two-Component decomposition parameters.

The size of each test-image is $[24 \times 24]$ and the same colormap has been used. The Matlab colormap used was “Jet”. The small size of the images allowed for fast implementations. This is particularly important if we consider using optimisation algorithms. It is also important to recall that δ is a surface parameter and ρ is a volume parameter. This means that it is only important to have well-defined δ when f_s shows high values. The same reasoning is valid for ρ in respect to f_v . Notice that f_s and f_v are complementary, being only two scattering components. It is important to remember that we used the test pattern simulation only for the Sea Ice Two-Component decomposition.

6.3 Real Images

The real images used in our work are two. The first image is the sea ice scene from the Fram Strait, Greenland. The figure [6.3] shows the Pauli decomposition of such an image. It is possible to notice a section black on the left that is open water. The central part of the image, in light purple, is a smooth first-year ice zone. In top-right corner, instead, there are ridges and very deformed ice. Thickness measurements, obtained with a helicopter-borne laser altimeter, confirms the hypothesis of very smooth ice in the central part of the image. The second image is the well known San Francisco Bay, California. This image is commonly used in SAR image processing because provides a perfect scenario for radar polarimetry. Indeed, it provides sea, mountains and urban areas. This image is not appropriate for the Sea Ice Two-component decomposition but it is useful to compare the results for Freeman and Durden decomposition using second order and fourth-order statistics.

6.4 Accuracy

To measure the quality of the reconstruction images we have used the following metrics. The Mean Square Error , defined as:

$$MSE = \frac{1}{mn} \sum_{i=0}^{m-1} \sum_{j=0}^{n-1} [f(i, j) - \tilde{f}(i, j)]^2 \quad (6.6)$$

measures the average of the squares of the errors, defined as the difference between the observed \tilde{f} and the model value f [20][16]. Since we use a normalised

cost function in our optimisation problem, we consider it important to use a normalised version of the metric. We call this quantity Relative Mean Square Error, $rMSE$, which is given by:

$$rMSE = \frac{1}{mn} \sum_{i=0}^{m-1} \sum_{j=0}^{n-1} \left[\frac{f(i, j) - \tilde{f}(i, j)}{f(i, j)} \right]^2 \quad (6.7)$$

The Root Mean Square Error is typically used, defined as the root square of the MSE:

$$RrMSE = \sqrt{rMSE} \quad (6.8)$$

In the result chapter, in order to better interpret the results, we will use the relative root mean square error expressed in percentage:

$$RrMSE\% = RrMSE \cdot 100 \quad (6.9)$$

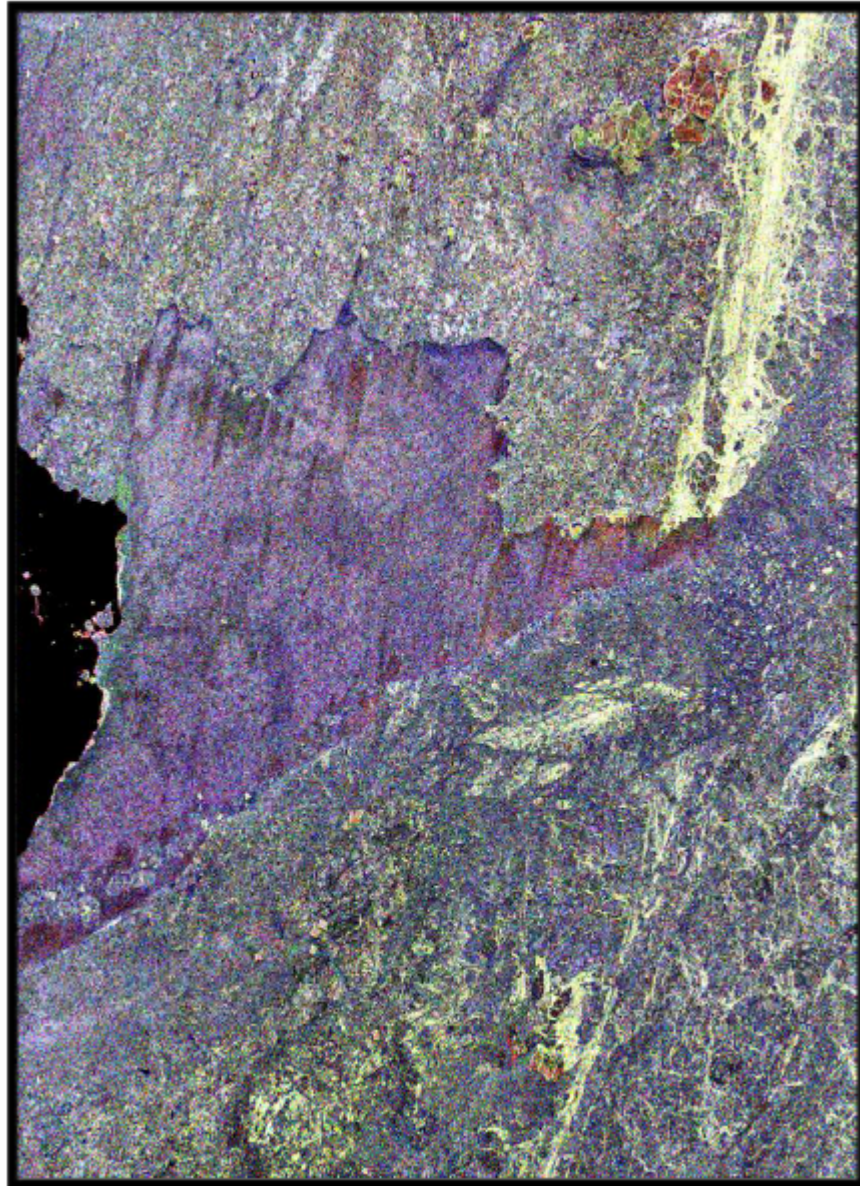


Figure 6.3: Pauli decomposition of sea ice scene from Fram Strait, Greenland. The image has been processed with the PolSARPro software [29].

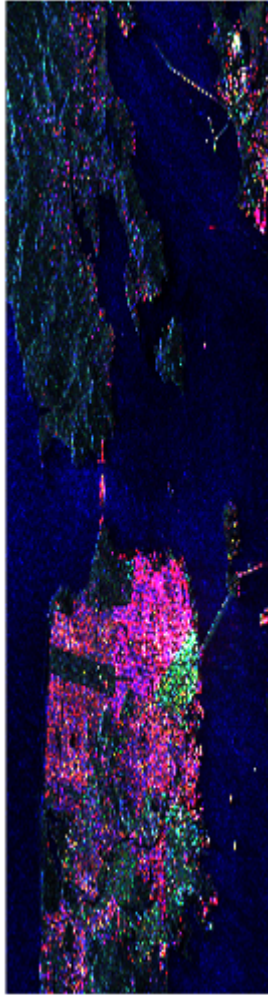


Figure 6.4: Pauli decomposition of San Francisco Bay, California.

Chapter 7

Results

In this final chapter we will show the results of the discussed decompositions. We start from the traditional model-based decompositions and we will conclude with the new higher-order model based decomposition.

7.1 Traditional Model-Based Decompositions

Before showing the found results using the higher-order statistics, we will see the traditional model-based decompositions applied to the work images in order to have a possible visual comparison. In particular, it will be possible to see how difficult it is to analyze the sea ice scenes with the traditional methods and so the possible usefulness of the proposed specific model-based decomposition for the sea ice. Figure [7.1] shows the surface, volume and double-bounce Span normalised powers obtained with the NNED. Figure [7.2] shows the same components but using the Freeman and Durden decomposition. The same Matlab colormap and the same number of looks, 8, have been used. As expected, NNED and Freeman and Durden decomposition give similar results. Both of them, show high surface scattering and very low double-bounce scattering. In particular, we can see the big difference among the double-bounce power and the other two remaining powers. This confirms the hypothesis made in [9] about the possible negligence of the double-bounce scattering in sea ice scenes.

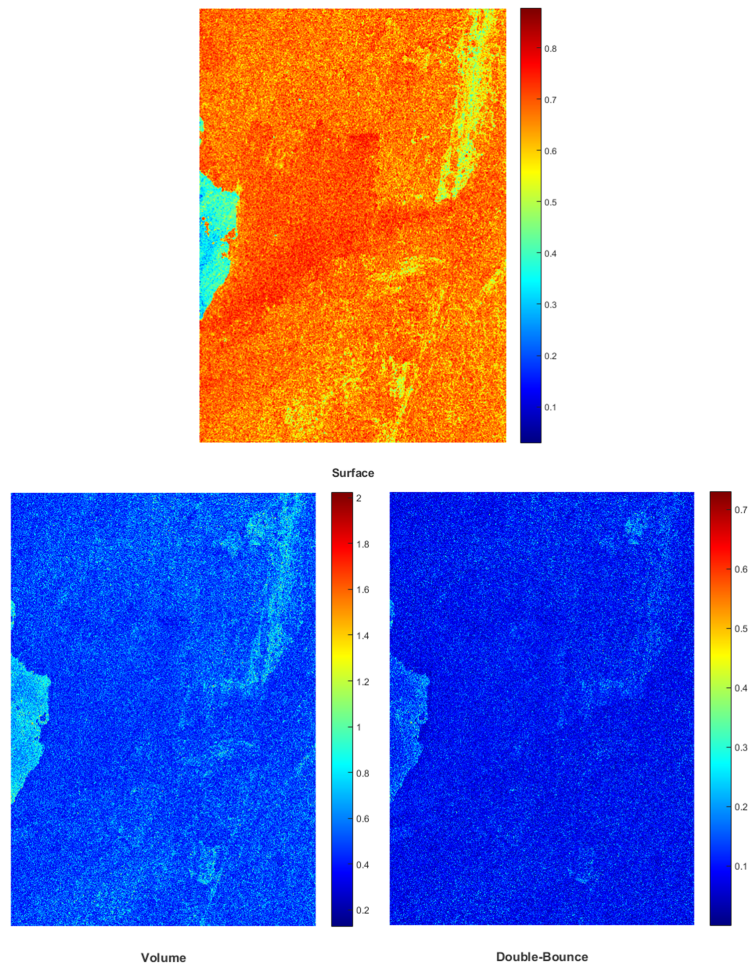


Figure 7.1: Non Negative Eigenvalue decomposition of sea ice scene from Fram Strait, Greenland. Span normalised powers.

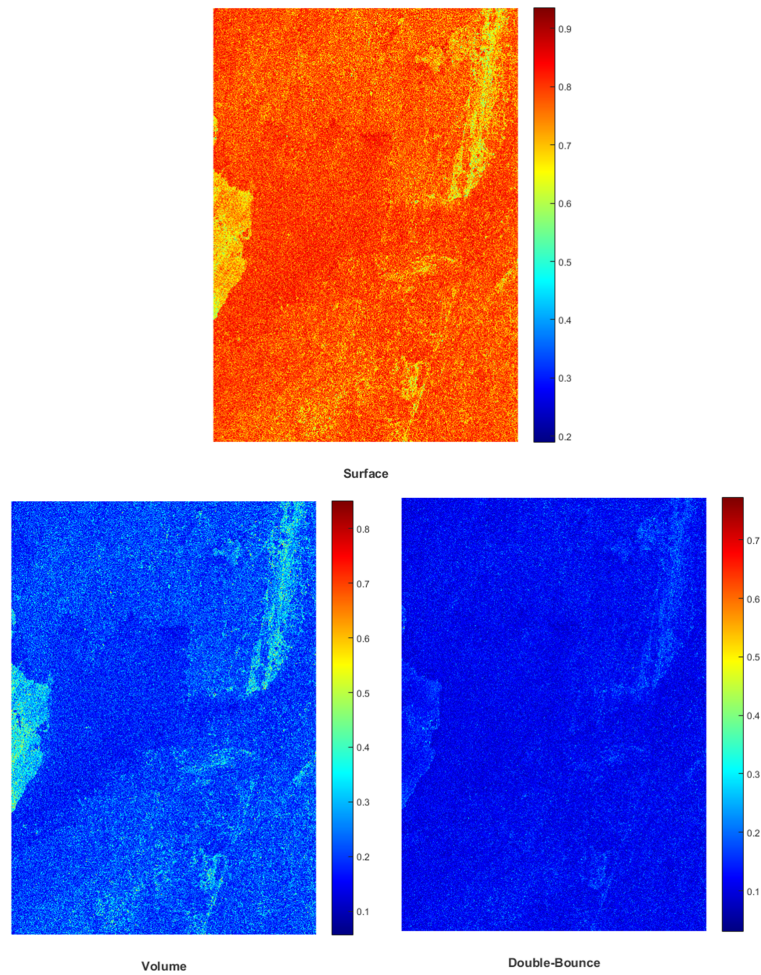


Figure 7.2: Traditional Freeman and Durden decomposition of sea ice scene from Fram Strait, Greenland. Span normalised powers.

7.2 Model-Based Decomposition using fourth-order statistics

Let us see the main results of our work: higher-order statistics applied to model-based decompositions. We will show the results for the following decompositions: Sea Ice Two-Component and Freeman and Durden.

7.2.1 Sea Ice Two-component Decomposition

As introduced in Chapter [6], the Sea Ice Two-Component decomposition has been the most analyzed decomposition in our work. We will show separately the results of such a decomposition for test patterns and real images, respectively.

7.2.1.1 Test Pattern

As described in Section [6.2], we used two models to build test patterns: Gaussian model and Non Gaussian model.

Gaussian Data

Second Order Moments

The test patterns are useful to show the improvement caused by the use of the fourth-order moments. For this reason it is important to start showing the obtained results using only the second-order information. Table [7.1] shows in first column the test patterns and in the second column the estimated values. Where it is possible to notice that using only second-order information does not cause satisfactory results. To have a better measure than a visual interpretation we show the RrMSE computed for each test pattern. In particular, in order to simplify the interpretation, we showed the RrMSE for each block of each test pattern. For example, test pattern of $|\beta|^2$ is constituted by two values, and we will show the RrMSE corresponding to each value. In this way, it is easy to understand how far, in percentage, the real value is from the estimated value and to have a quality measure of the considered decomposition. In addition, we will average these values and we will propose, in the last column the mean value of the RrMSE for each test pattern, RrMSE%.

Fourth-Order Moments Non-Textured model- Algebraic Solution

Let us start the fourth-order statistics analysis with the results obtained for the Non-Textured model using the algebraic solution, shown in Table [7.2]. It is important to remind that the Non-Textured case means:

$$E [\tau^2] = 1 \quad (7.1)$$

It is already possible to see the strong improvement introduced by the fourth-order statistics. The only exception is about $|\beta|^2$. Let us see our hypothesis about the odd RrMSE values of $|\beta|^2$. The algebraic solution, unlike the optimisation algorithm strategy, does not contrast the speckle. In this way it is possible all the noise converges in this parameter. We think this situation can be improved realizing a perfect balance of the errors introduced by each equation. It is also true that only the left side of $|\beta|^2$ shows a noisy behavior.

Fourth Order Moments Non-Textured model

Table [7.3] shows the results for the Sea Ice Two-Component decomposition

using the fourth-order statistics in the case without texture, and using the optimisation strategy defined in Section [5.5]. As confirm of the previous hypothesis about $|\beta|^2$, the optimisation strategy shows a more reliable value RrMSE. We repeat that a perfect error balance introduced by the optimisation algorithm would allow a better reconstruction.

Fourth-Order Moments Textured model

Table [7.4] shows the results for the Textured model. The results are similar to the Non-Textured model. It is also important to remind that we are considering Gaussian Data. Typically, PolSAR data are not Gaussian and so we expect better result for the Textured model but only for the Non Gaussian Data, as shown in the following part.

Summary

In order to show more clearly the improvement introduced by the fourth-order statistics we show in Tables [7.5] and [7.6] all the results obtained and their differences in terms of RrMSE%. The underscored values represent the best improvement between models for each parameter. From such a table we can conclude that for Gaussian data, the fourth-order moments without considering the texture allows a better parameters estimation.

	Test Pattern	Estimated	$\overline{RrMSE\%}$
RrMSE for each block			
f_s			19.57%
	[1] [2] [3] [4] [5] [6] 0.5488 0.2306 0.1626 0.1122 0.0760 0.0441		
f_v			15.16%
	[1] [2] [3] [4] [5] [6] 0.0915 0.0922 0.1220 0.1496 0.1900 0.2646		
δ			37.93%
	[1] [2] [3] 0.4912 0.3786 0.2682		
ρ			13.12%
	[1] [2] ... 0.1365 0.1260		
$ \beta ^2$			36.62%
	[1] [2] 0.4354 0.2970		

Table 7.1: Sea Ice Two-Component decomposition using second-order statistics and the optimisation strategy, for Gaussian data.

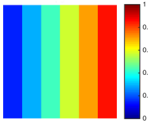
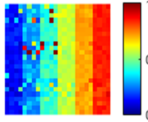
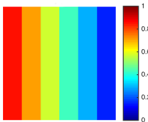
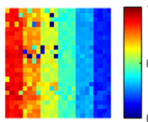
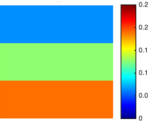
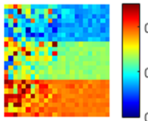
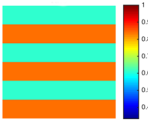
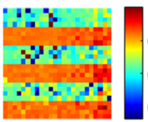
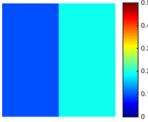
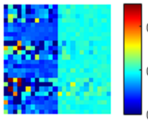
	Test Pattern	Estimated	$\overline{RrMSE\%}$
RrMSE for each block			
f_s			14.21%
	[1] [2] [3] [4] [5] [6]		
	0.1711 0.3138 0.3264 0.0181 0.0123 0.0106		
f_v			8.62%
	[1] [2] [3] [4] [5] [6]		
	0.0285 0.1255 0.2448 0.0242 0.0309 0.0106		
δ			18.11%
	[1] [2] [3]		
	0.3452 0.1362 0.0619		
ρ			5.55%
	[1] [2] ...		
	0.0988 0.0123		
$ \beta ^2$			108.36%
	[1] [2]		
	2.09 0.0772		

Table 7.2: Sea Ice Two-Component decomposition using fourth-order statistics for the Non-Textured model computed with the algebraic solution and Gaussian data.

	Test Pattern	Estimated	$\overline{RrMSE\%}$
RrMSE for each block			
f_s			6.78%
	<div style="display: flex; justify-content: space-around;"> <div style="text-align: center;">[1] 0.1637</div> <div style="text-align: center;">[2] 0.0799</div> <div style="text-align: center;">[3] 0.0532</div> <div style="text-align: center;">[4] 0.0383</div> <div style="text-align: center;">[5] 0.0362</div> <div style="text-align: center;">[6] 0.0355</div> </div>		
f_v			7.286%
	<div style="display: flex; justify-content: space-around;"> <div style="text-align: center;">[1] 0.0273</div> <div style="text-align: center;">[2] 0.0320</div> <div style="text-align: center;">[3] 0.0399</div> <div style="text-align: center;">[4] 0.0510</div> <div style="text-align: center;">[5] 0.0906</div> <div style="text-align: center;">[6] 0.1964</div> </div>		
δ			19.083%
	<div style="display: flex; justify-content: space-around;"> <div style="text-align: center;">[1] 0.3520</div> <div style="text-align: center;">[2] 0.1424</div> <div style="text-align: center;">[3] 0.0781</div> </div>		
ρ			3.91%
	<div style="display: flex; justify-content: space-around;"> <div style="text-align: center;">[1] 0.0452</div> <div style="text-align: center;">[2] 0.0330</div> <div style="text-align: center;">...</div> </div>		
$ \beta ^2$			18.00%
	<div style="display: flex; justify-content: space-around;"> <div style="text-align: center;">[1] 0.1731</div> <div style="text-align: center;">[2] 0.1870</div> </div>		

Table 7.3: Sea Ice Two-Component decomposition using fourth-order statistics and the optimisation strategy, for the Non-Textured model and Gaussian data.

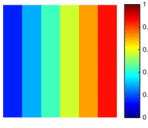
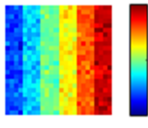
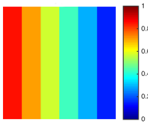
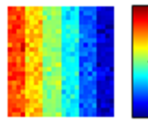
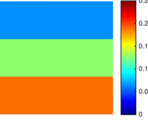
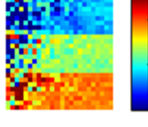
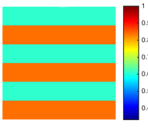
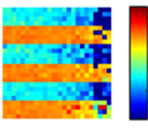
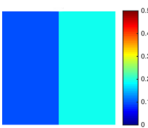
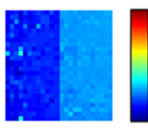
	Test Pattern	Estimated	$\overline{RrMSE\%}$				
RrMSE for each block							
f_s			7.29%				
	[1] 0.1886	[2] 0.0932	[3] 0.0645	[4] 0.0484	[5] 0.0480	[6] 0.0426	
f_v			9.29%				
	[1] 0.0315	[2] 0.0373	[3] 0.0484	[4] 0.0646	[5] 0.1200	[6] 0.2555	
δ			20.3%				
	[1] 0.3703	[2] 0.1559	[3] 0.0829				
ρ			6.82%				
	[1] 0.0864	[2] 0.0500	...				
$ \beta ^2$			18.73%				
	[1] 0.1887	[2] 0.1859					

Table 7.4: Sea Ice Two-Component decomposition using fourth-order statistics and the optimisation strategy, for Textured model and Gaussian data.

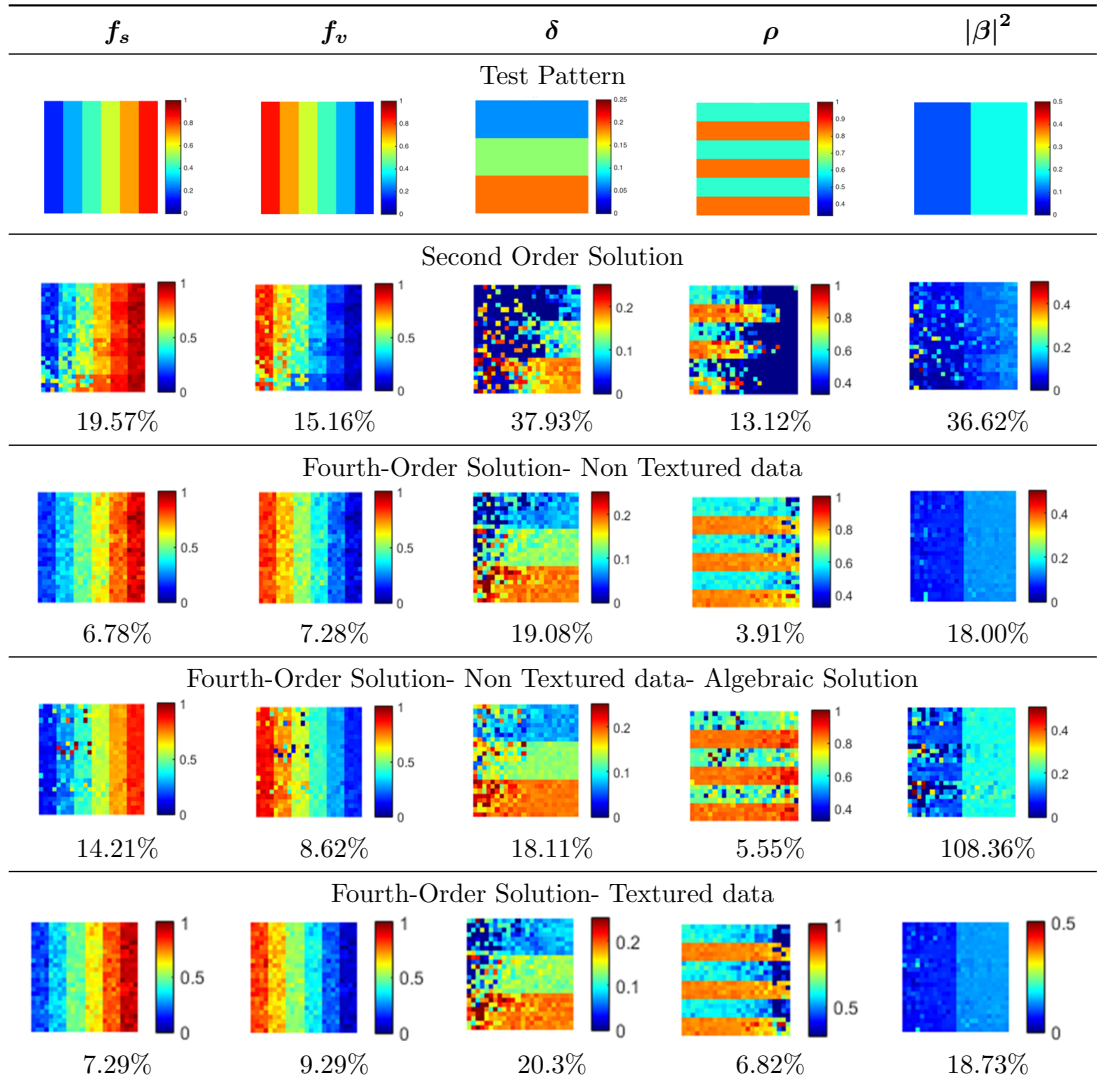


Table 7.5: Summary results for the various Sea Ice Two-Component decomposition with Gaussian data.

Results comparison	$\Delta RrMSEe\%$					
<i>2nd – Order vs 4th – Order NoTexture</i>	f_s	f_v	δ	ρ	$ \beta ^2$	[%]
	+12.79	+7.88	+18.85	+9.21	+18.62	
<i>2nd – Order vs 4th – Order No – Texture Algebraic – Solution</i>	f_s	f_v	δ	ρ	$ \beta ^2$	[%]
	+5.36	+6.54	+19.82	+7.57	-71.74	
<i>2nd – Order vs 4th – Order Textured</i>	f_s	f_v	δ	ρ	$ \beta ^2$	[%]
	+12.28	+5.87	+17.63	+6.3	+17.89	
<i>4th – Order No – Texture vs 4th – Order No – Texture Algebraic – Solution</i>	f_s	f_v	δ	ρ	$ \beta ^2$	[%]
	+7.43	+1.34	-0.97	+1.64	-90.36	
<i>4th – Order No – Texture vs 4th – Order Textured</i>	f_s	f_v	δ	ρ	$ \beta ^2$	[%]
	+0.51	+2.01	+1.22	+2.91	+0.73	
<i>4th – Order No – Texture Algebraic – Solution vs 4th – Order Textured</i>	f_s	f_v	δ	ρ	$ \beta ^2$	[%]
	-6.92	+0.67	+2.19	+1.27	-89.63	

Table 7.6: Second-Order and High-order methods comparison, with Gaussian data.

Non Gaussian Data

As described in Section [6.2], we used $\alpha = 10$ in order to build the data with the K-distribution model for the scattering vector \mathbf{k} .

Fourth-Order Moments Non-Textured model

As expected the results with the Non-Textured model are not satisfying. Only

$|\beta|^2$, δ , and ρ show a soft improvement over the second-order case, as shown in Table [7.7].

Fourth-Order Moments Textured model

This case shows a more reliability than the Non-Textured model, as it is possible to see in Table [7.8]. In particular, considering that the PolSAR data are non Gaussian, this “road” could be very interesting. We choose the K-distribution but clearly it is not the unique possibility. To analyze the study of the Non-Gaussian distribution of the product model could be an interesting future work.

Summary for test pattern simulations:

Let us try to resume the obtained results for the test pattern simulations. All the fourth-order moments cases show a strong improvement in respect to the second-order case, both for Gaussian and Non Gaussian data. In particular, the best results for Gaussian data, is shown by the fourth-order statistics case not considering the texture, as it is possible to see comparing Table [7.1] and Table [7.3]. Another important result is observable comparing Table [7.2] and Table [7.3], the Non-Textured model with the algebraic solution and the Non-Textured model with the optimisation algorithm, respectively. This comparison allows us to see smoother images when we use the optimisation algorithm. Therefore, we can affirm that using the optimisation algorithm allows to reduce the speckle in a larger manner than the algebraic solution. For non Gaussian data, the best results are shown for the Non-Textured model, as expected. However, these results do not show a better behavior than the best results obtained for the Gaussian data. Before to conclude we must reaffirm that we have not realize a perfect balance of the error equations but nevertheless it is already possible to affirm the usefulness of the fourth-order moments in the model-based decompositions.

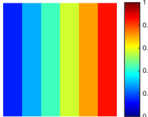
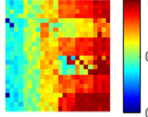
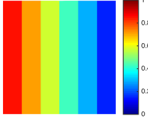
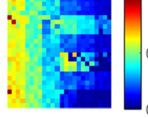
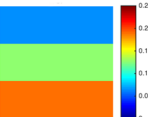
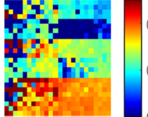
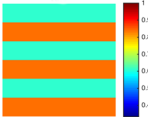
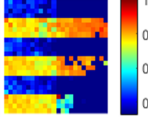
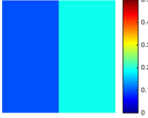
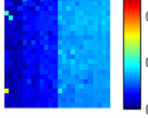
	Test Pattern	Estimated	$\overline{RrMSE\%}$
RrMSE for each block			
f_s			26.12%
	[1] [2] [3] [4] [5] [6]		
	0.7138 0.3451 0.2250 0.1517 0.0882 0.0434		
f_v			18.48%
	[1] [2] [3] [4] [5] [6]		
	0.1190 0.1380 0.1688 0.2022 0.2204 0.2603		
δ			23.46%
	[1] [2] [3]		
	0.5393 0.0225 0.1420		
ρ			10.68%
	[1] [2] ...		
	0.1653 0.0484		
$ \beta ^2$			28.13%
	[1] [2]		
	0.3794 0.1832		

Table 7.7: Sea Ice Two-Component decomposition using fourth-order moments and the optimisation algorithm for Non-Textured model and Non Gaussian data.

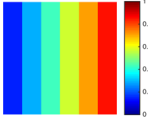
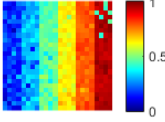
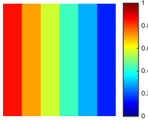
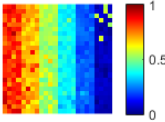
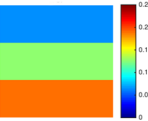
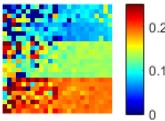
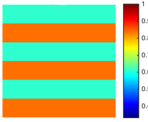
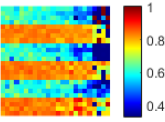
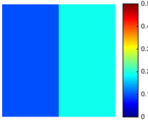
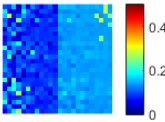
	Test Pattern	Estimated	$\overline{RrMSE\%}$
RrMSE for each block			
f_s			7.64%
	[1] [2] [3] [4] [5] [6]		
	0.1687 0.0775 0.0523 0.0480 0.0440 0.0681		
f_v			11.34%
	[1] [2] [3] [4] [5] [6]		
	0.0281 0.0310 0.0392 0.0639 0.1100 0.4085		
δ			25.23%
	[1] [2] [3]		
	0.4486 0.1944 0.1141		
ρ			7.15%
	[1] [2] ...		
	0.0925 0.0506		
$ \beta ^2$			24.79%
	[1] [2]		
	0.3111 0.1848		

Table 7.8: Sea Ice Two-Component decomposition using fourth-order moments and the optimisation algorithm for Textured model and Non Gaussian data.

7.2.1.2 Real Images

Let us see now the more interesting real sea ice image of the Fram strait, Greenland. The next images have been obtained with a multilooking process with a $[100 \times 100]$ window in order to suppress the speckle.

Second Order Moments

Figure [7.3] shows the retrieved parameters using the second-order moments. We used the optimisation algorithm and not fixing the delta parameter. The results seems very different from the traditional decompositions. High volume over all the scene can be noticed, as not expected from sea ice. The uncertainty about the ground truth cannot allow to be completely sure about the interpretation. We think the non perfect balance of the errors may mislead to a not proper interpretation. Nevertheless, analyzing the results we can see the correct behavior for the open water, high surface and low volume as expected. This is an indication of a possibility to have good interpretations of the scene. The δ parameter, the roughness measure, shows higher values for the open water than the smooth area. We think this is not perfectly correct, but we must remember that δ is the noisiest parameter as seen in the test pattern results. The ρ parameter is the most difficult parameter to interpret. If we interpret what the image of ρ shows, we can see the highest values around the smooth ice zone. Remembering that ρ is the shape parameter and high values of ρ mean a spherical shape of the scatterers, we can try to interpret the smooth zone as multiyear ice zone. It is important to repeat that the non perfect balance error equations could influence all the parameters value, as shown by the high volume over all the scene. The $|\beta|^2$ parameter shows a non perfect behavior from what expected. $|\beta|^2$ is connected to the dielectric constant, and so we expect high $|\beta|^2$ values for open water that is characterized by a higher dielectric constant than sea ice. It is important to remind that the second-order moments case is the more noisy case as seen for the test patterns in Table [7.1].

Fourth-Order Moments Non-Textured model - Algebraic Solution

Let us see now the results obtained with the algebraic solution in Figure [7.4]. The results are generally similar to those obtained with the second-order moments. The only differences are in $|\beta|^2$ and δ . The δ parameter is very noisy and it is impossible to interpret it. $|\beta|^2$ is practically constant and although a visible difference between sea ice and water exists. To be honest, it is important to remember that the algebraic does not consider the speckle. In addition, we included the the imaginary part of β , that is connected to the imaginary part of the dielectric constant. The high values of the imaginary part of β are in correspondence to the sea water, as expected. After a general interpretation of all the parameters we can affirm the poor reliability of the algebraic solution. Although the algebraic solution shows strong mathematics characteristics, it does not show the same strength for the real images.

Fourth-Order Moments Non-Textured model

In Figure [7.5] are shown the retrieved parameters considering the Non-Textured model. The general behavior seems to be better than the previous cases. However, it is possible to see clearly the smooth ice zone that was not possible to see with the second-order moments. In addition, it is possible to observe a more general definition of the details, in particular for the ridges and deformed ice.

δ has the same problem described for the previous cases. The $|\beta|^2$ parameter shows a better behavior in respect the second-order moments but it is not reliable yet.

Fourth Order Moments Textured model

We conclude the Sea Ice Two-Component decomposition with the Textured model, as shown in Figure [7.6]. The results are very generally similar to the Non-Textured case but they seems to be the best obtained results. The image definition is the highest of all the previous seen cases and in addition it is possible to observe a correct behavior of $|\beta|^2$. Furthermore, this model allows to retrieve the texture that shows a correct behavior, as we will describe in the next paragraph. Considering the Non-Gaussianity of PolSAR data we believe this case is the more reliable between those just seen.

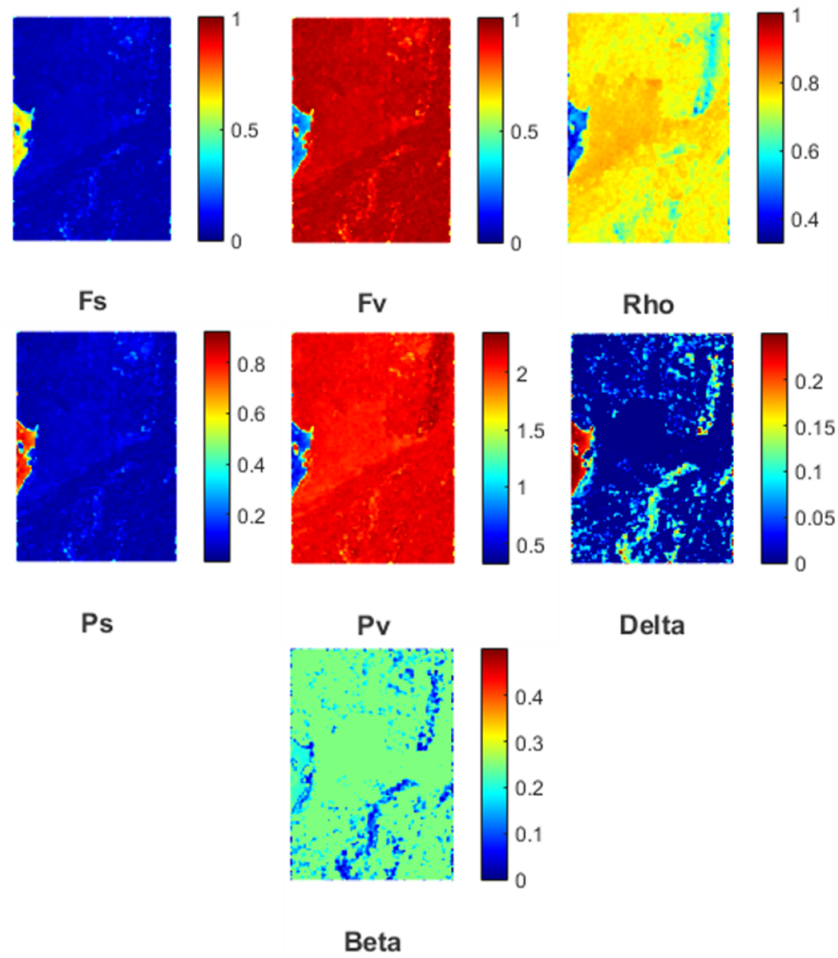


Figure 7.3: Sea Ice Two-Component decomposition using second-order statistics and the optimisation strategy.

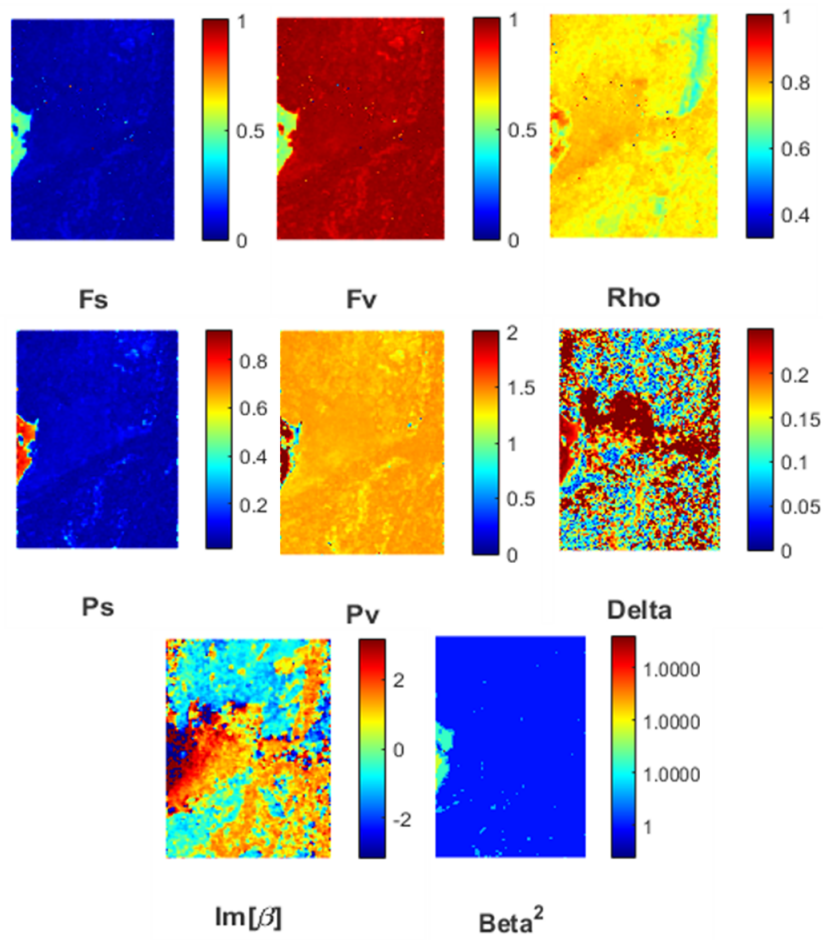


Figure 7.4: Sea Ice Two-Component decomposition using fourth-order statistics with the algebraic solution, for Non-Textured model.

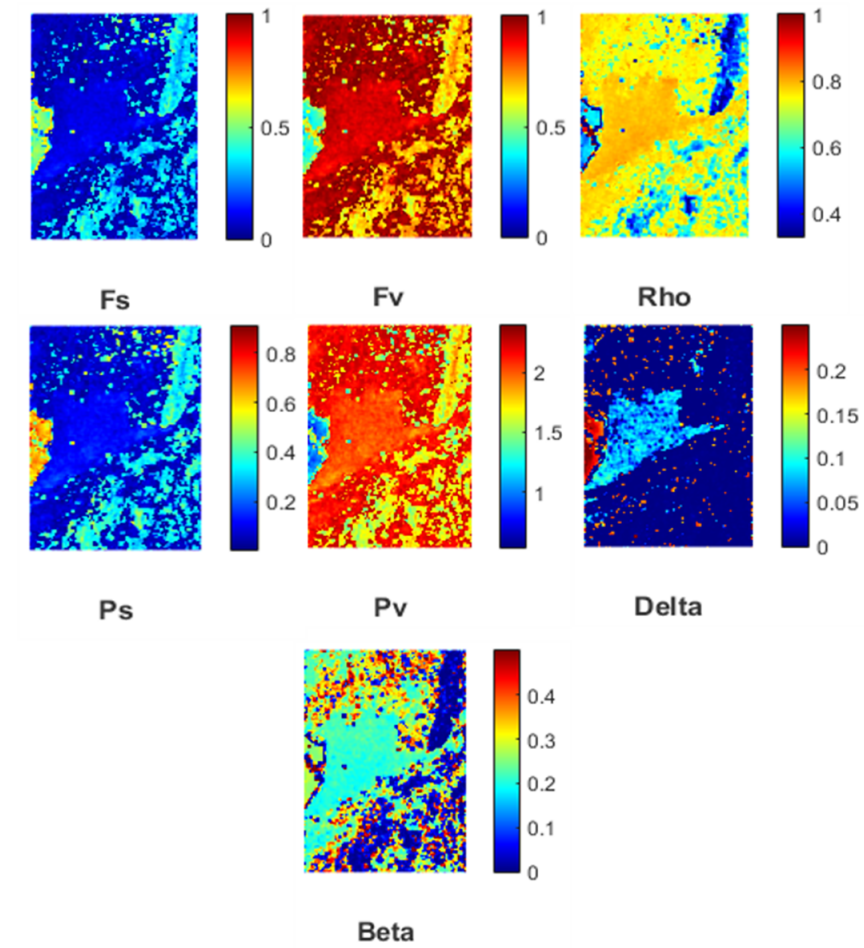


Figure 7.5: Sea Ice Two-Component decomposition using fourth-order statistics and the optimisation strategy, for Non-Textured model.

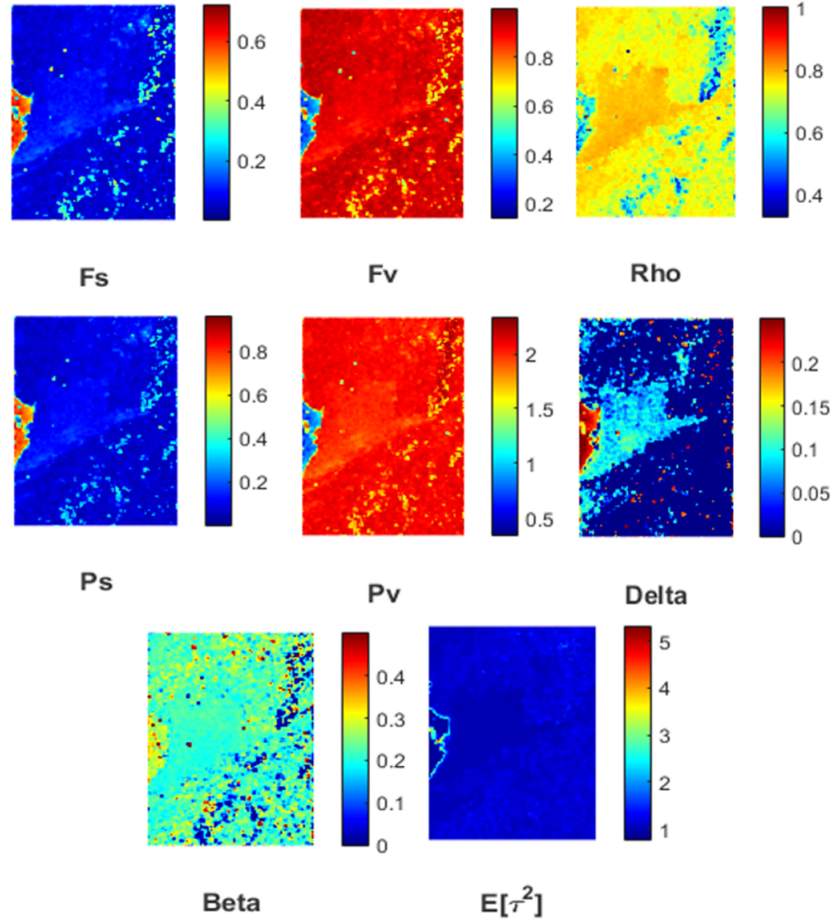


Figure 7.6: Sea Ice Two-Component decomposition using fourth-order statistics and the optimisation strategy, for Textured model.

7.2.1.3 Texture Analysis:

Using the textured model it is possible to compute the texture power $E[\tau^2]$. Reminding that $E[\tau^2] = 1$ describes the Gaussian model, we show in Figure [7.7] the behavior of such a retrieved parameter. It is possible to observe two peaks. Considering the Greenland sea ice scene, the lowest peaks corresponds to the sea water and the highest to the sea ice. Nevertheless, the most texture power is centered on 1. This means that globally the sea ice scenes considered is well defined with a Gaussian model with the only exception of the sea water zone. It is important to say that we have considered the simplest case of the texture. In fact, we have considered the same texture for the volume and the surface components. We think the volume component has a Gaussian behavior,

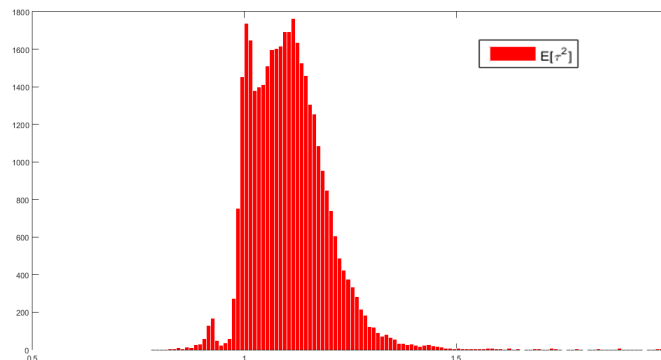


Figure 7.7: Texture power of the Sea Ice-Two component decomposition.

with the power texture near to one, but we believe that this behavior is not appropriated for the surface. In fact we expect a strong Non-Gaussianity for the sea ice surface scattering. We have not had time in order to realize this point but we think it could be a very interesting future work. Also to use the texture information in order to realize a classification algorithm could be an important application of our work.

7.2.2 Freeman and Durden Decomposition

Now we can see the results obtained with the Freeman and Durden decomposition. The following images are obtained with a multilooking process with a $[10 \times 10]$ window. This it is only a first tentative attempt to apply the higher-order statistics to the traditional decomposition theorems.

Second-order moments with traditional prior assumptions

In order to have a simple comparison we show in Figure [7.8] the retrieved components for the Freeman and Durden decomposition using the usual method of fixing α or β in according to $Re\{S_{hh}S_{vv}^*\}$, as seen in Section [4.3.1]. In this way we assume that α or β are real, indeed the proper model considers these two parameters as complex. It is important to remember that the components are Span normalised.

Second Order Moments with the optimisation algorithm

Figure [7.9] shows the retrieved parameters of the Freeman and Durden decomposition using only the second-order moments and the optimisation strategy. Overall, the parameters show a realistic behavior: high surface and low double bounce and volume for the water. In addition we have high volume for the mountains and high double-bounce for the urban area. The best improvement introduced by the optimisation strategy is the possibility to compute with precision the α and β parameters, without fixing any of them. It is important to

repeat that this is not possible with the traditional method. We think this is the major improvement introduced by the optimisation strategy.

Fourth-Order Moments Non-Textured model

Figure [7.10] shows the Freeman and Durden decomposition using the fourth-order moments for the Non-Textured model. The general behavior is similar to the previous case with the only difference about β and α . Also in this case, using the optimisation algorithm it is possible to retrieve the modulus of α and β , but the introduction of the three new high-order equations might lead of finding an algebraic solution and so to retrieve the complex values of these two parameters. We have not tested for lack of time, but we believe that to use the higher-order moments may represent a new interesting way in order to retrieve a greater number of parameters than the traditional methods.

Fourth-Order Moments Textured model

Figure [7.10] shows the case considering the texture. The results are similar to the second-order case, but with the important possibility to retrieve the texture information. The power texture seems to show a right behavior discerning sea water from the mountains and urban area.

Summary

To apply the higher-order moments method to the traditional Freeman and Durden it was only a first tentative attempt and we think this road could be furthermore explored. Comparing Figure [7.8] and Figures [7.9], [7.10], and [7.11] it is possible to notice that using the optimisation algorithm it is possible to retrieve a more defined value of α and β compared to the traditional Freeman and Durden decomposition. Another interesting point is the possibility to retrieve the texture information, that was not possible in the traditional model-based case. Obviously, using a classification clustering algorithm it is possible to obtain the texture information, but it is not achievable using the tradition model-based decompositions. The Figure [7.12] shows the RGB images for the described methods. In particular it is possible to see the main similarity of the images. This fact confirms furthermore the proper validity of the used optimisation strategy. The RGB image for the Textured model, that we remember they are power fractions, shows a more realistic behavior compared to the others, as expected. In addition, using a more complex model of the texture, as described in Section [7.2.1.3], it might lead to additional better results.

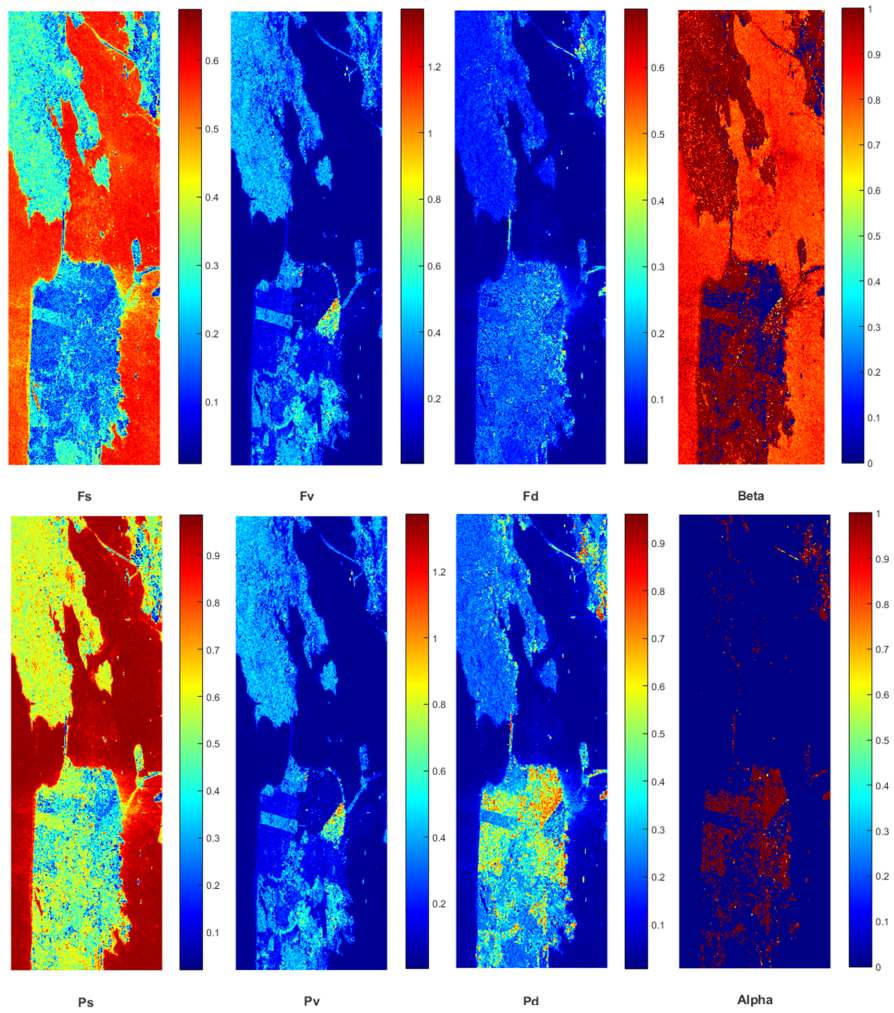


Figure 7.8: Traditional Freeman and Durden decomposition fixing β or α .

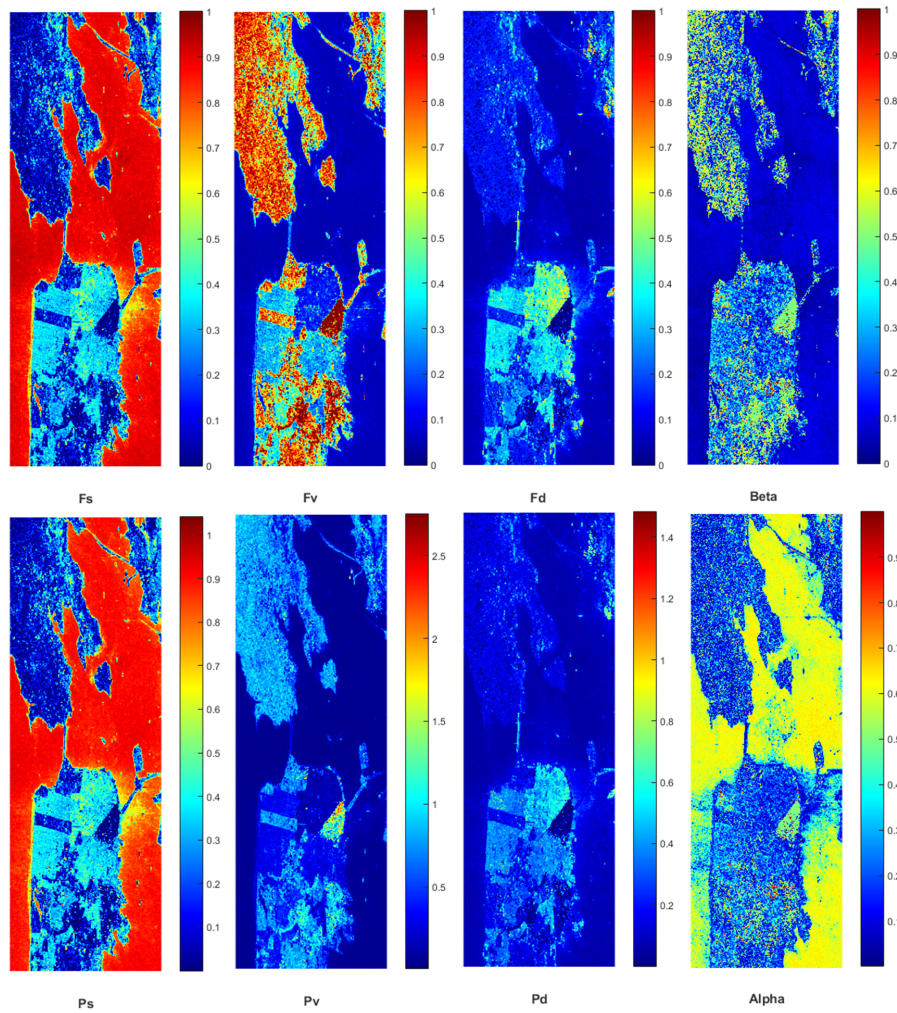


Figure 7.9: Freeman and Durden decomposition obtained with the second-order moments and the optimisation algorithm.

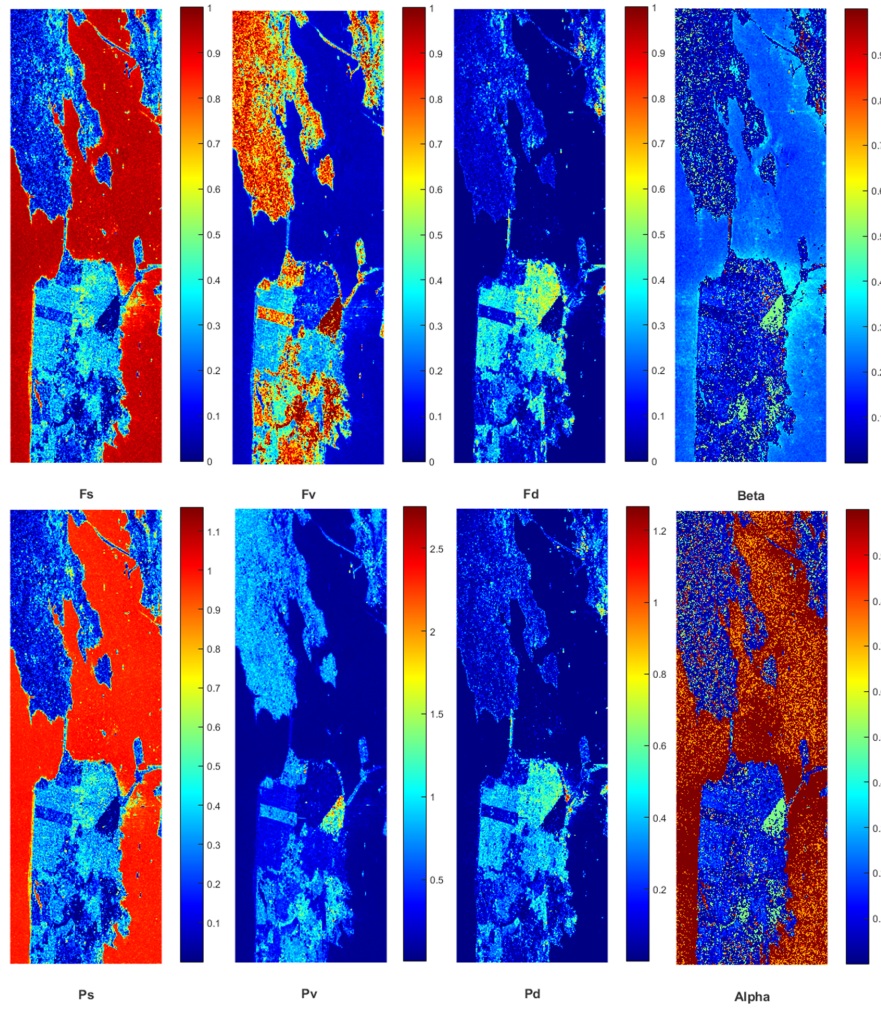


Figure 7.10: Freeman and Durden decomposition obtained with the fourth-order moments for the Non-Textured model.

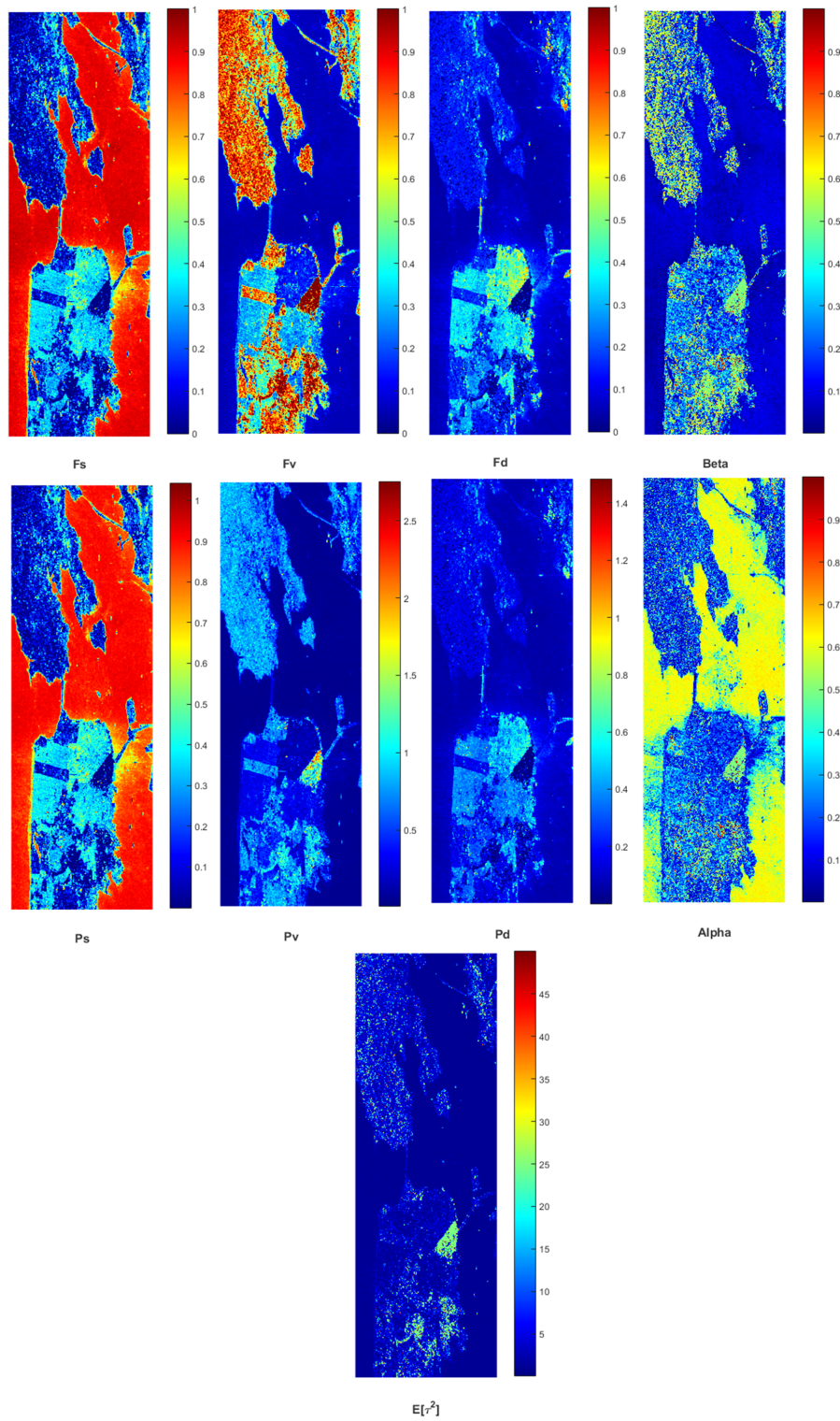


Figure 7.11: Freeman and Durden decomposition obtained with the fourth-order moments for the Textured model.

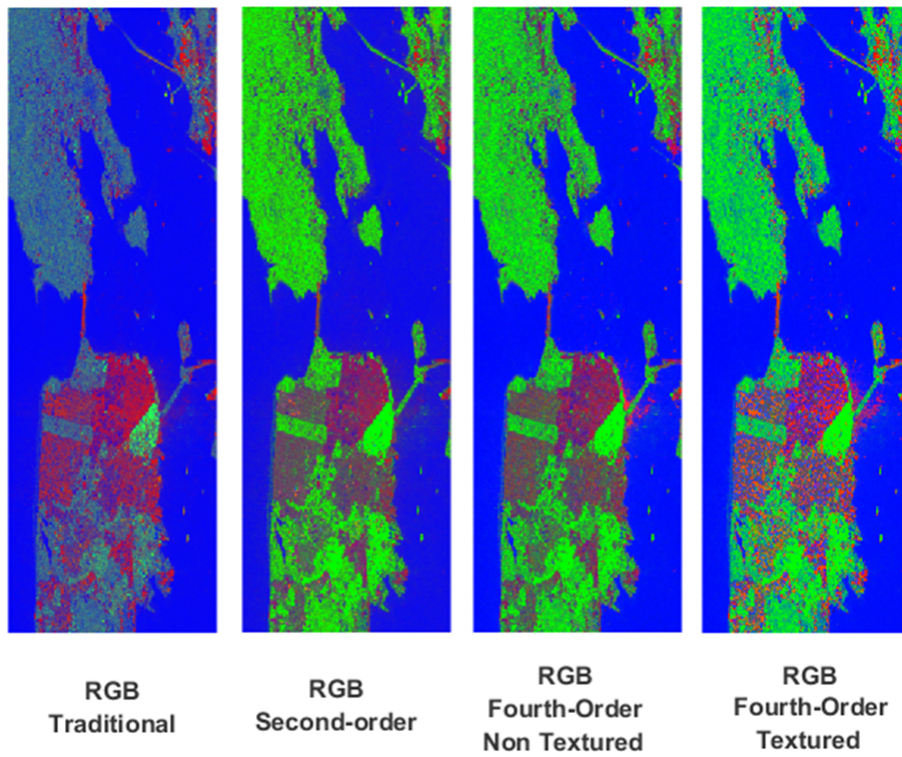


Figure 7.12: RGB images power fractions of the considered decompositions.

Chapter 8

Conclusions

8.1 Summary

Let us analyze the conclusions of our work. We start listing all we have done and then we will describe each point in detail.

- We studied and analyzed the physical and electromagnetic model of the Sea Ice, in particular the Arctic Sea Ice. Afterward, we applied such an analysis to the specific Sea Ice model-based decomposition: the Sea Ice Two-Component decomposition.
- We have confirmed a recently proposed statistical method based on the fourth-order moments to apply the traditional model-based decompositions.
- We showed preliminary results for an optimisation strategy with a preliminary algorithm that are able to solve the system of equations of the model-based decompositions.

In the part of the sea ice analysis we focused on the main characteristics that influence the scattering type of the Sea Ice. We mainly focused on the differences between Multi-Year ice and First-year ice. The Multi-year ice is characterized by strong volume scattering because the almost zero salinity allows a larger depth penetration of the incident wave and so to allow to the air-bubbles and air inclusions in the upper layer of the ice to influence the electromagnetic response. The First-year ice, characterized by a strong salinity does not allow a significant depth penetration. Theoretically, this is the reason that the First-year ice is strongly characterized by surface scattering. The main part of our work has been to evaluate the possibility of using the higher order moments than those of the second order, to the traditional model-based decomposition. The second-order moments are typically used because they have a clear physics meaning: the power. The fourth-order moments do not have a physical meaning but only a statistical meaning. This is the reason because we choose the title:

“Physical and statistical based decomposition of PolSAR images of Arctic sea ice”. Such a possibility has been evaluated using the Sea Ice Two-Component decomposition and so we were able to get the following results:

1. to have the possibility to get an analytic or algebraic solution without fixing any parameters, as shown in Table [7.2] for test patterns and in Figure [7.4] for the real images, in Subsection [7.2.1]
2. to have the possibility of including the product model and so to get information about the texture for any model-based decomposition.
3. using an optimisation algorithm it was possible to retrieve a solution when an algebraic solution cannot be found.
4. using an optimisation algorithm we obtain smooth images and so we can affirm the more speckle robustness of the optimisation strategy, than the algebraic solution, as it is possible to see comparing Table [7.2] and Table [7.4] in Subsection [7.2.1].

In order to evaluate the possible benefits introduced the fourth-order moments we built the test patterns in order to have a quick and reliable comparison method. The test pattern was built using real typical sea ice and ocean water parameters. The most important result of our work is shown by the strong improvement in the test pattern results. In particular we have found that the use of the fourth-order moments, for the Non-Textured model and for Gaussian data, allows to reduce to half the RrMSE compared to that of the second-order case. From that standpoint, we can affirm the usefulness of using the fourth-order moments to the traditional model-based decomposition in radar polarimetry. Although this is well-confirmed for the test pattern we cannot say the same for the real sea ice image we tested. The lack of in situ measurements does not allow a certain interpenetration of the Sea Ice Two-Component decomposition, but considering the main differences between First-year ice and Multi-year ice, explained in Subsection [3.3.3], we are almost sure that the diffuse high volume component over all the scene is not correct. The Sea Ice Two-Component decomposition it was not the only analyzed decomposition with the fourth-order statistics. We applied the same statistical method to the most traditional model-based decomposition: the Freeman and Durden decomposition, and using the well-known image of the San Francisco Bay, California, for which we know the ground scenario. The corresponding results in Subsection [7.2.2] show some interesting aspects: although the reconstructed images are very similar, the image obtained considering the fourth-order moments with the texture seems to show a more realistic behavior, as it is possible to see in Figure [7.12]. It is important to remember we used the simplest case of the texture, common to the all scattering mechanisms. On the other hand, the similarity of the images confirms the goodness of the proposed optimisation strategy. The last aspect, but not less important, we were able to retrieve, without making prior assumptions, three free parameters, α , β and the texture compared to the traditional Freeman and

Durden decomposition. Indeed, the traditional Freeman and Durden decomposition allows to find α or β only fixing one of them. Comparing Figure [7.8] and Figures [7.9], [7.10], [7.11] it is possible to observe a more realistic behavior of α and β . Concluding, we believe this fact is very significant: we have proposed a preliminary method applicable to any model-based decomposition in order to retrieve a larger number of parameters compared to the traditional cases.

8.2 Future challenges

Before showing the possible future challenges, it is important to remember what we think could be improved in our work. As first point will be important to improve the implementation of the Sea Ice Two-Component decomposition. The imbalance of the error equations was a clear limitation in the presented work and we are sure that fixing this point it would be possible to get stronger improvement for all the results. We propose now our ideas about the balance between the errors introduced by each equation. Considering a small sliding window on each component of the MLC data and extracting the variance and using such a variance as the normalisation factor for the optimisation algorithm we think this method might considerably improve the image reconstruction. For lack of time, we have not tested this idea. Another possible future work is about the texture. The extraction of texture information from the higher-order model-based decompositions is one of the best possibility of our work. We considered the simplest case of the texture, common to all the scattering mechanism. We believe that using two texture parameters, one for each component, would be more physically realistic and it might lead a significant improvement. In particular, we think the texture could be very different for the volume scattering and for the surface scattering. We expect a non Gaussian behavior for the surface scattering texture and a Gaussian behavior for the volume scattering texture. This confirms the possibility of a future exploration of the texture starting from our work.

Bibliography

- [1] L. Alparone, B. Aiazzi, S. Baronti, and Garzelli A. *Remote Sensing Image Fusion*. CRC Press , Print ISBN: 978-1-4665-8749-6 eBook ISBN: 978-1-4665-8750-2, 2015.
- [2] S.N. Anfinsen, A.P. Doulgeris, and T. Eltoft. Estimation of the equivalent number of looks in polarimetric synthetic aperture radar imagery. *Geoscience and Remote Sensing, IEEE Transactions on*, 47(11):3795–3809, Nov 2009.
- [3] F. Argenti, A. Lapini, T. Bianchi, and L. Alparone. A tutorial on speckle reduction in synthetic aperture radar images. *Geoscience and Remote Sensing Magazine, IEEE*, 1(3):6–35, Sept 2013.
- [4] S. Cloude. *Polarisation : Applications in remote sensing*. Oxford University Press., 2010.
- [5] S.R. Cloude and E. Pottier. A review of target decomposition theorems in radar polarimetry. *Geoscience and Remote Sensing, IEEE Transactions on*, 34(2):498–518, Mar 1996.
- [6] I. Cumming and Frank H. Wong. *Digital processing of synthetic aperture radar data : Algorithms and implementation*. MA: Artech House., 2005.
- [7] A. P. Doulgeris and T. Eltoft. Can higher-order statistics add information in model-based polarimetric decompositions? POLinSAR 2015 2015-01-26 - 2015-01-30 2015.
- [8] C. Elachi and J. Van Zyl. *Introduction to the physics and techniques of remote sensing*. Hoboken, N.J: Wiley, 2nd edition, 2006.
- [9] T. Eltoft, A. P. Doulgeris, and J. Grahn. Model-based polarimetric decomposition of arctic sea ice. pages 1–4, June 2014.
- [10] European Space Agency. ESA. *Polarimetric Decompositions*.
- [11] I. Hajnsek, T. Jagdhuber, H. Schon, and K.P. Papathanassiou. Potential of estimating soil moisture under vegetation cover by means of polsar. *Geoscience and Remote Sensing, IEEE Transactions on*, 47(2):442–454, Feb 2009.

- [12] I. Hajnsek, E. Pottier, and S.R. Cloude. Inversion of surface parameters from polarimetric sar. *Geoscience and Remote Sensing, IEEE Transactions on*, 41(4):727–744, April 2003.
- [13] M. Hallikainen and D. P. Winebrenner. The physical basis for sea ice remote sensing. pages 29–46, 2013.
- [14] Monson H. Hayes. *Statistical Digital Signal Processing and Modeling*. John Wiley & Sons, Inc., New York, NY, USA, 1st edition, 1996.
- [15] J. R. Huynen. Phenomenological theory of radar targets. 1970.
- [16] Rob J. Hyndman and Anne B. Koehler. Another look at measures of forecast accuracy. *International Journal of Forecasting*, 22(4):679 – 688, 2006.
- [17] IEEE. Ieee standard letter designations for radar-frequency bands. *IEEE Std 521-2002 (Revision of IEEE Std 521-1984)*, pages 1–3, 2003.
- [18] J. Jackson. *Classical electrodynamics*. 3rd edition, 1999.
- [19] J. Lee and Eric. Pottier. *Polarimetric radar imaging : From basics to applications*, volume Vol. 142, Optical science and engineering. Fla: CRC Press., 2009.
- [20] E. L. Lehmann and George Casella. *Theory of point estimation*. Springer Texts in Statistics. Springer-Verlag, New York, second edition, 1998.
- [21] MANICE. Manual of standard procedures for observing and reporting ice conditions. *Canadian Ice Service*, Ottawa, Ontario, Canada, 2005. ISBN: 0-660-62858-9.
- [22] M.A. N. Moen. Analysis and interpretation of c-band polarimetric sar signatures of sea ice. *The Cryosphere*, 7(6):1693–1705, 2013.
- [23] S. V. Nghiem, R. Kwok, S. H. Yueh, and M. R. Drinkwater. Polarimetric signatures of sea ice: 1. theoretical model. *Journal of Geophysical Research: Oceans*, 100(C7):13665–13679, 1995.
- [24] S. V. Nghiem, S. H. Yueh, R. Kwok, and F. K. Li. Symmetry properties in polarimetric remote sensing. *Radio Science*, 27(5):693–711, 1992.
- [25] C Oliver and S. Quegan. *Understanding synthetic aperture radar images*. (The SciTech radar and defense series). N.C: SCITECH, 2004.
- [26] R. G. Onstott. *SAR and Scatterometer Signatures of Sea Ice*, pages 73–104. American Geophysical Union, 2013.
- [27] James Overland, Kevin Wood, and Muyin Wang. Warm arctic - cold continents: climate impacts of the newly open arctic sea. *Polar Research*, 30(0), 2011.

- [28] D. K. Perovich and A. J. Gow. A quantitative description of sea ice inclusions. *Journal of Geophysical Research: Oceans*, 101(C8):18327–18343, 1996.
- [29] E. Pottier. Polsarpro v5.0 practical - 2nd advanced course on radar polarimetry. <https://earth.esa.int/>.
- [30] M. Shokr and N. Sinha. Arctic sea ice microstructure observations relevant to microwave scattering. *ARCTIC*, 47(3), 1994.
- [31] M. Skolnik. *Introduction to radar systems*. Boston, 3rd edition, 2001.
- [32] W. B. Tucker, D. K. Perovich, A. J. Gow, W. F. Weeks, and M. R. Drinkwater. *Physical Properties of Sea Ice Relevant to Remote Sensing*, pages 9–28. American Geophysical Union, 2013.
- [33] J. van Zyl. Unsupervised classification of scattering behavior using radar polarimetry data. *Geoscience and Remote Sensing, IEEE Transactions on*, 27(1):36–45, Jan 1989.
- [34] J.J. van Zyl. *Synthetic Aperture Radar Polarimetry*. JPL Space Science and Technology Series. Wiley, 2011.
- [35] J.J. van Zyl, M. Arii, and Yunjin Kim. Model-based decomposition of polarimetric sar covariance matrices constrained for nonnegative eigenvalues. *Geoscience and Remote Sensing, IEEE Transactions on*, 49(9):3452–3459, Sept 2011.
- [36] T. Vihma. Effects of arctic sea ice decline on weather and climate: A review. *Surveys in Geophysics*, 35(5):1175–1214, 2014.
- [37] S.H. Yueh, J.A. Kong, J.K. Jao, R.T. Shin, and L.M. Novak. K-distribution and polarimetric terrain radar clutter. *Journal of Electromagnetic Waves and Applications*, 3(8):747–768, 1989.

Appendix A

Freeman and Durden Decomposition

Derivation of Volume Scattering Covariance Matrix

Freeman and Durden decomposition consider the volume scattering generated from a cloud of randomly oriented cylinder-like scatterers. The scattering matrix for a small vertical dipole is given by:

$$\mathbf{S} = \begin{bmatrix} 0 & 0 \\ 0 & 1 \end{bmatrix} \quad (\text{A.1})$$

If we consider θ as the angle of the particle around the radar line of sight, we can write, through the Singular Value Decomposition, SVD, the equivalent form of the scattering matrix \mathbf{S} :

$$\begin{aligned} \mathbf{S} &= \begin{bmatrix} \cos \theta & \sin \theta \\ -\sin \theta & \cos \theta \end{bmatrix} \begin{bmatrix} 0 & 0 \\ 0 & 1 \end{bmatrix} \begin{bmatrix} \cos \theta & -\sin \theta \\ \sin \theta & \cos \theta \end{bmatrix} = \\ &= \begin{bmatrix} \sin^2 \theta & \sin \theta \cos \theta \\ \sin \theta \cos \theta & \cos^2 \theta \end{bmatrix} \end{aligned} \quad (\text{A.2})$$

Reformulating \mathbf{S} as a Pauli scattering vector we have:

$$\boldsymbol{\kappa} = \frac{1}{\sqrt{2}} \begin{bmatrix} \sin^2 \theta + \cos^2 \theta \\ \sin^2 \theta - \cos^2 \theta \\ 2 \sin \theta \cos \theta \end{bmatrix} = \frac{1}{\sqrt{2}} \begin{bmatrix} 1 \\ -\cos 2\theta \\ \sin 2\theta \end{bmatrix} \quad (\text{A.3})$$

The corresponding coherency \mathbf{T} matrix is given by:

$$\mathbf{T} = \langle \boldsymbol{\kappa} \boldsymbol{\kappa}^H \rangle =$$

$$= \frac{1}{2} \begin{bmatrix} 1 & -\cos 2\theta & \sin 2\theta \\ -\cos 2\theta & |\cos 2\theta|^2 & -\cos 2\theta \sin 2\theta \\ \sin 2\theta & -\cos 2\theta \sin 2\theta & |\sin 2\theta|^2 \end{bmatrix} \quad (\text{A.4})$$

Assuming the prolate particle randomly is randomly oriented about the radar line of sight, we can average this matrix over all possible angles θ :

$$p(\theta) = \partial\theta/2\pi \quad 0 \leq \theta \leq 2\pi \quad (\text{A.5})$$

In this way the off-diagonal terms will be zero, as expected. Resolving the following integrals:

$$\begin{aligned} T_{11} &= \frac{1}{2} \int_0^{2\pi} p(\theta) \partial\theta = \frac{1}{4\pi} \int_0^{2\pi} \partial\theta = \frac{1}{2} \\ T_{12} &= -\frac{1}{2} \int_0^{2\pi} \cos 2\theta p(\theta) \partial\theta = -\frac{1}{4\pi} \int_0^{2\pi} \cos 2\theta \partial\theta = 0 \\ T_{13} &= \frac{1}{2} \int_0^{2\pi} \sin 2\theta p(\theta) \partial\theta = \frac{1}{4\pi} \int_0^{2\pi} \sin 2\theta \partial\theta = 0 \\ T_{21} &= T_{12} \\ T_{22} &= \frac{1}{2} \int_0^{2\pi} |\cos 2\theta|^2 p(\theta) \partial\theta = \frac{1}{4\pi} \int_0^{2\pi} |\cos 2\theta|^2 \partial\theta = \frac{1}{4\pi} \left[\frac{1}{2}\theta + \frac{1}{4} \sin(2\theta) \Big|_0^{2\pi} \right] = \frac{1}{4\pi} \cdot \pi = \frac{1}{4} \\ T_{23} &= -\frac{1}{2} \int_0^{2\pi} \cos 2\theta \sin 2\theta p(\theta) \partial\theta = -\frac{1}{4\pi} \int_0^{2\pi} \cos 2\theta \sin 2\theta \partial\theta = 0 \\ T_{31} &= T_{13} \\ T_{32} &= T_{23} \\ T_{33} &= \frac{1}{2} \int_0^{2\pi} |\sin 2\theta|^2 p(\theta) \partial\theta = \frac{1}{4\pi} \int_0^{2\pi} |\sin 2\theta|^2 \partial\theta = \frac{1}{4\pi} \left[\frac{1}{2}\theta - \frac{1}{8} \sin(2\theta) \Big|_0^{2\pi} \right] = \frac{1}{4\pi} \cdot \pi = \frac{1}{4} \end{aligned} \quad (\text{A.6})$$

we finally obtain the coherency \mathbf{T} matrix form:

$$\mathbf{T} = \begin{bmatrix} 1/2 & 0 & 0 \\ 0 & 1/4 & 0 \\ 0 & 0 & 1/4 \end{bmatrix} \quad (\text{A.7})$$

and using Equation [2.44] we can write the volume scattering covariance \mathbf{C} matrix as:

$$\mathbf{C} = \frac{1}{2} \begin{bmatrix} 3/4 & 0 & 1/4 \\ 0 & 1/2 & 0 \\ 1/4 & 0 & 3/4 \end{bmatrix} \quad (\text{A.8})$$

It is important to notice that, having considered θ uniformly distributed, the previous form of \mathbf{C} would have been obtained also in case of horizontal dipoles:

$$\mathbf{S} = \begin{bmatrix} 1 & 0 \\ 0 & 0 \end{bmatrix} \quad (\text{A.9})$$

Appendix B

Sea Ice Two-Component Decomposition

Derivation of Algebraic Solution

We show the procedure in order to derive the algebraic solution for the Sea Ice Two-Component decomposition. It is important to notice that having more equations than unknowns it is not the unique possible procedure. We start subtracting \tilde{T}_{33} from \tilde{T}_{22} :

$$\begin{aligned}
 \tilde{T}_{22} - \tilde{T}_{33} &= \\
 &= \frac{1}{2} f_s SPAN \frac{|\beta|^2 (1 + \text{sinc}(4\delta))}{(1 + |\beta|^2)} + f_v SPAN \frac{(1 - \rho)}{3 - \rho} - \\
 &\quad - \frac{1}{2} f_s SPAN \frac{|\beta|^2 (1 + \text{sinc}(4\delta))}{(1 + |\beta|^2)} - f_v SPAN \frac{(1 - \rho)}{3 - \rho} = \\
 &= \frac{1}{2} f_s SPAN \frac{|\beta|^2}{(1 + |\beta|^2)} + \frac{1}{2} f_s SPAN \frac{|\beta|^2 \text{sinc}(4\delta)}{(1 + |\beta|^2)} + f_v SPAN \frac{(1 - \rho)}{3 - \rho} - \\
 &\quad - \frac{1}{2} f_s SPAN \frac{|\beta|^2}{(1 + |\beta|^2)} + \frac{1}{2} f_s SPAN \frac{|\beta|^2 \text{sinc}(4\delta)}{(1 + |\beta|^2)} - f_v SPAN \frac{(1 - \rho)}{3 - \rho} = \\
 &= f_s \cdot SPAN \frac{|\beta|^2 \text{sinc}(4\delta)}{(1 + |\beta|^2)} \tag{B.1}
 \end{aligned}$$

Let us do the same with $\langle k_2 \rangle^4$ and $\langle k_3 \rangle^4$:

$$\langle k_2 \rangle^4 - \langle k_3 \rangle^4 =$$

$$\begin{aligned}
 &= 2SPAN^2 \left(f_s \left[\frac{|\beta|^2 (1 + \text{sinc}(4\delta))}{2(1 + |\beta|^2)} \right]^2 + f_v \left[\frac{(1 - \rho)}{3 - \rho} \right]^2 \right) - \\
 &- 2SPAN^2 \left(f_s \left[\frac{|\beta|^2 (1 - \text{sinc}(4\delta))}{2(1 + |\beta|^2)} \right]^2 + f_v \left[\frac{(1 - \rho)}{3 - \rho} \right]^2 \right) = \\
 &= 2SPAN^2 f_s \left(\frac{|\beta|^4}{4(1 + |\beta|^2)^2} + \frac{|\beta|^4 \text{sinc}^2(4\delta)}{4(1 + |\beta|^2)^2} + \frac{|\beta|^4 \text{sinc}(4\delta)}{2(1 + |\beta|^2)^2} \right) \\
 &- f_s \left(\frac{|\beta|^4}{4(1 + |\beta|^2)^2} + \frac{|\beta|^4 \text{sinc}^2(4\delta)}{4(1 + |\beta|^2)^2} - \frac{|\beta|^4 \text{sinc}(4\delta)}{2(1 + |\beta|^2)^2} \right) + \\
 &+ 2SPAN^2 f_v \left[\frac{(1 - \rho)}{3 - \rho} \right]^2 - 2SPAN^2 f_v \left[\frac{(1 - \rho)}{3 - \rho} \right]^2 = \\
 &= 2SPAN^2 f_s \frac{|\beta|^4 \text{sinc}(4\delta)}{(1 + |\beta|^2)^2}
 \end{aligned}$$

Considering the ratio of $\tilde{T}_{22} - \tilde{T}_{33}$ and $\langle k_2 \rangle^4 - \langle k_3 \rangle^4$:

$$\begin{aligned}
 &\frac{\tilde{T}_{22} - \tilde{T}_{33}}{\langle k_2 \rangle^4 - \langle k_3 \rangle^4} = \\
 &= f_s \cdot SPAN \frac{|\beta|^2 \text{sinc}(4\delta)}{(1 + |\beta|^2)} \cdot \frac{(1 + |\beta|^2)^2}{2SPAN^2 f_s \text{sinc}(4\delta) |\beta|^4} = \\
 &= f_s \cdot \frac{(1 + |\beta|^2)}{2SPAN |\beta|^2}
 \end{aligned}$$

it is possible to obtain $|\beta|^2$:

$$\begin{aligned}
 &\left[\frac{\tilde{T}_{22} - \tilde{T}_{33}}{k_2 - k_3} \right] 2SPAN |\beta|^2 = (1 + |\beta|^2) \\
 &|\beta|^2 = \frac{k_2 - k_3}{[\tilde{T}_{22} - \tilde{T}_{33}] \cdot 2 \cdot SPAN - k_2 + k_3} \tag{B.2}
 \end{aligned}$$

Now we find f_s from the product of \tilde{T}_{12} and \tilde{T}_{12}^* :

$$\tilde{T}_{12} \tilde{T}_{12}^* = f_s \frac{\beta^* \text{sinc}(2\delta)}{(1 + |\beta|^2)} \cdot f_s \frac{\beta \text{sinc}(2\delta)}{(1 + |\beta|^2)} =$$

$$= f_s^2 \frac{|\beta|^2 \operatorname{sinc}^2(2\delta)}{(1 + |\beta|^2)^2}$$

and f_s is given by:

$$f_s = \frac{|\tilde{T}_{12}| (1 + |\beta|^2)}{|\beta| \operatorname{sinc}(2\delta) \cdot \operatorname{SPAN}} \quad (\text{B.3})$$

Using the Span relationship we can find f_v :

$$f_v = 1 - f_s \quad (\text{B.4})$$

Now we can find δ substituting f_s in $\tilde{T}_{22} - \tilde{T}_{33}$:

$$\begin{aligned} \tilde{T}_{22} - \tilde{T}_{33} &= \\ &= f_s \cdot \operatorname{SPAN} \frac{|\beta|^2 \operatorname{sinc}(4\delta)}{(1 + |\beta|^2)} = \\ &= \operatorname{SPAN} \frac{|\tilde{T}_{12}| (1 + |\beta|^2)}{|\beta| \operatorname{sinc}(2\delta) \cdot \operatorname{SPAN}} \cdot \frac{|\beta|^2 \operatorname{sinc}(4\delta)}{(1 + |\beta|^2)} = \\ &= \frac{|\tilde{T}_{12}| \cdot |\beta| \operatorname{sinc}(4\delta)}{\operatorname{sinc}(2\delta)} \\ &= |\tilde{T}_{12}| \cdot |\beta| \frac{\operatorname{sinc}(4\delta)}{\operatorname{sinc}(2\delta)} = \frac{|\tilde{T}_{12}| \cdot |\beta| \sin(4\delta)}{2\delta} \frac{\delta}{\sin(2\delta)} = \\ &= |\tilde{T}_{12}| \cdot |\beta| \frac{\sin(4\delta)}{2 \sin(2\delta)} = \end{aligned}$$

and using the duplication formula:

$$\sin 2\alpha = 2 \sin \alpha \cos \alpha \quad (\text{B.5})$$

we obtain:

$$= |\tilde{T}_{12}| \cdot |\beta| \frac{\sin(4\delta)}{2 \sin(2\delta)}$$

In this way, it is possible to arrive to the final expression of δ :

$$\delta = \frac{1}{2\pi} \arccos \left[\frac{\tilde{T}_{22} - \tilde{T}_{33}}{|\tilde{T}_{12}| \cdot |\beta|} \right] \quad (\text{B.6})$$

From T_{11} it is possible to calculate ρ :

$$\tilde{T}_{11} =$$

$$\begin{aligned}
 &= f_s \frac{SPAN}{(1 + |\beta|^2)} + f_v SPAN \frac{(1 + \rho)}{3 - \rho} = \\
 &= \frac{f_s SPAN (3 - \rho) + f_v SPAN (1 + \rho) (1 + |\beta|^2)}{(1 + |\beta|^2) (3 - \rho)}
 \end{aligned}$$

Resolving we have:

$$\begin{aligned}
 \tilde{T}_{11} (1 + |\beta|^2) (3 - \rho) &= f_s SPAN (3 - \rho) + f_v SPAN (1 + \rho) (1 + |\beta|^2) = \\
 3\tilde{T}_{11} + 3\tilde{T}_{11} |\beta|^2 - \tilde{T}_{11} \rho - \tilde{T}_{11} \rho |\beta|^2 &= \\
 = 3f_s SPAN + \rho [f_v SPAN (1 + |\beta|^2) - f_s SPAN] + f_v SPAN + f_v SPAN |\beta|^2 &= \\
 \rho = \frac{(1 + |\beta|^2)(f_v \cdot SPAN - 3\tilde{T}_{11}) + 3f_v \cdot SPAN}{-[(1 + |\beta|^2)(\tilde{T}_{11} + f_v \cdot SPAN) + SPAN \cdot f_s]} &=
 \end{aligned}$$

Finally we can write the expression of the algebraic solution for the Sea Ice Two-Component decomposition:

$$|\beta|^2 = \frac{k_2 - k_3}{[\tilde{T}_{22} - \tilde{T}_{33}] \cdot 2 \cdot SPAN - k_2 + k_3} \quad (\text{B.7})$$

$$\delta = \frac{1}{2\pi} \arccos \left[\frac{\tilde{T}_{22} - \tilde{T}_{33}}{|\tilde{T}_{12}| \cdot |\beta|} \right] \quad (\text{B.8})$$

$$f_s = \frac{|\tilde{T}_{12}| (1 + |\beta|^2)}{|\beta| \text{sinc}(2\delta) \cdot SPAN} \quad (\text{B.9})$$

$$f_v = 1 - f_s \quad (\text{B.10})$$

$$\rho = \frac{(1 + |\beta|^2)(f_v \cdot SPAN - 3\tilde{T}_{11}) + 3f_v \cdot SPAN}{-[(1 + |\beta|^2)(\tilde{T}_{11} + f_v \cdot SPAN) + SPAN \cdot f_s]} \quad (\text{B.11})$$

□

